UNIVERSITÉ DU LUXEMBOURG

PhD-FSTC-2019-43
The Faculty of Science, Technology and Communication

DISSERTATION

Defense held on 03/06/2019 in Luxembourg

to obtain the degree of

DOCTEUR DE L'UNIVERSITÉ DU LUXEMBOURG

EN SCIENCES DE L'INGÉNIEUR

by

Kerstin Julia CRAMER
Born on 26 June 1990 in Hamburg, (Germany)

NUMERICAL MODELING OF AIR-GAP MEMBRANE DISTILLATION

Dissertation defense committee

Dr Stephan Leyer, dissertation supervisor
Professor, Université du Luxembourg, Luxembourg

Dr Horst-Michael Prasser
Professor, Eidgenössische Technische Hochschule Zürich, Schweiz

Dr Joachim Hansen, Chairman
Professor, Université du Luxembourg, Luxembourg

Dr Robert Mnich
Professor, Technische Hochschule Deggendorf, Deutschland

Dr Bojan Niceno, Vice Chairman
Group Leader, Computational Fluid Dynamics Group, Paul Scherrer Institut, Schweiz

Für meine Eltern, Edith und Heinz, und meine Schwester Catarina.

Abstract

Fresh water supply is a problem in large parts of the world and present on every continent. Many countries facing physical water scarcity, however, have access to the sea and lie in arid zones of the earth where solar energy is plentiful available. Membrane distillation (MD) describes an emerging desalination technology which has advantages when driven by solar energy or waste heat. In MD, seawater is thermally desalinated by generating a temperature gradient between hot salt water and produced fresh water which are separated by a membrane. In air-gap membrane distillation (AGMD) an insulating air-gap is introduced between membrane and distillate in order to minimize conductive losses. Despite its advantages, the permeate stream needs to be increased for large-scale application. To improve performance and energy efficiency, a detailed understanding of the highly coupled heat and mass transfer is crucial. However, for AGMD not many models exist and the existing models simplify the heat and mass transfer processes. The goal of this thesis is therefore to increase the understanding of the AGMD process and the predictive power of numerical models. A three-dimensional (3D) macro-scale model is developed with emphasis on the heat and mass transfer. It integrates aspects from multiphase flow modeling namely energy conservation over phase-change interfaces and the thermodynamic concept of moist air in the air-gap. Thereby, it computes the condensation mass flow independently from the evaporation mass flow, allowing to study the influence of convection on the heat and mass transfer in the air-gap. The model is accelerated for computation on graphical processing units (GPU). Employing the macro-scale model, a comparative analysis of the effects of module orientation on module performance and efficiency is performed. Vortexes in the air-gap are observed when using a module configuration where the hot feed flows below air-gap and membrane and the temperature gradient is opposing gravity. These vortexes lead to a significantly increased energy utilization also at low feed velocities. As the main advantage of AGMD is the reduction of heat losses, this configuration could bring further improvement. Furthermore, membrane transport properties are determined from high-resolution 3D membrane imaging combined with Lattice-Boltzmann simulation. Thereby, the 3D structure of membrane samples is obtained and porosity, tortuosity and permeability values are computed for the investigated membranes. Following the findings in the papers, further studies are suggested employing the modeling approaches developed in this thesis.

Preface

The work for the doctoral thesis began in September 2015 and was carried out at the Research Unit of Engineering Sciences, Faculty of Science, Technology and Communication of the University of Luxembourg. The main supervision was done by Prof. Stephan Leyer[(i)]. The Comité d'Encadrement de Thèse (Dissertation Supervisory Committee) consisted furthermore of Prof. Horst-Michael Prasser[(ii)], Prof. Robert Mnich[(iii)] and Dr. Bojan Niceno[(iii)]. The jury is formed by the members of the Comité d'Encadrement de Thèse with Prof. Joachim Hansen[(i)] as the chairman.

This thesis is organized in two main parts: Firstly an overview and summary of the work is presented, followed by a second part consisting of the appended papers and reports.

Paper A

K. Cramer, B. Niceno, H.-M. Prasser and S. Leyer, "A Three-Dimensional Model for the Heat and Mass Transfer in Air-gap Membrane Distillation", submitted to *Journal of Membrane Science*, March 2019.

Paper B

K. Cramer, N. I. Prasianakis, B. Niceno, J. Ihli, M. Holler and S. Leyer, "Three-dimensional membrane imaging with X-ray ptychography: determination of membrane transport properties for membrane distillation", submitted to *Journal of Membrane Science*, January 2019.

Paper C

K. Cramer, P. Lamesch, M.-A. Dalle, B. Niceno and S. Leyer, "Module Orientation for Performance and Energy Efficiency in Air-gap Membrane Distillation", submitted to *Desalination*, February 2019.

[(i)] Faculty of Science, Technology and Communication, University of Luxembourg, Luxembourg
[(ii)] Department of Mechanical and Process Engineering, Eidgenössische Technische Hochschule Zürich, Switzerland
[(iii)] Faculty of Mechanical Engineering and Mechatronics, Technische Hochschule Deggendorf, Germany
[(iii)] Laboratory for Scientific Computing and Modelling, Paul-Scherrer Institute, Switzerland

Paper D

K. Cramer and L. Manzari, "Speed-up Using GPU Accelerators: How to Port a Numerical Solver for CFD with PyCUDA", unpublished.

Division of work in the papers

Paper A

Cramer and Prasser formulated the theory for the heat and mass transfer modeling. Niceno developed the CFD tool in which the heat and mass transfer was implemented by Cramer. The validation study was performed by Cramer. The results were analyzed by Cramer and discussed together with Leyer. The paper was written and compiled by Cramer and it was reviewed by all the co-authors.

Paper B

Prasianakis, Niceno and Cramer proposed the idea and study conception. Membrane sample preparation was organized by Cramer. Ihli and Holler acquired the tomograms from the X-Ray ptychography. The numerical implementation was provided by Prasianakis and the simulations were performed and processed by Cramer. The results were analyzed by Cramer and discussed together with Prasianakis and Leyer. The paper was written and compiled by Cramer and it was reviewed by all the co-authors.

Paper C

The conception study was done by Lamesch, Cramer and Dalle. The simulations were performed by Cramer. The modification of the numerical model was proposed by Cramer, reviewed by Niceno and implemented by Cramer. The results were analyzed by Lamesch and Cramer and discussed together with Dalle and Leyer. The paper was written and compiled by Cramer and it was reviewed by all the co-authors.

Paper D

Cramer provided the numerical CFD code and identified the code sections for acceleration. Manzari developed the benchmarking cases. The final implementation and testing was performed together by Cramer and Manzari. The report was written and compiled by Cramer and Manzari.

Papers not included in this thesis

K. Cramer, B. Niceno, H.-M. Prasser and S. Leyer, "Numerical modelling of the heat and mass transfer in a flat-sheet air-gap membrane distillation module", presented at *3rd International Conference on Desalination using Membrane Technology*, Gran Canaria, April 2017

K. Cramer, B. Niceno, H.-M. Prasser and S. Leyer, "HEAT AND MASS TRANSFER IN FLAT-SHEET, AIR-GAP MEMBRANE DISTILLATION: A THREE-DIMENSIONAL MODEL" in *The International Desalination Association World Congress*, São Paulo, October 2017

Acknowledgment

I would like to thank my supervisor, Stephan Leyer, for giving me the means and support that allowed me to pursue this thesis work. I was extremely lucky to have a supervisor who cared about my work while giving me the freedom to put my own ideas into practice. The mutual honesty and openness throughout all the years have been greatly appreciated. I would also like to thank the members of my dissertation supervisory committee, namely Horst-Michael Prasser, Robert Mnich and Bojan Niceno for the fruitful discussions and ideas during the yearly meetings. Furthermore, I would like to thank Joachim Hansen for agreeing to be the chairman of my defense jury.

Bojan, I want to especially thank you for always taking the time to reply to all questions promptly and advising me both on how to write good code but also about priorities in life. Every time I got stuck with the CFD code, I visited PSI and you fixed it within minutes. Your dedication and involvement were essential for the results of this thesis.

I would like to thank Nikolaos Prasianakis for opening the doors to Lattice-Boltzmann simulations for me and for the constructive collaboration. Furthermore, I would like to thank Joakim Reuteler at ScopeM, ETH Zürich for his engagement preparing the membrane samples for the imaging until late in the night. For the advice and the flawless performance of the imaging experiments at the Swiss Light Source, PSI I would like to thank my local contact Johannes Ihli as well as Mirco Holler and Ana Diaz.

My officemate Michel deserves thanks not only for technical discussions but also for an invaluable introduction to Luxembourgish culture. To my colleagues Veronika and Marie-Alix: I will greatly miss our biking, climbing, yoga and sporting activities which always freed my mind, made me smile, energetic and open for new ideas. I hope that our friendship will remain well beyond our time as colleagues.
Furthermore, I want to acknowledge Elias Zea whose thesis served as a template and gave this thesis its structure.

Luca, I am incredibly happy that I went to the PDC summer school at KTH in August 2017 and met you. In the last two years, you always listened to me, encouraged me and made me smile. Thank you so much for always being by my side.

I finally want to thank my parents Edith and Heinz and my sister Catarina for their endless support and patience during all the ups and downs. I am very grateful that you always lent me an open ear when times were hard. Thank you, Heinz, for teaching me to bite through and to not give up so that this thesis was completed.

Luxembourg, June 2019
Kerstin Cramer

Nomenclature

Roman letters

$\dot{m}$	Mass flux
$\dot{q}_L$	Latent heat flux
$\dot{q}_S$	Sensible heat flux
$\dot{q}_x$	Heat flux from membrane material to air
a	Air-gap thickness
d	Height
d_w	Collision diameter for vapor
$D_{v,a}$	Diffusion coefficient of vapor in air
h	Heat transfer coefficient
h_d	Specific latent heat of evaporation
k_B	Boltzmann constant
Kn	Knudsen number
M	Molar mass
P	Pressure
p	Partial vapor pressure
$p_{a,m}$	Partial pressure of air in the membrane
R	Gas constant
r	Pore radius
T	Temperature

Greek letters

δ	Membrane thickness
ϵ	Porosity
λ	Thermal conductivity
λ_m	Mean free path of vapor
μ	Viscosity
ρ	Density
τ	Tortuosity

Subscripts

air	Air/ air-gap
$cold$	Cold side of membrane
D	Diffusion
$evap$	Evaporation
hot	Hot feed water channel
int	Interface
K	Knudsen
M	Molecular
mem	Membrane
$PVDF$	Membrane material
sat	Saturation
T	Transition
top	Top
V	Viscous flow

Contents

Part I

OVERVIEW AND SUMMARY OF THE WORK

Chapter 1

Introduction

Fresh water supply is a problem in large parts of the world and present on every continent. Around 1.2 billion people, or almost one-fifth of the world's population, live in areas of physical scarcity, and 500 million people are approaching this situation [1]. Water use has been growing at more than twice the rate of population increase in the last century, and, although there is no global water scarcity as such, an increasing number of regions are chronically short of water [1]. Water scarcity is among the main problems for many societies already and is expected to become more severe.

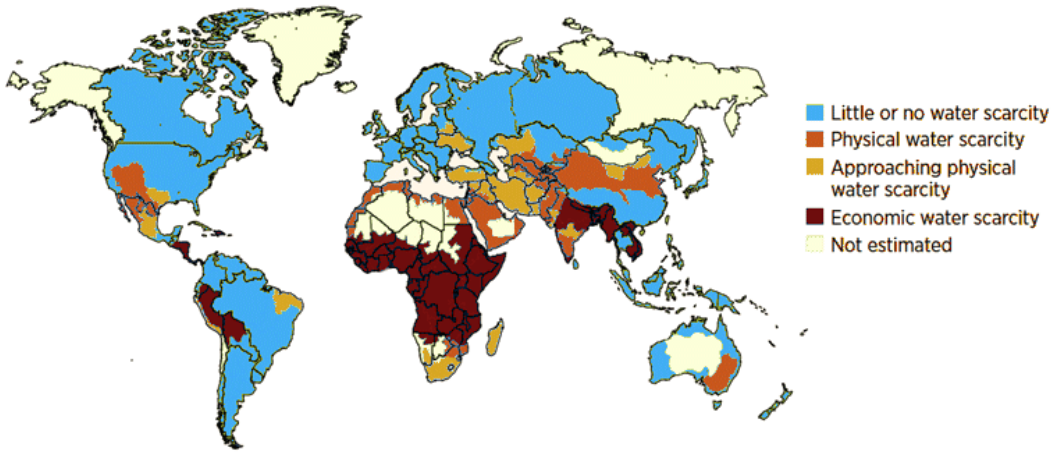

Figure 1.1: *Global physical and economic water scarcity [2]*

A look on the water scarcity world map in Fig. 1.1 reveals that many affected countries have access to the sea. Thus, seawater desalination becomes a viable option for these countries.

The most applied seawater desalination technologies in large, commercial desalination plants are thermal distillation and reverse osmosis (RO) [3]. However, the thermal distillation plants require large amounts of thermal energy and are therefore often constructed in co-generation with power plants as both need low pressure heating steam [4]. RO, on the other hand, uses electrical energy to pump seawater through a salt retaining membrane overcoming the osmotic pressure. As both technologies are energy-intensive,

they are only feasible for areas with access to appropriate infrastructure and countries which can afford the fuel for the desalination plants.

Many countries facing physical water scarcity lie in arid zones of the earth (Fig. 1.1) where solar energy is plentiful available. For rural areas, smaller desalination systems using solar energy are therefore considered promising [5].

Membrane distillation (MD) describes an emerging technology which has advantages when driven by solar energy or waste heat as temperatures below the boiling point are sufficient [6]. In MD, contaminated water or seawater is concentrated and potable water is separated via a membrane. MD modules have the advantage of small investment and operating costs and a high quality of produced water. The retention rate for substances insoluble in water vapor is close to unity [7]. Additionally, the modules are easy to install and require low maintenance [8]. There are lab-scale facilities and pilot plants designed for the desalination of seawater, treatment of waste water, concentration of juices or liquid nuclear waste [9]. However, the overall efficiency and output production rate are insufficient for large-scale facilities [10].

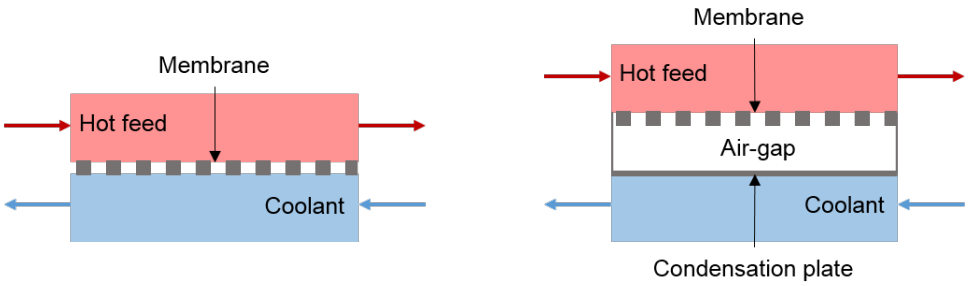

(a) *Direct contact membrane distillation* **(b)** *Air-gap membrane distillation*

Figure 1.2: *Membrane distillation configurations*

MD thermally desalinates seawater by generating a temperature gradient between hot salt water and colder fresh water which are separated by a membrane (Fig. 1.2). The feed is warmed up externally in a solar collector and flows over a membrane which is hydrophobic but permeable for vapor. The membrane is cooled from the other side, generating a gradient in temperature. The temperature gradient leads to a gradient in partial vapor pressure across the membrane and therefore diffusion of water vapor through the air in the membrane. It drives the evaporation of water at the liquid vapor interface on the membrane top at temperatures below the boiling point. Salt is not soluble in water vapor and is therefore retained in the water.

In case of direct contact membrane distillation (DCMD) the vapor is condensed directly into a fresh water stream (Fig. 1.2a). In this configuration a large portion of the supplied heat is lost in conduction through the membrane without the evaporation of vapor [11]. In air-gap membrane distillation (AGMD) an insulating air layer is introduced which is separately cooled and the vapor condenses on the condensation plate forming a liquid film layer (Fig. 1.2b). The air-gap displays an additional mass transfer resistance

for diffusion, but limits the convective heat flux through the membrane. Another configuration to reduce the conductive losses is sweeping gas membrane distillation where a cold, inert sweeping gas is transporting the vapor away after passing the membrane. The condensation of the water vapor takes place in an external condenser complicating the system design and increasing its cost [12]. In vacuum membrane distillation the pressure on the permeate side is reduced below the vapor saturation pressure using a vacuum pump. This configuration reduces the conductive losses across the membrane at the same time as it reduces the mass transfer resistance for the diffusion of the vapor [13]. However, the external condenser adds again complexity to the otherwise low-tech MD process.

AGMD is considered the most versatile and promising configuration [14]. The majority of the tested pilot systems is employing AGMD even though the operation needs to become more economical and energy efficient for successful commercial application [15].

The membranes used in MD consist of polytetrafluoroethylene (PTFE), polypropylene (PP) or polyvinylidene fluoride (PVDF) [16]. In case of PTFE, the membrane material is attached onto a coarser PP grid.

1.1. Problem statement

In order to increase the economical performance and the energy efficiency of AGMD modules, a detailed understanding of the heat and mass transport processes is crucial. The heat and mass transfer occurs simultaneously and is highly coupled [14]. Also the operational parameter like feed inlet temperature and inlet velocity influence the heat and mass transfer [17]. For a successful modeling of an AGMD module, all these effects and phenomena need to be taken into account and considered simultaneously.

In the state-of-the-art theoretical models for DCMD, the mass transfer through the membrane is calculated with one-dimensional (1D) correlations. It is based on the Dusty-Gas-Model which combines 1D diffusion and convection through porous media [18]. The Dusty-Gas-Model in its general form contains three structural parameter which should be measured for each porous medium individually. However, state-of-the-art MD models in MD employ the approximation for uniform cylinders [11]. Porosity and tortuosity (a measure for the length of the pathways through the membrane) are used to adapt the models to the actual membrane. Whereas porosity is measured, tortuosity is not explicitly known and either roughly estimated or used as a fitting parameter between experimental data and numerical model [16, 19].

For AGMD, the 1D correlation is extended to cover the vapor transport through the membrane and the air-gap [16]. The vapor flux is then directly calculated using the vapor pressure gradient between the vapor-liquid equilibrium at the hot side of the membrane and the liquid condensate layer in the air-gap channel. This procedure neglects any multi-dimensional influences in the air-gap on the mass transfer. Especially for AGMD, not many computational fluid dynamic (CFD) models exists as the diffusion process of vapor through the air-gap and the condensation process need to be included [20]. The existing models solve the velocity and temperature distribution in 2D but the vapor

mass flux still with 1D correlations combining membrane and air-gap modeling [21]. Any three-dimensional (3D) effects due to buoyancy or spacers are thereby not reflected.

1.2. General and specific goals

This thesis aims at broadening the understanding of the AGMD process in order to increase the predictive power of numerical models and eventually make AGMD a more economically feasible and energy efficient process. Specific goals are formulated on two different magnitude scales.

- On a macro-scale, an approach is to be developed to model the AGMD module in 3D including appropriate modeling of the heat and mass transfer through the air-gap. An optimization of the AGMD module should be possible using this model.
- On a micro-scale, the modeling of the vapor transport through the membrane is to be analyzed in order to reduce the necessity for fitting parameters.

1.3. Approach

According to the formulation of the goals, also the approach is structured in two magnitude scales: (i) macro-scale modeling, investigated in Paper A, C and D, and (ii) micro-scale modeling, investigated in Paper B.

Macro-scale modeling

Starting from an incompressible CFD solver, a three-dimensional (3D) model for an AGMD module is developed with 1D correlations for the heat and mass transfer through the membrane and the heat transfer through the condenser plate. From multiphase flow modeling, heat and mass transfer equations are implemented for the phase change at evaporation and condensation interfaces. The macro-scale model is validated against experimental data (Paper A). Employing the models capability of accounting for gravitational effects, a module orientations study is performed. The effects on permeate output and energy efficiency due to buoyancy are studied for seawater and tap water as feed solutions (Paper C). An option for acceleration using graphical processing units (GPU) is added to the model for large computations (Paper D).

Micro-scale modeling

3D structures of three, state-of-the-art membranes for MD are acquired by X-ray ptychography. Velocity fields are obtained by computing the viscous flow through the membrane structures via Lattice-Boltzmann (LB) simulation. From the velocity fields, membrane transport properties are computed which can be used to determine the vapor mass transport through the membrane in macro-scale models (Paper B).

1.4. Structure of the book

This thesis is divided into two parts: (i) overview and summary of the work and (ii) appended papers. The overview and summary of the work is structured as follows:

Chapter 1 introduces and states the problem investigated in the thesis, as well as the goals and approaches to achieve them,

Chapter 2 presents the state-of-the-art approach to model the heat and mass transfer through the membrane in DCMD and AGMD,

Chapter 3 compares two models for the heat and mass transfer across the evaporation interface and the membrane as a prerequisite for the 3D model in Paper A,

Chapter 4 presents a summary of the appended papers,

Chapter 5 provides directions for future research by proposing numerical studies employing the modeling options developed in this thesis,

Chapter 6 concludes and summarizes the thesis work.

Chapter 2

State-of-the-Art Membrane Modeling

2.1. Mass Transfer: The Dusty Gas Model

MANY modeling approaches exist but the most physical and applied model is the Dusty Gas Model (DGM) [11, 16]. The DGM describes the mass transfer through porous media [18] and displays the state-of-the-art model for MD [19]. Mass transfer through the membrane occurs by diffusive and viscous transport of vapor (Fig. 2.1). The DGM can include surface diffusion, however, this diffusion process is generally considered negligible [11]. It is originally developed for isothermal systems, but it is applied in MD with the assumption of an average temperature in the membrane [16]. This chapter is intended as an introduction to the DGM and in the provided equations the approximation of uniform cylinders is applied for the structural parameter [11].

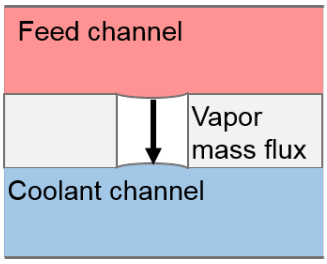

Figure 2.1: *Illustration of membrane mass transfer in DCMD modeling*

Mass Transfer Mechanisms

The diffusion of the water vapor is driven by the partial pressure gradient across the membrane. The vapor molecules interact thereby with the membrane wall (Knudsen diffusion) and with the air molecules trapped in the pores (molecular diffusion).

The vapor flux through the membrane due to Knudsen diffusion $\dot{m}_{D,K}$ can be calculated according to Eq. 2.1 [16, 22]

$$\dot{m}_{D,K} = -\frac{2}{3}\frac{\epsilon r}{\tau}\sqrt{\frac{8\,M}{\pi R T}}\nabla p \tag{2.1}$$

where ϵ is the membrane porosity, τ the membrane tortuosity, r the membrane pore radius, M the molecular weight, T the temperature and ∇p the partial vapor pressure gradient across the membrane.

The molecular diffusion is also referred to as Stefan diffusion or ordinary diffusion and derived for the diffusion of a multicomponent mixture of gases. In the membrane, vapor and air are present. However, as the solubility of air in water is relatively low (around 10ppm), the resulting air flux is rather low compared to the vapor flux and therefore commonly neglected [16]. The vapor flux due to molecular diffusion $\dot{m}_{D,M}$ can then be obtained by

$$\dot{m}_{D,M} = -\frac{\epsilon D_{v,a} M P}{\tau R T p_{a,m}} \nabla p \tag{2.2}$$

with $D_{v,a}$ as the diffusion coefficient of vapor in air, P the total pressure and $p_{a,m}$ the partial air pressure in the membrane.

The viscous flow or Poiseuille flow displays the convective flow through a capillary due to the total pressure gradient across the membrane [18]. The force on the fluid due to the pressure gradient needs to be compensated by the viscous drag force in order to not accelerate the fluid. The inertia of the membrane is thereby neglected. The DGM states that the convective flow does not separate a mixture into its components.

The vapor flux due to viscous flow $\dot{m}_V$ can be calculated by Eq. 2.3, a Poiseuille-like equation modified for compressible fluids [16, 18]

$$\dot{m}_V = -\frac{\epsilon r^2 M p}{8 \tau R T \mu} \nabla P \tag{2.3}$$

where μ is the viscosity.

Coupling of the Mass Transfer Mechanisms

The vapor pressure difference leads to the diffusive mass flow whereas the total pressure drop results in viscous flow. There are no convective terms in the diffusion equation and no diffusive terms in the convection equation. The viscous and diffusive mass fluxes are therefore additive and the total membrane vapor flux $\dot{m}$ can be calculated as [18]

$$\dot{m} = \dot{m}_D + \dot{m}_V \tag{2.4}$$

where $\dot{m}_D$ is the diffusive vapor flux.

The diffusive vapor flux is computed differently depending on the membrane pore diameter and the kinetic energy. The dominance of Knudsen or molecular diffusion varies depending on the Knudsen number Kn:

$$Kn = \frac{\lambda_m}{d} \tag{2.5}$$

where d is the membrane pore diameter. The mean free path of water vapor λ_m can be calculated by [16]

$$\lambda = \frac{k_B T}{\sqrt{2} P \pi d_w^2} \tag{2.6}$$

with k_B as the Boltzmann constant and the collision diameter $d_w = 2.641 \cdot 10^{-10}$ Å for water vapor [16]. The mean free path describes how far an average molecule travels until it collides with another molecule. At 60 °C the mean free path is around 0.3 µm [22]. When the membrane diameter is smaller than the mean free path, collisions with the membrane wall become frequent and Knudsen diffusion is the governing diffusion mechanism. Depending on the Knudsen number, the following assumptions can be made regarding the diffusive vapor flux:

- $Kn > 1 \rightarrow$ Knudsen diffusion dominant: $\dot{m}_D = \dot{m}_{D,K}$
- $Kn < 0.01 \rightarrow$ molecular diffusion dominant: $\dot{m}_D = \dot{m}_{D,M}$
- $0.01 < Kn < 1 \rightarrow$ transition region: $\dot{m}_D = \dot{m}_{D,T}$

In the transition region, Knudsen and molecular diffusion take place simultaneously. Both processes are driven by the partial pressure gradient. Thereby, the vapor mass flux can be calculated analogous to an electrical serial circuit as shown in Fig. 2.2 [18].

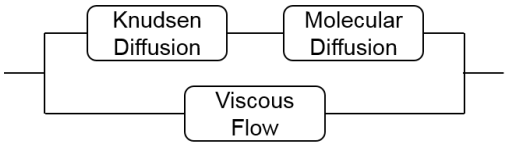

Figure 2.2: *Combination of the different mass transfer mechanisms in an electrical circuit analogy*

The diffusive vapor mass flux in the transition region $\dot{m}_{D,T}$ can be calculated as follows.

$$\dot{m}_{D,T} = \left[\frac{1}{\dot{m}_{D,K}} + \frac{1}{\dot{m}_{D,M}} \right]^{-1} \tag{2.7}$$

$$\dot{m}_{D,T} = -\frac{\epsilon}{\tau R T} \left[\left(\frac{2r}{3} \sqrt{\frac{8RTM}{\pi}} \right)^{-1} + \left(\frac{PMD_{v,a}}{p_{a,m}} \right)^{-1} \right]^{-1} \nabla p \tag{2.8}$$

The total vapor mass flux in the transition region results in:

$$\dot{m} = -\frac{\epsilon}{\tau R T} \left[\left(\frac{2r}{3} \sqrt{\frac{8RTM}{\pi}} \right)^{-1} + \left(\frac{PMD_{v,a}}{p_{a,m}} \right)^{-1} \right]^{-1} \nabla p - \frac{\epsilon r^2 M p}{8 \tau R T \mu} \nabla P \tag{2.9}$$

2.2. Mass Transfer in Air-gap Membrane Distillation

In DCMD, the vapor pressure difference across the membrane can be easily determined by the Antoine equation which states that the saturation vapor pressure is only a function of temperature. The Antoine equation can be applied at both sides of the membrane being in contact with liquid. In AGMD, the cold side of the membrane is not in contact with the coolant and therefore the partial vapor pressure can not be determined by assuming saturated air. This assumption is, however, valid at the interface of the air-gap with the liquid film. The partial vapor pressure gradient is therefore applied between the evaporation and the condensation interface (Fig. 2.3). Only molecular diffusion is assumed through the membrane which is combined with diffusion through the air-gap in [21]

$$\dot{m} = -\frac{D_{v,a}\, M\, P}{R\, T\, p_{a,m}} \left(\frac{\epsilon}{\tau\, d_{mem}} + \frac{1}{d_{air}} \right) \Delta p \tag{2.10}$$

where d_{mem} is the thickness of the membrane and d_{air} the thickness of the air-gap respectively.

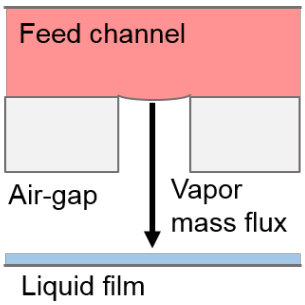

Figure 2.3: *Illustration of mass transfer in AGMD modeling*

2.3. Heat Transfer

Heat is transferred through the membrane via conduction (sensible heat) and latent heat [11]. In Fig. 2.4 the heat transfer mechanisms are illustrated. The latent heat $\dot{q}_L$ is used for the evaporation of water vapor:

$$\dot{q}_L = \dot{m} \cdot h_d \tag{2.11}$$

with h_d as the specific latent heat of evaporation.

The sensible heat $\dot{q}_S$ is considered a heat loss mechanism as it reduces the heat available for the evaporation of water vapor. It is calculated using an overall conductivity λ_{mem} for the membrane which is determined according to the porosity [16, 19]

$$\lambda_{mem} = \epsilon\, \lambda_{PVDF} + (1-\epsilon)\, \lambda_{air} \tag{2.12}$$

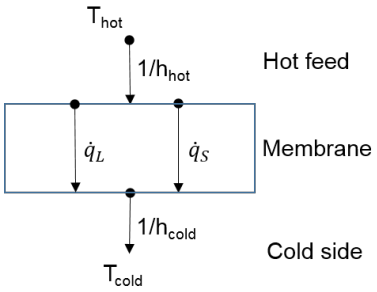

Figure 2.4: *Heat transfer through the membrane*

with the index $PVDF$ for the membrane material and air for the air in the membrane.

The convective heat transfer through the boundary layer in the hot feed and coolant channels is usually considered with Nusselt correlations for the heat transfer coefficient h_{hot} and h_{cold} [19]. When computing the feed and coolant channel in 2D, also conjugate heat transfer models have been used [23].

Chapter 3

Two New Models for Heat Transfer in the Membrane

This chapter displays an addition to Paper A and the study of chapter 2 *Numerical Model* in Paper A is recommended beforehand as the energy conservation equation at the interface is introduced there.

Two different heat transfer models are tested with different levels of detail to determine which level is sufficient or how accurate the modeling of the heat and mass transfer through the membrane needs to be. In both models, the following temperatures must be defined. The temperature in the hot feed water T_{hot} and the air-gap T_{air} near the membrane are given from the solution of the energy equation in the respective domains. The temperature at the interface T_{int} is written $T_{int,evap}$ in Paper A but is shortened here for brevity reasons. T_{int} needs to be determined for the mass transfer through the membrane as the saturation vapor pressure and the diffusive membrane flux are a function of T_{int}. Also the evaporation rate is calculated by an energy balance over the interface for which T_{int} must be known. Furthermore, the membrane temperature T_{mem} is needed for the computation of the diffusive flux through the membrane.

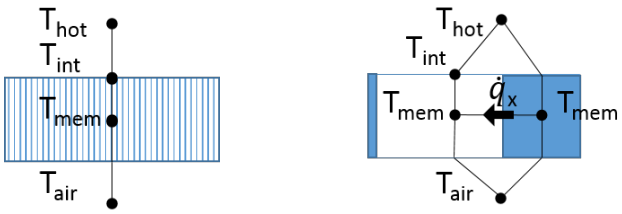

(a) *Simple Model* **(b)** *Advanced Model*

Figure 3.1: *Illustration of the heat transfer models through the membrane: (a) the simple model assumes uniform temperature layers (b) the advanced model assumes separate heat fluxes through the air and the membrane material but both have the same temperature*

3.1. Simple Model

The simple model is based on the state-of-the-art heat transfer model presented in Chapter 2.3 with the modification that the latent heat is not considered parallel to the conductive heat flux through the membrane but at the evaporation interface. The simple

model assumes continuous heat transfer through uniform temperature layers in the membrane (Fig. 3.1a). The properties are interpolated between the properties of air and the membrane material according to the porosity (Eq. 2.12). For the following derivation, the diffusion coefficient C is introduced and the expression for the diffusive membrane flux (Eq. 9 in Paper A) is reduced to the following:

$$\dot{m}_{evap} = C\left(p_{sat}\left(T_{int}\right) - p_{air}\right) \tag{3.1}$$

where p_{air} is the partial vapor pressure on the bottom side of the membrane.

The interface temperature T_{int} is located on top of the membrane. Combining the expressions for the diffusive membrane flux and evaporation mass flux (Eq. 7 and 9 in Paper A) an implicit expression for T_{int} can be derived:

$$\begin{aligned} C \cdot p_{sat}\left(T_{int}\right) + \frac{\epsilon}{h_d}\left(\frac{2\lambda_{hot}}{d_{hot}} + \frac{1}{\frac{d_{mem}}{\lambda_{mem}} + \frac{d_{air}}{2\lambda_{air}}}\right) T_{int} \\ = C \cdot p_{air} + \frac{\epsilon}{h_d}\left(\frac{2\lambda_{hot}}{d_{hot}} T_{hot} + \frac{1}{\frac{d_{mem}}{\lambda_{mem}} + \frac{d_{air}}{2\lambda_{air}}} T_{air}\right) \end{aligned} \tag{3.2}$$

3.2. Advanced Model

In the advanced model, the heat transfer through the membrane is calculated in parallel through the air and the membrane material under the assumption that both air and membrane material have the same temperature T_{mem} as it is steady-state. The heat flowing through the membrane material and the air respectively are not equal even though the temperature in the membrane is the same in both domains. For this assumption to hold true, a heat flux from the membrane material to the air in the membrane $\dot{q}_x$ is introduced. The interface temperature T_{int} is defined as the temperature between hot feed and air in the membrane. The energy balance for the air and the membrane material in the membrane reads

$$-\dot{q}_x = \epsilon \frac{2\lambda_{air}}{d_{mem}}\left(T_{int} - T_{mem}\right) + \epsilon \frac{2\lambda_{air}}{d_{mem} + d_{air}}\left(T_{air} - T_{mem}\right) \tag{3.3}$$

$$\dot{q}_x = (1-\epsilon)\frac{1}{\frac{d_{hot}}{2\lambda_{hot}} + \frac{d_{mem}}{2\lambda_{PVDF}}}\left(T_{hot} - T_{mem}\right) + (1-\epsilon)\frac{1}{\frac{d_{mem}}{2\lambda_{PVDF}} + \frac{d_{air}}{2\lambda_{air}}}\left(T_{air} - T_{mem}\right) \tag{3.4}$$

with λ_{PVDF} as the thermal conductivity of the membrane material.

Combining Eq. 3.3 and 3.4, an expression for T_{mem} as function of T_{int} can be written:

$$T_{mem} = \frac{\frac{\lambda_{air}\epsilon}{d_{mem}} T_{int} + \frac{1-\epsilon}{\frac{d_{hot}}{\lambda_{hot}} + \frac{d_{mem}}{\lambda_{PVDF}}} T_{hot} + \left(\frac{1-\epsilon}{\frac{d_{mem}}{\lambda_{PVDF}} + \frac{d_{air}}{\lambda_{air}}} + \frac{\epsilon\lambda_{air}}{d_{mem}+d_{air}}\right) T_{air}}{\frac{1-\epsilon}{\frac{d_{hot}}{\lambda_{hot}} + \frac{d_{mem}}{\lambda_{PVDF}}} + \frac{1-\epsilon}{\frac{d_{mem}}{\lambda_{PVDF}} + \frac{d_{air}}{\lambda_{air}}} + \frac{\epsilon\lambda_{air}}{d_{mem}} + \frac{\epsilon\lambda_{air}}{d_{mem}+d_{air}}} \tag{3.5}$$

The energy conservation over the evaporation interface reads for the advanced model:

$$\dot{m}_{evap} \cdot h_d = \epsilon \frac{2\lambda_{hot}}{d_{hot}} (T_{hot} - T_{int}) - \epsilon \frac{2\lambda_{air}}{d_{mem}} (T_{int} - T_{mem}) \tag{3.6}$$

Combining Eq. 3.1 and 3.6 gives:

$$C \cdot p_{sat}(T_{int}) + \frac{2\epsilon}{h_d} \left(\frac{\lambda_{hot}}{d_{hot}} + \frac{\lambda_{air}}{d_{mem}} \right) T_{int} = C \cdot p_{air} + \frac{2\epsilon}{h_d} \left(\frac{\lambda_{hot}}{d_{hot}} T_{hot} + \frac{\lambda_{air}}{d_{mem}} T_{mem} \right) \tag{3.7}$$

Finally, an implicit equation for T_{int} can be written:

$$\begin{aligned} C \cdot p_{sat}(T_{int}) + \frac{2\epsilon}{h_d} \left[\frac{\lambda_{hot}}{d_{hot}} + \frac{\lambda_{air}}{d_{mem}} \left(1 - \frac{\epsilon \lambda_{air}}{d_{mem} \cdot denom} \right) \right] T_{int} \\ = C \cdot p_{air} + \frac{2\epsilon}{h_d} \left[\left(\frac{\lambda_{hot}}{d_{hot}} + \frac{(1-\epsilon)\lambda_{air}}{d_{mem} \cdot denom \left(\frac{d_{hot}}{\lambda_{hot}} + \frac{d_{mem}}{\lambda_{PVDF}} \right)} \right) T_{hot} \right. \\ \left. + \frac{\lambda_{air}}{d_{mem} \cdot denom} \left(\frac{1-\epsilon}{\frac{d_{mem}}{\lambda_{PVDF}} + \frac{d_{air}}{\lambda_{air}}} + \frac{\epsilon \lambda_{air}}{d_{mem} + d_{air}} \right) T_{air} \right] \end{aligned} \tag{3.8}$$

$$denom = \frac{1-\epsilon}{\frac{d_{hot}}{\lambda_{hot}} + \frac{d_{mem}}{\lambda_{PVDF}}} + \frac{1-\epsilon}{\frac{d_{mem}}{\lambda_{PVDF}} + \frac{d_{air}}{\lambda_{air}}} + \frac{\epsilon \lambda_{air}}{d_{mem}} + \frac{\epsilon \lambda_{air}}{d_{mem} + d_{air}} \tag{3.9}$$

A cell averaged temperature $T_{mem,top,advanced}$ on top of the membrane is calculated according to Eq. 3.10 for the advanced model and is used as a boundary condition for the hot feed water domain. The membrane material top temperature $T_{PDVF,top}$ is calculated according to the resistances in series between T_{mem} and T_{hot}.

$$T_{mem,top} = \epsilon \cdot T_{int} + (1-\epsilon) \cdot T_{PVDF,top} \tag{3.10}$$

3.3. Comparison of the Models

The 70 °C validation simulation from Paper A is used to compare both models. The vertical temperature distribution in the membrane for the simple and advanced model are shown in Fig. 3.2. In the figures, the temperature in the last half air cell, the membrane and the first half feed water cell is shown. The temperature values are averaged over the complete membrane area.

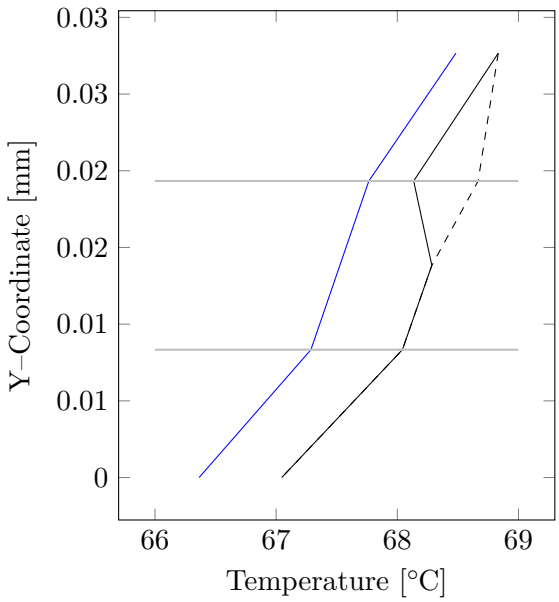

Figure 3.2: *Vertical temperature distribution in membrane and half adjacent domain cells:* —— *simple model,* —— *air in advanced model,* - - - *membrane material in advanced model*

The membrane averaged interface temperature is 67.77 °C for the simple model and 68.14 °C for the advanced model respectively. The combined temperature on the membrane top for the advanced model $T_{mem,top}$ is 68.27 °C. The relative difference between the interface temperatures is 0.5%. The compensation heat flux $\dot{q}_x$ is $237.54\frac{W}{m^2}$ or $0.3712 \cdot 10^{-3} \frac{W}{\text{computational cell}}$.

As the temperature difference is not significant between the two models, the simple model is used in the computation because of the reduced complexity. However, the advanced model remains in the code and can be easily employed.

Chapter 4

Summary of contributions

A synopsis of the appended papers can be given as follows:

Paper A: Implementation and validation of a 3D CFD model for flat-sheet AGMD with special emphasis on the heat and mass transfer during evaporation and condensation

Paper B: Mapping of the 3D structure of three commercial state-of-the-art PTFE membranes in MD with ptychographic X-ray computed tomography, computation of the flow field in the samples via Lattice-Boltzmann simulation and investigation of the membrane transport properties

Paper C: Comparison of two modules where the temperature gradient is parallel or opposing gravity and study of buoyancy effects in the latter module, furthermore extension of the salt modeling in the numerical model of Paper A and comparison of tap water and seawater as feed

Paper D: Porting of the bi-conjugate gradient stabilized (bicgstab) method from the CFD tool of Paper A to run on Graphical Processing Units (GPU) and quantification of the speed-up

4.1. Paper A

A Three-Dimensional Model for the Heat and Mass Transfer in Air-gap Membrane Distillation

The extent of the model is shown in Fig. 4.1a. The velocity and temperature field is obtained in 3D by solving the incompressible Navier-Stokes and energy equation in the hot water channel, the air-gap and the coolant channel. A salt concentration equation is solved in the hot water channel which decreases the saturation vapor pressure at the evaporation interface. The membrane modeling combines the energy conservation during evaporation with the diffusive vapor transport and thermal conduction in the membrane (Knudsen and molecular). Thereby, the temperature profile and mass flux through the membrane is obtained. Also at the liquid film, the condensation mass flux is obtained from energy conservation assuming saturated air. By solving a conservation equation for the vapor in the air-gap, the effects of natural convection on the vapor mass transfer in the air-gap are considered. The temperature profile in the liquid film is computed in 3D while the heat transfer through the steel plate is computed with the 1D heat resistance in series approach.

The model is validated against experimental data from Banat [24]. Variations of the heat and mass transfer along the flow direction of the hot feed water are visible (Fig. 4.1b). It is observed that the evaporation interface temperature at the membrane is dominant for the heat and mass transfer in the module. Furthermore, natural convection in the air-gap is found.

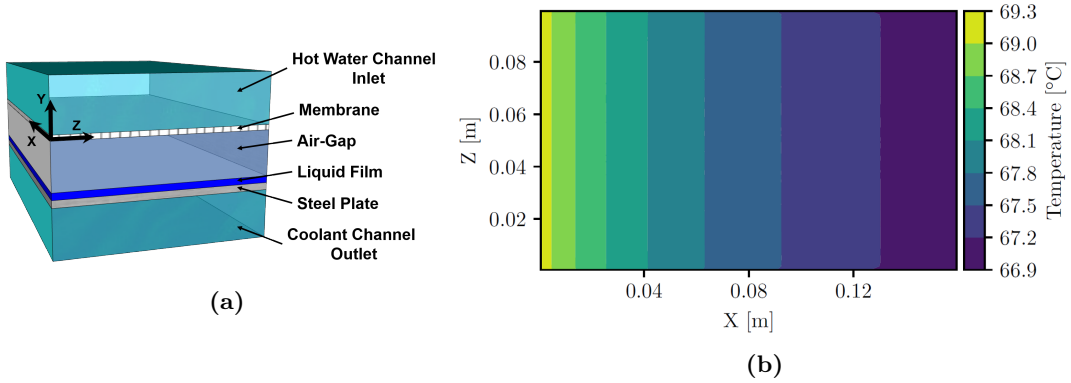

Figure 4.1: *(a) Domains included in the model (not to scale) (b) Evaporation interface temperature at the membrane [25]*

4.2. Paper B

Three-dimensional membrane imaging with X-ray ptychography: determination of membrane transport properties for membrane distillation

Three state-of-the-art MD membranes are mapped using X-ray ptychography and their 3D structures are obtained. In total, four membrane samples are analyzed. Using these structures, the flow field is calculated driven by a pressure gradient using LB computation. In this way, porosity, tortuosity and permeability values are determined. A comparison between the computed intrinsic permeability and the DGM is presented. Additionally, the apparent permeability as a function of Knudsen number is computed which includes a correction for velocity slip effects at the solid boundaries. It is found that the porosity agrees well with the porosity specified by the manufacturer for three of the samples. The porosity of one sample is below the specified manufacturer value. Considering the porosity across slices perpendicular to the main flow direction, variations are observed. Closer to the PP grid, the porosity is increased compared to the mean value while it is reduced on the free surface. The tortuosity lies for all membrane samples slightly above 2. The intrinsic permeability is in the same order of magnitude as predicted by the DGM for three samples. For the membrane sample with the larger pore diameter, the DGM predicts the permeability to be one order of magnitude higher which is not reflected in the computations. Similar to the porosity, also the permeability is increased closer to the PP grid compared to the overall membrane height. Interestingly, for all four samples the apparent permeability is closer to the permeability predicted by the DGM in the range of Knudsen numbers common in MD. This is surprising as the DGM calculates an intrinsic permeability. The discrepancy between DGM and computed permeability needs therefore to be better understood and a physical explanation investigated, especially for the membrane sample with larger pore diameter. Furthermore, it is found that averaging the results of few smaller membrane volumes yields to the same results as analyzing the full mapped volume.

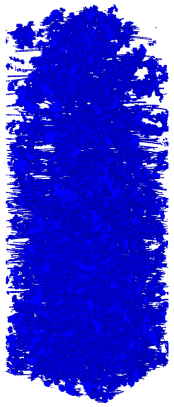

Figure 4.2: *Representation of the segmented tomogram and domain for the computation of the membrane transport properties [26]*

4.3. Paper C

Module Orientation for Performance and Energy Efficiency in Air-gap Membrane Distillation

Two AGMD module configurations are numerically compared and their performance at different feed inlet temperatures, velocities and air-gap thicknesses evaluated. In the upside configuration the hot feed flows above the membrane, while in the downside configuration it flows below the air-gap and membrane. In the latter, the feed solution is not in contact with the membrane but separated by the air-gap which is expected to improve the fouling resistance of the membrane. Buoyancy effects are included by considering temperature depended density and gravity in the incompressible Navier-Stokes equation. As feed, both tap water and sea water are studied and compared. In order to do so, the model is extended to compute salt concentration boundary layers which form due to evaporation of vapor and an increase in salt concentration. Also the density is computed as a function of temperature and salt concentration. For the downside configuration, the velocity profile in the air-gap due to buoyancy is visualized (Fig. 4.3). It is found that the downside configuration is less susceptible to feed inlet velocity variations than the upside configuration. The vortex formation in the air-gap is favored by low feed velocities which results for smaller air-gaps in an increased energy utilization. In general, the energy utilization of the downside module is consistently and significantly higher indicating that less energy is needed to distill the same permeate flux compared to the upside configuration. As the main advantage of AGMD is the reduction of heat losses, the downside configuration could bring further improvement in this direction. For low salinities like sea water, the salt boundary layer is thinner than the temperature boundary layer and its impact is visible but not yet predominant. The modification implemented in this study orients the model in the direction of studying the treatment of highly saline brines.

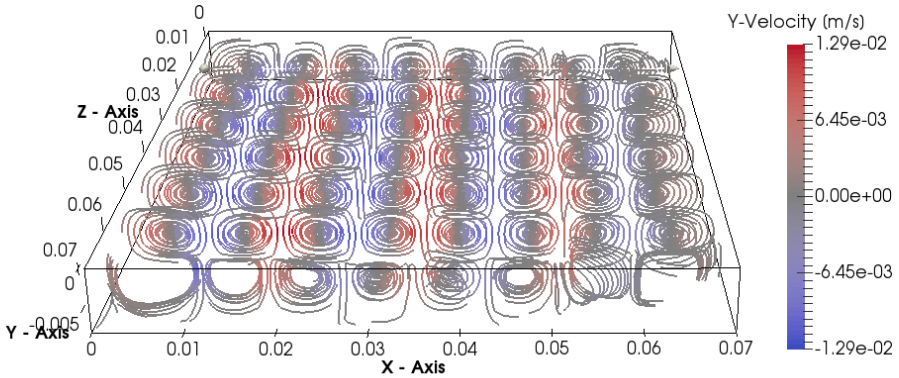

Figure 4.3: *Streamlines in the air-gap for downside configuration for 80 °C hot water inlet temperature and 8 mm air-gap [27]*

4.4. Paper D

Speed-up Using GPU Accelerators: How to Port a Numerical Solver for CFD with PyCUDA

The finite-volume CFD code of Paper A solves the incompressible Navier-Stokes equation. To obtain the velocity and pressure field, both momentum conservation and pressure correction equations are discretized forming a system of linear equations which needs to be solved for every time step. This results in a large system of linear equations growing with the refinement of the grid and the size of the physical problem. Numerous linear equations are solved significantly faster with numerical, iterative methods. Using these methods, the problem is reduced to multiple matrix multiplications with big matrices which fits well the architecture of GPUs. Therefore, the implementation of the bi-conjugate gradient stabilized (bicgstab) method for the CFD code in Paper A is ported to run on GPU. As the CFD code is implemented in Python, the PyCUDA module is used to translate Python code into NVIDIA CUDA kernels to achieve a speed-up of the overall execution time. The speed-up of the final implementation is tested by comparing the run time of a test case with different grid refinements calculated both on GPU and Central Processing Units (CPU). From a certain mesh size on, the computation on GPU is faster (Fig. 4.4) and the time advantage is significantly increasing with mesh size. Unfortunately, as the AGMD model consists of multiple domains and the equations are discretized per domain, the matrices to be solved in Paper A and C are smaller than the threshold matrix where computation on the GPU becomes faster. Also, for computational cells with a high aspect ratio as in Paper A, the conjugate gradient solver is more robust than bicgstab and therefore advisable. However, the option of computing with bigcstab on GPU remains in the CFD code for the case that larger modules will be computed in the future.

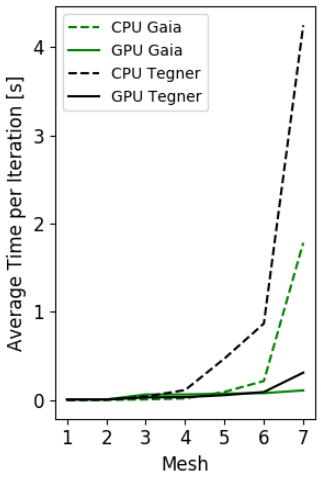

Figure 4.4: *Comparison of the average time spent per iteration in bicgstab for different mesh sizes computed on CPU and GPU [28]*

Chapter 5

Directions for future research

Study ideas to continue the modeling of AGMD and to employ the modeling approaches developed in this thesis are presented in the following.

Advancement of the macro-scale model in Paper A

In the macro-scale model, the liquid film thickness is assumed to be constant and the discharge of the module to be equal to the condensation mass flow. Especially for thin air-gaps, the permeate tends to flood the air-gap if the discharge is lower than the condensation [29]. To study air-gap flooding and appropriate discharge designs, a varying liquid film thickness is to be implemented in the model depending on the condensation mass flow. This modification is expected to be possible but challenging.

Effective diffusivity of membrane samples in Paper B

In Paper B, permeability values are calculated from the flow field in the membrane samples. The knowledge of permeability values is essential for modules with non-negligible total pressure gradient across the membrane. In AGMD, however, diffusive processes outweigh viscous flow. Effective diffusivity values can be calculated by applying a concentration gradient across the membrane. In the computation, Knudsen effects should be considered. As the computation of the diffusivity requires significantly more computational resources than the permeability computation, analyzing few smaller membrane volumes might be required for feasibility. As noted in Paper B, averaging the results of few smaller membrane volumes yields to the same results as analyzing the full mapped volume. This circumstance might make diffusivity calculations feasible. Furthermore, it should be noted that diffusion is a temperature dependent process. The knowledge of the effective diffusivity as a function of temperature would eliminate the need of applying the DGM and assuming uniform, cylindrical cavities for the analyzed membranes. It would also allow to reduce modeling uncertainties in the macro-scale model of Paper A.

Module optimization study

Paper C opened the ground for a numerical optimization study investigating phenomena which might be difficult to visualize experimentally. Nevertheless, experimental

validation need to be performed for the findings in Paper C.

To study more complex geometries than possible with the Cartesian grid in the macro-scale model, isothermal computations of the velocity field can be performed using commercial CFD software. For the modeling of the feed water flow, the evaporation mass flux can be assumed negligible which justifies this procedure [30]. The macro-scale model can then be applied to compute energy efficiency and permeate flux of the module as the temperature profile in the module depends highly on the heat and mass transfer through the membrane which is included in the macro-scale model.

Mixing in the feed channel is found to reduce boundary layers and enhance the heat and mass transfer from the feed to the membrane [31]. This can be achieved by including spacers in the feed channel or having the feed flowing in the turbulent region. In this thesis, laminar flow conditions have been considered and investigated. A numerical study on turbulent and/or spacer-induced mixing with different spacer designs could be beneficial for the design of efficient AGMD modules.

Treatment of highly saline brines

MD is insusceptible to feed concentration and therefore considered promising for the further treatment of brines from RO in the direction of achieving zero liquid discharge [32]. However, especially when treating highly saline brines, salts tend to deposit on the membrane which reduces the membrane performance [33]. Simulations of membrane scaling can be therefore performed on both magnitude scales: on micro-scale the growth of salt on the membrane and the membrane blockage can be modeled ideally leading to a model for the scaling rate depending on the thermodynamic conditions. On the macro-scale, this scaling rate can be used to investigate the influence of scaling on the heat and mass transfer and on the thermodynamic conditions in long-term operation.

Chapter 6

Concluding remarks

The present thesis is concerned with the numerical modeling of AGMD. The overall goal is to increase the understanding of the AGMD process and the predictive power of numerical models. For this purpose two magnitude scales are investigated: (i) on a macro-scale, the AGMD process on module level is modeled and (ii) on a micro-scale, the transport properties of the membrane are investigated in order to reduce fitting parameter and uncertainties for the modeling on the macro-scale. Four studies are performed in order to address these challenges, three of which focus on the development of the macro-scale model and one on the determination of membrane transport properties. These studies are included in the thesis in the form of appended Papers A–D.

The main advantage of the macro-scale model lies in the combination of 3D CFD with detailed heat and mass transfer modeling. It integrates aspects from multiphase flow modeling namely energy conservation over phase-change interfaces and the thermodynamic concept of moist air in the air-gap. The condensation mass flow is calculated independently from the evaporation mass flow. Thereby, it allows to study convection phenomena in the air-gap as presented in Paper C which are not represented in the state-of-the-art modeling approach. Vortexes in the air-gap are observed when employing a module configuration where the hot feed flows below air-gap and membrane and the temperature gradient is opposing gravity. These vortexes lead to a significantly increased energy utilization. As the main advantage of AGMD is the reduction of heat losses, this configuration could bring further improvement. Further experimental validation is required to reinforce the findings. Also, a modeling approach for salt boundary layers is proposed that form due to the evaporation of vapor. The influence of these salt boundary layers on the density distribution of the feed is shown to be minor in the case of seawater which is expected to increase when treating highly saline brines. For the investigation of larger modules and/or higher resolution, acceleration on GPUs is implemented in the model and documented in Paper D.

The combination of X-ray ptychography and LB simulation proved appropriate for the characterization of membrane transport properties as shown in Paper B. Thereby, the 3D structure of membrane samples was obtained and porosity, tortuosity and permeability values were computed for the investigated membranes. Especially, since the membrane properties can be determined by analyzing and averaging a few smaller sample volumes, membrane samples of reduced size can be analyzed which decreases beam damage and computational resources making this combination more viable. The computation of

membrane diffusivity values from the 3D membrane samples may become feasible under this assumption.

Areas for future research are identified based on the findings in Paper A–D. Advances to continue the module optimization study are proposed. On the other hand, MD gains advantage at treating highly saline brines for which both, micro-scale and macro-scale model, can be applied to better understand scaling phenomena. The application of the models leads the way to hopefully better performing and more energy-efficient module designs.

References

1. *Coping with water scarcity. Challenge of the twenty-first century* (UN-Water and FAO, FAO, 2007).
2. *The United Nations World Water Development Report 4* (UNESCO, United Nations World Water Assessment Programme (WWAP), and UN-Water, Mar. 2012).
3. Al-Karaghouli, A. & Kazmerski, L. L. Energy consumption and water production cost of conventional and renewable-energy-powered desalination processes. *Renewable and Sustainable Energy Reviews* **24,** 343–356 (2013).
4. Ettouney, H. in *Seawater Desalination Conventional and Renewable Energy Processes* (eds Cipollina, A., Micale, G. & Rizzuti, L.) 17–40 (Springer, Heidelberg, 2007).
5. Chaibi, M. T. & El-Nashar, A. M. in *Seawater Desalination Conventional and Renewable Energy Processes* (eds Cipollina, A., Micale, G. & Rizzuti, L.) 131–163 (Springer, Heidelberg, 2007).
6. Alkhudhiri, A., Darwish, N. & Hilal, N. Membrane distillation: A comprehensive review. *Desalination* **287.** Special Issue in honour of Professor Takeshi Matsuura on his 75th Birthday, 2–18 (2012).
7. Khayet, M. & Matsuura, T. in *Membrane Distillation* (eds Khayet, M. & Matsuura, T.) 1–16 (Elsevier, Amsterdam, 2011).
8. Koschikowski, J., Wieghaus, M. & Rommel, M. Solar thermal-driven desalination plants based on membrane distillation. *Desalination* **156.** Joint EDS, WSTA and IWA conference on Desalination and the Environment Fresh Water for All UN International Year of Fresh Water 2003, 295–304 (2003).
9. Camacho, L. M., Dumée, L., Zhang, J., Li, J.-d., Duke, M., Gomez, J. & Gray, S. Advances in Membrane Distillation for Water Desalination and Purification Applications. *Water* **5,** 94–196 (2013).
10. Summers, E. K., Arafat, H. A. & Lienhard, J. H. Energy efficiency comparison of single-stage membrane distillation (MD) desalination cycles in different configurations. *Desalination* **290,** 54–66 (2012).
11. Lawson, K. W. & Lloyd, D. R. Membrane distillation. *Journal of Membrane Science* **124,** 1–25 (1997).

12. Khayet, M. & Matsuura, T. in *Membrane Distillation* (eds Khayet, M. & Matsuura, T.) 295–322 (Elsevier, Amsterdam, 2011).

13. Khayet, M. & Matsuura, T. in *Membrane Distillation* (eds Khayet, M. & Matsuura, T.) 323–359 (Elsevier, Amsterdam, 2011).

14. Khayet, M. & Matsuura, T. in *Membrane Distillation* (eds Khayet, M. & Matsuura, T.) 361–398 (Elsevier, Amsterdam, 2011).

15. Saffarini, R. B., Summers, E. K., Arafat, H. A. & Lienhard V, J. H. Technical evaluation of stand-alone solar powered membrane distillation systems. *Desalination* **286,** 332–341 (2012).

16. Khayet, M. Membranes and theoretical modeling of membrane distillation: A review. *Advances in Colloid and Interface Science* **164.** Membrane Separation and Colloid Science, 56–88 (2011).

17. Alklaibi, A. & Lior, N. Membrane-distillation desalination: Status and potential. *Desalination* **171,** 111–131 (2005).

18. Mason, E. & Malinauskas, A. *Gas transport in porous media: the dusty-gas model Chemical engineering monographs* **Bd. 17** (Elsevier, 1983).

19. Hitsov, I., Maere, T., De Sitter, K., Dotremont, C. & Nopens, I. Modelling approaches in membrane distillation: A critical review. *Separation and Purification Technology* **142,** 48–64 (Mar. 2015).

20. Shirazi, M. M. A., Kargari, A., Ismail, A. F. & Matsuura, T. Computational Fluid Dynamic (CFD) opportunities applied to the membrane distillation process: State-of-the-art and perspectives. *Desalination* **377,** 73–90 (Jan. 2016).

21. Alklaibi, A. & Lior, N. Transport analysis of air-gap membrane distillation. *Journal of Membrane Science* **255,** 239–253 (2005).

22. Schofield, R., Fane, A. & Fell, C. Heat and mass transfer in membrane distillation. *Journal of Membrane Science* **33,** 299–313 (1987).

23. Janajreh, I., Suwwan, D. & Hashaikeh, R. Assessment of direct contact membrane distillation under different configurations, velocities and membrane properties. *Applied Energy* **185.** Clean, Efficient and Affordable Energy for a Sustainable Future, 2058–2073 (2017).

24. Banat, F. A. *Membrane distillation for desalination and removal of volatile organic compounds from water* en. OCLC: 46510663. PhD thesis (McGill University, Montreal, Canada, 1994).

25. Cramer, K., Niceno, B., Prasser, H.-M. & Leyer, S. A Three-Dimensional Model for the Heat and Mass Transfer in Air-gap Membrane Distillation. *Submitted for publication* (2019).

26. Cramer, K., Prasianakis, N. I., Niceno, B., Ihli, J., Holler, M. & Leyer, S. Three-dimensional membrane imaging with X-ray ptychography: determination of membrane transport properties for membrane distillation. *To be submitted* (2019).

27. Cramer, K., Lamesch, P., Dalle, M.-A., Niceno, B. & Leyer, S. Module Orientation for Performance and Energy Efficiency in Air-gap Membrane Distillation. *To be submitted* (2019).

28. Cramer, K. & Manzari, L. *Speed-up Using GPU Accelerators: How to Port a Numerical Solver for CFD with PyCUDA* 2018.

29. Warsinger, D. M., Swaminathan, J., Morales, L. L. & Lienhard V, J. H. Comprehensive condensation flow regimes in air gap membrane distillation: Visualization and energy efficiency. en. *Journal of Membrane Science* **555,** 517–528 (June 2018).

30. Bouguecha, S., Chouikh, R. & Dhahbi, M. Numerical study of the coupled heat and mass transfer in membrane distillation. *Desalination* **152,** 245–252 (2003).

31. Yun, Y., Wang, J., Ma, R. & Fane, A. G. Effects of channel spacers on direct contact membrane distillation. *Desalination and Water Treatment* **34,** 63–69 (2011).

32. Tong, T. & Elimelech, M. The Global Rise of Zero Liquid Discharge for Wastewater Management: Drivers, Technologies, and Future Directions. *Environmental Science & Technology* **50,** 6846–6855 (2016).

33. Warsinger, D. M., Swaminathan, J., Guillen-Burrieza, E., Arafat, H. A. & Lienhard V, J. H. Scaling and fouling in membrane distillation for desalination applications: A review. en. *Desalination* **356,** 294–313 (Jan. 2015).

Part II

APPENDED PAPERS AND REPORTS

Paper A

A Three-Dimensional Model for the Heat and Mass Transfer in Air-gap Membrane Distillation

Kerstin Cramer[a], Bojan Niceno[b], Horst-Michael Prasser[c], Stephan Leyer[a]

[a] *University of Luxembourg, 1359 Luxembourg, Luxembourg*
[b] *Paul-Scherrer-Institute (PSI), 5232 Villigen, Switzerland*
[c] *Swiss Federal Institute of Technology (ETHZ), 8092 Zürich, Switzerland*

Abstract

Membrane distillation (MD) is a process to desalinate seawater. Pilot plants are operated aiming at increasing the modules' efficiency for large-scale application. In air-gap MD (AGMD) the state-of-the-art modeling of mass and heat transfer is one-dimensional, combining evaporation and diffusion through the membrane and the condenser channel in one correlation. In this work, a numerical model is developed which computes AGMD modules in three dimensions. For evaporation and condensation, energy conservation equations at the interfaces are solved.

Simulation results are compared to experimental data and a good agreement is found. The simulation results show flow profile variations in axial direction and therefore the advantage of multi-dimensional computations. Additionally, natural convection in the air-gap is observed. The model is intended to complement experiments to develop better performing AGMD modules.

Keywords: Air Gap Membrane Distillation, CFD, Heat and Mass Transfer, Temperature Polarization

1. Introduction

Fresh water supply is a problem in large parts of the world. According to World Health Organization (WHO), 3.5 million fatalities occur each year due to a lack of fresh drinking water while the trend is rising due to population growth [1]. Membrane distillation (MD) is considered a promising desalination technique which requires low grade heat to thermally separate potable water from sea or brackish water [2]. Other advantages include a large insensitivity to feed concentration, a high quality of produced fresh water and a higher fouling resistance than other comparable desalination techniques [3]. Despite its advantages, MD lacks the energy efficiency and the economical performance to be competitive in commercial applications [4]. Membrane distillation uses renewable energy or waste heat to desalinate feed water by generating a temperature gradient between hot salt water and colder fresh water, which are separated by a membrane. The membrane is filled with air and is hydrophobic but permeable to water vapor. Thereby, the temperature gradient leads to a gradient in partial vapor pressure across the membrane. It drives the evaporation of water at the liquid-vapor interface on the membrane top at temperatures below the boiling point. Salt is not soluble in water vapor and is therefore retained in the liquid water. Desalinated water is mostly produced by condensing the water vapor either directly into a freshwater stream (direct contact MD) or into a cooled, air-filled condenser compartment forming a liquid film at the bottom (air-gap MD). Other configurations are realized as well. Direct contact MD (DCMD) is the most studied configuration [5], while air-gap MD (AGMD) is the configuration applied in most pilot plants [4]. The insulating air-gap reduces the conductive heat flow in the module while introducing an additional mass resistance to the vapor flux [6]. A phenomenon observed in all configurations is temperature and concentration polarization. A strong temperature and concentration gradient is observed in the boundary layer of the feed stream at the membrane [7]. It is assumed to be the limiting factor for the transport efficiency [8].

Email addresses: kerstin.cramer@uni.lu (Kerstin Cramer), bojan.niceno@psi.ch (Bojan Niceno), stephan.leyer@uni.lu (Stephan Leyer)

Nomenclature

Roman letters

$\mathbf{S}$	Computational cell surface
$\mathbf{u}$	Velocity vector
$\dot{m}$	Mass flux
$\dot{q}_{a\to b}$	Heat flux from a into b
a	Concentration
c	Mole fraction
c_P	Heat capacity
d	Height
$D_{a,b}$	Diffusion coefficient of a in b
h_d	Specific latent heat of evaporation
M	Molar mass
P	Pressure
p	Partial pressure
P'	Pressure correction
R	Gas constant
r	Pore radius
T	Temperature
t	Time
V	Computational cell volume

Greek letters

ϵ	Porosity
λ	Thermal conductivity
μ	Viscosity
ψ	Temperature concentration coefficient
ρ	Density
τ	Tortuosity

Subscripts

air	Air-gap
$cond$	Condensation
$evap$	Evaporation
$film$	Liquid film
g	Gas
hot	Hot feed water channel
int	Interface
l	Liquid
mem	Membrane
s	Salt
sat	Saturation
tot	Mixture of air and vapor
v	Vapor

One-dimensional heat and mass transfer models were developed for DCMD computing the membrane flux and heat transfer through the membrane from the bulk flow parameters under consideration of temperature polarization [9]. For AGMD, the mass transfer through membrane and air-gap is combined in an one-dimensional equation [10, 11]. Summers et al. [12] extended these models to two dimensions in the hot feed and air-gap channel to compare different MD configurations in respect to their energy efficiency. Chouikh et al. [13] computed natural convection in the air-gap in two dimensions. Alklaibi and Lior [14] developed a very detailed model for an AGMD hollow fiber module. The temperature profile in the hot water channel, air-gap, liquid film, cooling plate and coolant channel is solved in two dimensions. The liquid film thickness is calculated assuming the condensation mass flux equal to the vapor flux through the membrane which is calculated using the molecular diffusion model. Thereby, diffusion in the air-gap is still one-directional. The radial temperature profile and boundary layer at different axial locations are shown indicating temperature variations in axial direction. Recently, Janajreh et al. [15] presented the axial profiles of temperature, temperature polarization, permeate mass flux and thermal efficiency in different DCMD configurations. In their study, the Navier-Stokes and energy equations were solved in two dimensions assuming Knudsen diffusion and Poiseuille flow through the membrane as in Schofield's model [16]. In a different study, they extend the model to AGMD, however, it remains unspecified how the mass transfer through the air-gap and the vapor pressure on the membrane bottom side was calculated [17].

Currently, there are no three-dimensional models which compute the heat and mass transfer in the module [18, 19]. Especially the mass transfer in the air-gap is not investigated, even though the understanding of three-dimensional

fluid-dynamical and thermodynamical phenomena would benefit the technology development. In this work, a three-dimensional model for flat-sheet AGMD is presented. Special emphasis is thereby put on the heat and mass transfer modeling of the evaporation and condensation processes. At the liquid-vapor interfaces, conjugate heat transfer models are applied satisfying the energy conservation to determine interface temperatures. They are used to calculate the evaporation and condensation mass fluxes independently. The model is compared to experimental data published by Banat [20] which have been previously used for the numerical validation [14].

2. Numerical Model

The model computes the hot feed channel, air-gap, liquid film and cooling channel in three dimensions[1]. Thereby, the conjugate heat transfer model is employed. In between, the evaporation interface, membrane, condensation interface and cooling plate are considered with one dimensional heat and mass transfer correlations applied to individual computational cells. A graphical representation of the modeled AGMD module and relevant temperature locations can be found in Fig. 1. In the following, the equations, assumptions and boundary conditions are presented.

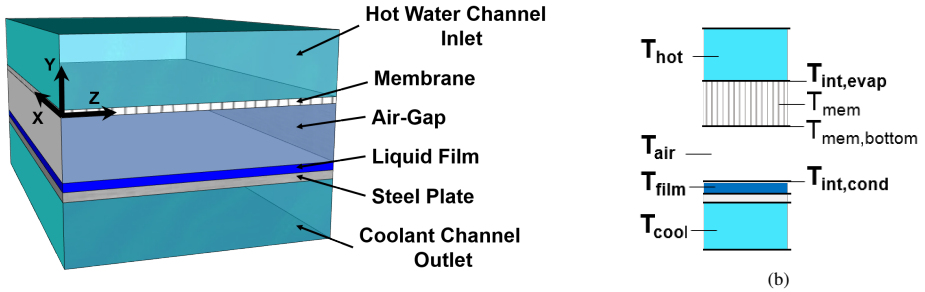

Figure 1: (a) Domains included in the model (not to scale); heat and mass transfer through the membrane and heat transfer through the steel plate are calculated in 1D, the other domains in 3D; (b) Relevant temperature locations and their naming convention

2.1. Hot Feed Channel

The Navier-Stokes (NS) and energy conservation equation are solved in three dimensions (Eq. 1 – 3). Equation 2 displays the pressure correction equation which is needed to satisfy mass conservation. Gravity is considered in the force term F. Additionally, a concentration conservation equation is solved for the salt concentration a_{salt} (Eq. 4) where $D_{s,H2O}$ is the diffusion coefficient of salt in water.

$$\int_V \frac{\partial \rho \mathbf{u}}{\partial t}\, dV + \int_S \rho \mathbf{u}\mathbf{u}\, d\mathbf{S} = \int_S \mu \nabla \mathbf{u}\, d\mathbf{S} + \int_V \nabla P\, dV + \mathbf{F} \tag{1}$$

$$\int_S \frac{\nabla P'}{\rho}\, d\mathbf{S} = \frac{1}{\Delta t} \int_S \mathbf{u}\, d\mathbf{S} \tag{2}$$

$$\int_V \frac{\partial \rho c_P T}{\partial t}\, dV + \int_S \rho \mathbf{u} c_P T\, d\mathbf{S} = \int_S \lambda \nabla T\, d\mathbf{S} \tag{3}$$

$$\int_V \frac{\partial \rho a_s}{\partial t}\, dV + \int_S \rho \mathbf{u} a_s\, d\mathbf{S} = \int_S D_{s,H2O} \nabla a_s\, d\mathbf{S} \tag{4}$$

The temperature at the inlet is assumed to be constant and uniform. The walls are modeled as adiabatic. For the temperature on the boundary to the membrane, the interface saturation temperature $T_{int,evap}$ is applied which is calculated from the energy jump condition as described in Section 2.2.

For this study, an inlet velocity profile is assumed which is parabolic in height and constant throughout the depth of the module. At the membrane side, a velocity component normal to the membrane is computed as $v = \dot{m}_D/\rho_{H2O}$ from the membrane vapor flux and the density of the feed water.

[1]The source code can be found at `https://github.com/kjcramer/pyns/tree/validation_study`

2.2. Evaporation Interface and Membrane

Energy Conversation at Interface

The energy conversation at the interface is developed for the modeling of multiphase flows and combines the heat and mass transfer including the latent heat across a liquid-vapor interface. It dictates that all heat fluxes transfered from the liquid to the interface must leave the interface either by conduction to the vapor phase or evaporation as the interface has no thermal inertia. This is illustrated in Fig. 2 and translates into Eq. 5 where the simplified temperature naming of Fig. 2 is applied.

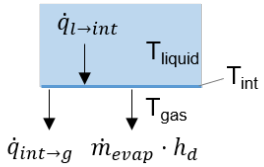

Figure 2: Illustration of heat fluxes and temperatures at the interface; as there is no thermal inertia in the interface, all heat fluxes must balance out

$$\dot{q}_{l\to int} = \dot{q}_{int\to g} + \dot{m}_{evap} \cdot h_d \tag{5}$$

Fourier's law is used to determine the heat flux from the liquid phase to the interface $\dot{q}_{l\to int}$ and from the interface to the gaseous phase $\dot{q}_{int\to g}$ (Eq. 6).

$$\dot{q}_{l\to int} = \frac{\lambda_l}{d_l}\left(T_l - T_{int}\right) \tag{6}$$

Combining Eq. 5 and 6 and applying it on the AGMD module, an equation is obtained which relates the interface temperature and the evaporation mass flux at a given hot salt water and air-gap temperature (Eq. 7). The distance from the point where the temperature T_{hot} is defined to the interface is only $d_{hot}/2$ and therefore the factor 2 needs to be included. The same holds true on the air side.

$$\dot{m}_{evap} \cdot h_d = \epsilon \frac{2\lambda_{hot}}{d_{hot}}\left(T_{hot} - T_{int,evap}\right) - \epsilon \frac{1}{\frac{d_{mem}}{\lambda_{mem}} + \frac{d_{air}}{2\lambda_{air}}}\left(T_{int,evap} - T_{air}\right) \tag{7}$$

The thermal conductivity of the membrane λ_{mem} is calculated as

$$\lambda_{mem} = \epsilon\lambda_{air} + (1-\epsilon)\,\lambda_{PVDF} \tag{8}$$

Membrane Flux

The membrane flux is calculated applying the Dusty-Gas Model. The Knudsen number is in the order of unity for the pore diameter and temperature considered and therefore Knudsen and molecular diffusion are considered. Viscous flow can be neglected as the total pressure difference across the membrane is negligible. Membrane flux is calculated according to Eq. 9.

$$\dot{m}_{mem} = -\frac{\epsilon}{\tau R T_{mem}}\left[\left(\frac{2r}{3}\sqrt{\frac{8RT_{mem}M_v}{\pi}}\right)^{-1} + \left(\frac{PM_vD_{v,air}}{p_{air}}\right)^{-1}\right]^{-1}\nabla p \tag{9}$$

The partial pressure gradient across the membrane is considered between the evaporation interface and the bottom of the membrane where the vapor content is assumed to be equal to the one in the adjacent air cell.

From the ideal gas law and the definition of a_v as the mass fraction of vapor to vapor and air mixture, an expression for the vapor pressure in function of vapor content can be derived (Eq. 10).

$$p = a_v \frac{M_{tot}}{M_{H_2O}} P \qquad M_{tot} = \frac{1}{\frac{1-a_v}{M_{air}} + \frac{a_v}{M_{H_2O}}} \tag{10}$$

At the interface, the air is assumed to be saturated and the partial vapor pressure p is therefore determined by the Antoine equation from the interface temperature T_{int} (Eq. 11). The coefficients are taken from Bridgeman and Aldrich [21] for the corresponding temperature range (Eq. 11). The pressure is in bar and the temperature in K. Raoult's law is applied to account for the boiling point elevation due to the presence of salt (Eq. 12).

$$\log_{10} p^0_{sat} = \left(A - \frac{B}{T_{int,evap} - C} \right) \tag{11}$$

$$p_{sat} = p^0_{sat} \, (1 - c_s) \tag{12}$$

By applying the Antoine equation, the membrane flux becomes a function of $T_{int,evap}$ which is not determined at this point. However, both the evaporation interface and the membrane are assumed to have no inertia due to their limited thickness. Thereby, all mass evaporating at the interface must also pass through the membrane to satisfy mass conservation. The evaporation and the membrane mass flux are therefore equal ($\dot{m}_{evap} = \dot{m}_{mem}$). Therefore, Eq. 7 and 9 can be combined to derive an implicit expression for $T_{int,evap}$.

The temperature in the membrane T_{mem} and at the bottom of the membrane $T_{mem,bottom}$ are then derived using the thermal resistances in series approach (they are needed for Eq. 9 and the boundary conditions). The partial air pressure and the total pressure in the membrane are calculated as the arithmetic mean value between the interface and the air-gap.

2.3. Air Gap

The NS equations (Eq. 1 – 3) are solved for the air-vapor mixture in the air-gap. The temperature boundary condition on the membrane side $T_{mem,bottom}$ is calculated between the air-gap temperature T_{air} and the interface temperature $T_{int,evap}$ according to the thermal resistances in series. In contact with the liquid film, the interface saturation temperature $T_{int,cond}$ is applied as boundary condition as calculated in 2.4.

To account for the vapor, a concentration conservation equation is used to calculate the water content (Eq. 13).

$$\int_V \frac{\partial \rho a_v}{\partial t} \, dV + \int_{\mathbf{S}} \rho \mathbf{u} a_v \, d\mathbf{S} = \int_{\mathbf{S}} D_{v,air} \nabla a_v \, d\mathbf{S} + J \tag{13}$$

$D_{v,air}$ refers to the diffusion coefficient of water vapor in air. The vapor mass flux through the membrane $\dot{m}_{mem}$ and the condensation mass flux at the liquid film $\dot{m}_{cond}$ are included in the source term J. The thermodynamic properties of the air vapor mixture are approximated by constant air properties at the mean temperature between hot salt water inlet temperature and coolant inlet temperature. Only the density is a function of temperature to account for buoyancy effects.

2.4. Condensation Interface

The condensation mass flux can be obtained from the energy conservation equation at the interface (Eq. 14).

$$\dot{m}_{cond} \cdot h_d = \lambda_{film} \frac{\left(T_{int,cond} - T_{film} \right)}{d_{film}/2} - \lambda_{air} \frac{(T_{air} - T_{int,cond})}{d_{air}/2} \tag{14}$$

Still, the interface temperature $T_{int,cond}$ is to be determined. For condensation to occur, $T_{int,cond}$ is assumed to be the temperature at which the air in contact with the interface is saturated. Therefore, the vapor pressure in the adjacent air cells is calculated from the vapor content (Eq. 10) and the inverted Antoine equation is used to determine $T_{int,cond}$ (Eq. 11).

2.5. Liquid Film

The film thickness is kept constant throughout the calculation assuming that the condensation rate equals the condensate discharge from the module. A three-dimensional temperature profile is calculated according to Eq. 3. The boundary temperature on the air side is set to the interface temperature $T_{int,cond}$. On the side of the steel plate, the thermal resistance in series approach between T_{film} and T_{cool} leads to the temperature boundary condition.

2.6. Coolant Channel

In the coolant channel, Eq. 1 – 3 are solved. Similar to the hot water channel, the temperature at the inlet is assumed to be constant and uniform. The walls are modeled as adiabatic. Also, an inlet velocity profile is assumed which is parabolic in height and constant throughout the depth of the module.

3. Implementation and Validation

The model is implemented in Python and the finite volume method is used for solving the three-dimensional equations. The first-order backward Euler scheme is applied for temporal discretization, whereas central differencing is used for spatial discretization. Only for the discretization of the advection terms, SUPERBEE scheme is used [22].

For the validation, a rectangular membrane area of $0.16 \cdot 0.1$ m^2 in x and z direction is investigated according to the experiments performed by Banat [20]. In y direction, the height of the hot feed and coolant channel is $1.5 \cdot 10^{-3}$ m, of the air-gap $3.5 \cdot 10^{-3}$ m and of the liquid film $0.5 \cdot 10^{-3}$ m. In the hot feed and coolant channel, the computational domain consists of 92k cells, 215k in the air-gap domain and 31k in the liquid film. Gravity acts in negative x direction.

The mean hot water and coolant inlet velocity is $0.6\frac{m}{s}$ and the coolant inlet temperature is 20°C.

For the membrane, literature values for polyvinylidene fluoride (PVDF) are used for the thermodynamic properties. The membrane thickness is 110 µm, the pore diameter 0.45 µm and the porosity is 75% [20]. The tortuosity is set to 1.5.

This validation study is symmetrical in Z-direction and therefore does not exploit all capabilities of the three-dimensional model here presented. The validation, however, opens the ground for further qualitative studies which include three-dimensional effects.

4. Results

In Fig. 3 the permeate flux measured in the experiments by Banat [20] are compared to the condensation mass flux $\dot{m}_{cond}$ computed by the model. The permeate flux is increasing with increasing hot water inlet temperatures in both data sets and a good agreement can be found.

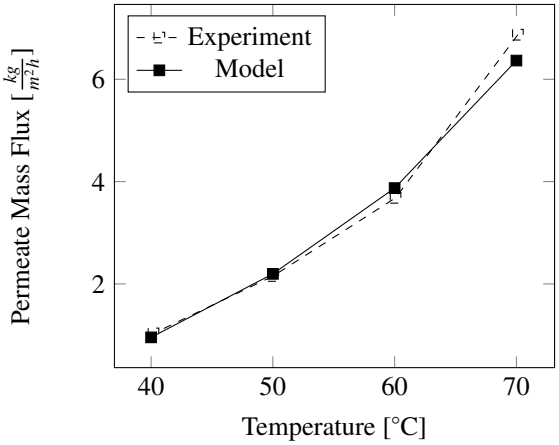

Figure 3: Fresh water output for different hot salt water channel inlet temperatures; from the model the condensation mass flux $\dot{m}_{cond}$ is used, the experiments are performed by Banat [20]

In Fig. 4, the temperature profile is shown perpendicular to the membrane at different locations in the hot feed stream for the 70 °C hot inlet temperature case. Variations are visible along the feed stream direction (x direction). While close to the hot feed water inlet, an uniform temperature distribution can bee seen in the hot salt water, a larger gradient becomes visible further downstream. This behavior can also be seen in the coolant channel in opposite direction and has been previously reported in literature [14]. In the liquid film, however, the variation in temperature is reduced.

The temperature profile in the air-gap follows a concave slope at $x = 0$ m, a straight line in the middle and a convex slope on the hot water outlet side. These deviations from the straight profile are caused by natural convection occurring in the air-gap due to density differences and gravity (see Fig. 5). Natural convection in the air-gap has been reported previously by Chouikh et al. [13].

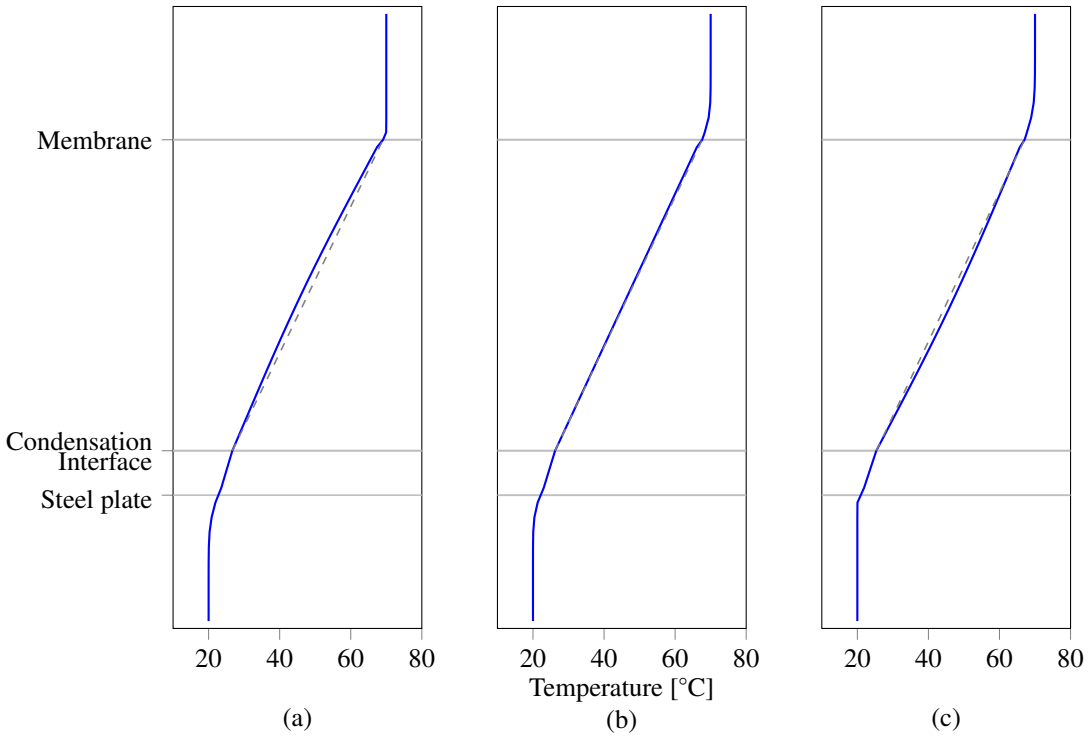

Figure 4: Temperature profile in y direction perpendicular to the membrane for 70°C hot inlet temperature (a) close to the hot water inlet (x = 0 m) (b) in the mid-X location (x = 0.8 m) (c) close to the hot water channel outlet and the coolant inlet (x = 0.16 m); the dashed lines display a straight line between the temperatures at the membrane and at the condensation interface; deviations of the actual temperature profile in blue are due to natural convection

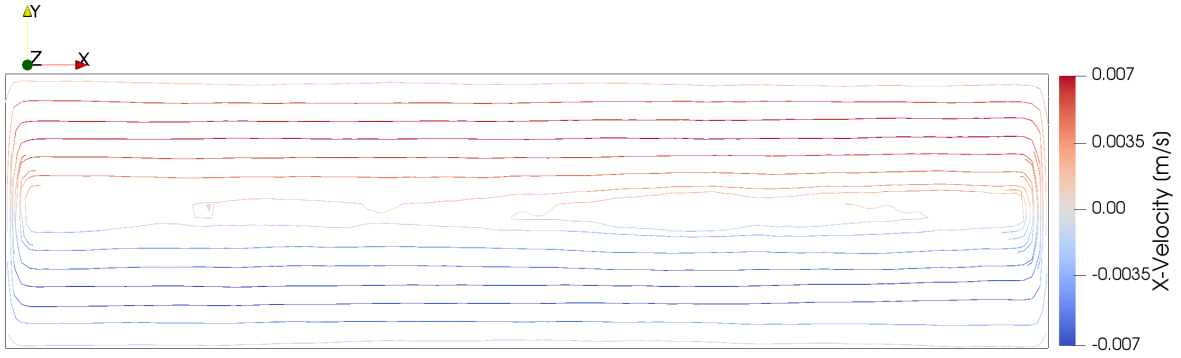

Figure 5: Streamlines in air-gap in mid-Z-plane for 70°C hot inlet temperature; natural convection is visible

This temperature distribution leads to a profile of evaporation $\dot{m}_{mem}$ and condensation fluxes $\dot{m}_{cond}$ in x direction as shown in Fig. 6. The membrane mass flux is increased at the hot feed water inlet due to the higher temperature gradient across the membrane. Additionally, evaporation is favored by the natural convection loop counteracting sensible heat

losses on this side. The opposite is occurring on the side of the hot water outflow, where the swirl reduces the heat available for evaporation, hence the sharp drop in evaporation mass flux.

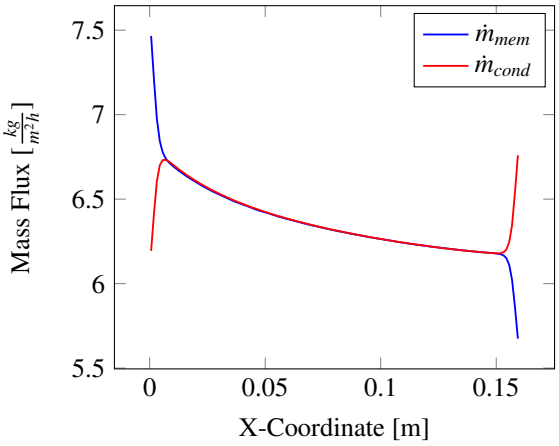

Figure 6: Axial evaporation ($\dot{m}_{mem}$) and condensation mass flux ($\dot{m}_{cond}$) in mid z plane for 70 °C hot inlet temperature

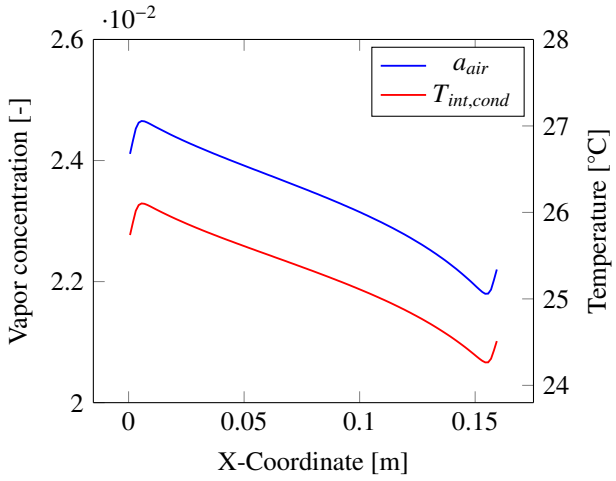

Figure 7: Vapor concentration of air in the air-gap near the liquid film a_{air} and condensation interface temperature $T_{int,cond}$ in mid z plane for 70 °C hot inlet temperature; as $T_{int,cond}$ is calculated from a_{air}, the curves are similar for small variations of $T_{int,cond}$

The profile of the condensation mass flux in Fig. 6 is mainly influenced by the profile of the condensation interface $T_{int,cond}$ which is itself calculated by the vapor concentration a_{air} in the air-gap near the liquid film. $T_{int,cond}$ and a_{air}, therefore, have the same profile for small variations of $T_{int,cond}$ (s. Fig. 7). At the extreme x locations, the influence of the natural convection vortex on the vapor concentration leads to the sharp turns.

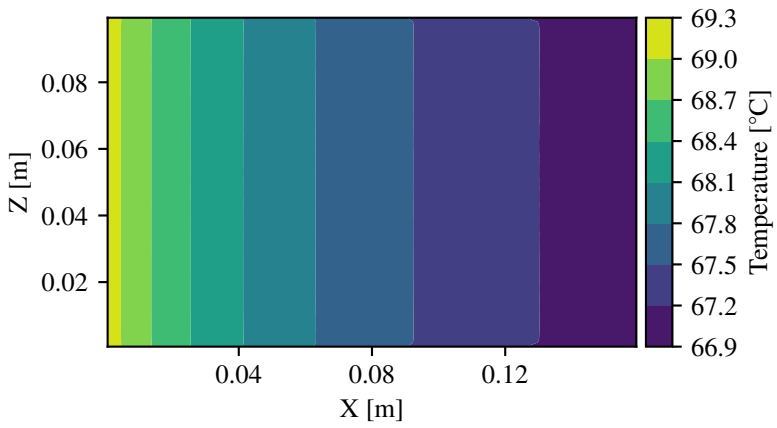

Figure 8: Evaporation interface temperature at the membrane $T_{int,evap}$ for 70 °C hot inlet temperature

In Fig. 8, a contour plot of the evaporation interface temperature is shown as the computation is carried out in three dimensions. As the validation case is symmetrical to the z axis, no variations in this direction are observable.

However, a profile in x direction can be seen. At the hot feed water inlet, the interface temperature is close to the hot inlet temperature, however, it drops significantly further downstream leading to temperature polarization. Thereby, the temperature gradient across the membrane is reduced in comparison to the feed water and air-gap bulk temperature difference (Eq. 15) [2, 9].

$$\psi = \frac{T_{int,evap} - T_{mem,bottom}}{T_{hot} - T_{air}} \tag{15}$$

Temperature polarization values range from 0 to 1 where $\psi = 1$ means that no thermal boundary layer is established. By comparing different axial locations in Fig. 9, it can be seen that temperature polarization enhances in flow direction and therefore depends on the channel geometry as reported previously [14].

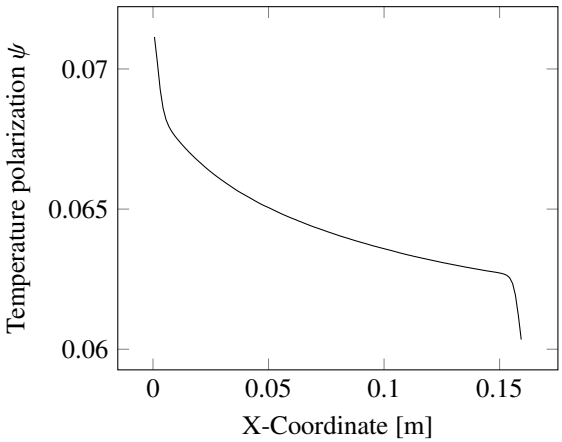

Figure 9: Temperature polarization coefficient in mid z plane for 70 °C hot inlet temperature

A decline in x direction can be seen in many profiles: firstly in the evaporation interface temperature $T_{int,evap}$ and following also the temperature polarization ψ, the membrane flux $\dot{m}_{mem}$, the vapor concentration in the air-gap a_{air}, the condensation interface temperature $T_{int,cond}$ and finally the condensation mass flux $\dot{m}_{cond}$ (Fig. 6 – 9). Therefore, the evaporation interface temperature $T_{int,evap}$ displays the most influential variable and its optimization is crucial for the performance of the MD process.

To highlight the advantage of three-dimensional calculations, the resulting profile of $T_{int,evap}$ (Fig. 11) in case of a double parabolic hot water velocity inlet profile (Fig. 10) is shown. This computation was intended to investigate and optimize the experimental facilities at the University of Luxembourg. The hot feed water inlet temperature is set to 80 °C. Depending on the velocity inlet condition, the evaporation interface temperature clearly varies in z direction leading to a varying utilization of the membrane. Therefore, the model proves useful for the optimization of MD modules.

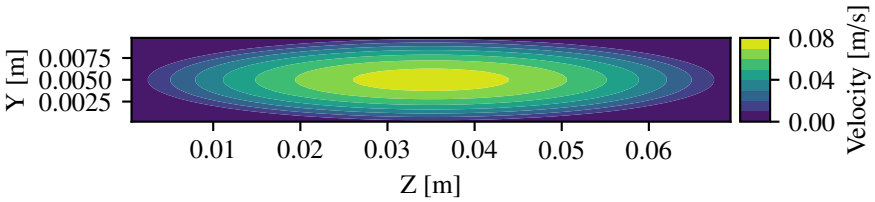

Figure 10: Hot salt water channel inlet velocity profile of a design study for the in-house experimental set-up

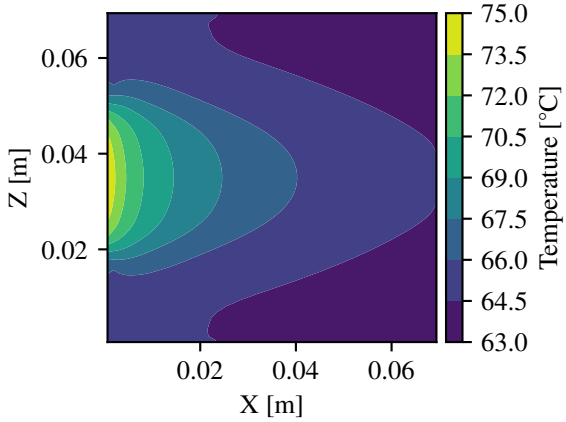

Figure 11: Evaporation interface temperature at the membrane $T_{int,evap}$ of a design study for the in-house experimental set-up; hot feed water inlet temperature is 80 °C

5. Conclusion

A numerical model is introduced which computes AGMD modules in three dimensions covering the feed water channel, air-gap, liquid film and coolant channel. For evaporation and condensation, phase change energy conservation equations are solved. Thereby, the condensation mass flux is computed independently from the membrane mass flux. Simulation results are compared to experimental data and a good agreement is found.

The simulation results show flow profile variations in axial direction and therefore the advantage of multi-dimensional calculations. The validation study investigated an experimental set-up which is symmetrical in one dimension and does not take full advantage of the capabilities of the model. However, different module designs and configurations can be investigated to fully exploit the potential of a three-dimensional model where axial symmetry is no longer required. Additionally, the uncoupling of the distillate mass flux from the membrane flux enables to study gravitational effects and natural convection in the air-gap. A detailed study on module orientation is numerically and experimentally in progress where three-dimensional effects in the air-gap will be investigated. The model therefore complements experiments in developing modules with higher performance.

References

[1] World Health Organization, The global burden of disease, Technical Report, World Health Organization, 2008.

[2] A. Alkhudhiri, N. Darwish, N. Hilal, Membrane distillation: A comprehensive review, Desalination 287 (2012) 2 – 18. Special Issue in honour of Professor Takeshi Matsuura on his 75th Birthday.

[3] A. Alklaibi, N. Lior, Membrane-distillation desalination: Status and potential, Desalination 171 (2005) 111 – 131.

[4] R. B. Saffarini, E. K. Summers, H. A. Arafat, J. H. Lienhard V, Economic evaluation of stand-alone solar powered membrane distillation systems, Desalination 299 (2012) 55 – 62.

[5] M. Khayet, A. Velazquez, J. I. Mengual, Modelling mass transport through a porous partition: Effect of pore size distribution., Journal of Non-Equilibrium Thermodynamics 29 (2004) 279 – 299.

[6] K. W. Lawson, D. R. Lloyd, Membrane distillation, Journal of Membrane Science 124 (1997) 1 – 25.

[7] A. Fane, R. Schofield, C. Fell, The efficient use of energy in membrane distillation, Desalination 64 (1987) 231 – 243.

[8] M. Khayet, Membranes and theoretical modeling of membrane distillation: A review, Advances in Colloid and Interface Science 164 (2011) 56 – 88. Membrane Separation and Colloid Science.

[9] R. Schofield, A. Fane, C. Fell, Heat and mass transfer in membrane distillation, Journal of Membrane Science 33 (1987) 299 – 313.

[10] S. Kimura, S.-I. Nakao, S.-I. Shimatani, Transport phenomena in membrane distillation, Journal of Membrane Science 33 (1987) 285 – 298.

[11] G. L. Liu, C. Zhu, C. S. Cheung, C. W. Leung, Theoretical and experimental studies on air gap membrane distillation, Heat and Mass Transfer 34 (1998) 329–335.

[12] E. K. Summers, H. A. Arafat, J. H. Lienhard, Energy efficiency comparison of single-stage membrane distillation (md) desalination cycles in different configurations, Desalination 290 (2012) 54 – 66.

[13] R. Chouikh, S. Bouguecha, M. Dhahbi, Modelling of a modified air gap distillation membrane for the desalination of seawater, Desalination 181 (2005) 257 – 265.

[14] A. Alklaibi, N. Lior, Transport analysis of air-gap membrane distillation, Journal of Membrane Science 255 (2005) 239 – 253.

[15] I. Janajreh, D. Suwwan, R. Hashaikeh, Assessment of direct contact membrane distillation under different configurations, velocities and membrane properties, Applied Energy 185 (2017) 2058 – 2073. Clean, Efficient and Affordable Energy for a Sustainable Future.

[16] R. Schofield, A. Fane, C. Fell, Gas and vapour transport through microporous membranes. i. knudsen-poiseuille transition, Journal of Membrane Science 53 (1990) 159 – 171.

[17] I. Janajreh, K. E. Kadi, R. Hashaikeh, R. Ahmed, Numerical investigation of air gap membrane distillation (agmd): Seeking optimal performance, Desalination 424 (2017) 122 – 130.

[18] M. M. A. Shirazi, A. Kargari, A. F. Ismail, T. Matsuura, Computational Fluid Dynamic (CFD) opportunities applied to the membrane distillation process: State-of-the-art and perspectives, Desalination 377 (2016) 73–90.

[19] I. Hitsov, T. Maere, K. De Sitter, C. Dotremont, I. Nopens, Modelling approaches in membrane distillation: A critical review, Separation and Purification Technology 142 (2015) 48–64.

[20] F. A. Banat, Membrane distillation for desalination and removal of volatile organic compounds from water, Ph.D. thesis, McGill University, Montreal, Canada, 1994. OCLC: 46510663.

[21] O. C. Bridgeman, E. W. Aldrich, Vapor pressure tables for water, Journal of Heat Transfer 86 (1964) 279–286.

[22] P. L. Roe, Characteristic-Based Schemes for the Euler Equations, Annual Review of Fluid Mechanics 18 (1986) 337–365.

Paper B

Three-dimensional membrane imaging with X-ray ptychography: determination of membrane transport properties for membrane distillation

Kerstin Cramer[a], Nikolaos I. Prasianakis[b], Bojan Niceno[b], Johannes Ihli[c], Mirko Holler[c], Stephan Leyer[a]

[a] *University of Luxembourg, 1359 Luxembourg, Luxembourg*
[b] *Paul-Scherrer-Institute (PSI), Nuclear Energy and Safety Division, 5232 Villigen, Switzerland*
[c] *Paul-Scherrer-Institute (PSI), Swiss Light Source, 5232 Villigen, Switzerland*

Abstract

Membrane distillation (MD) is a desalination technique that uses a membrane to thermally separate potable water from sea or brackish water. The mass transport processes through the membrane are commonly described by the Dusty Gas Model. These processes are modeled assuming uniform, ideally cylindrical capillaries and are adjusted for the membrane geometry by including porosity and tortuosity. The tortuosity is usually set to 2 or is used as an adjusting parameter to fit theoretical models to experimentally measured data. In this work, ptychographic X-ray computed tomography is employed to map the three-dimensional (3D) structure of three commercial state-of-the-art PTFE membranes in MD. The porosity, tortuosity and permeability (viscous flow coefficient) of the samples are computed using the Lattice-Boltzmann method. The intrinsic permeability is compared to the Dusty Gas Model and an apparent permeability is proposed which is corrected for Knudsen slip effects at the membrane structure.

Keywords: Microporous and Porous Membranes, Gas and Vapor Permeation, Tortuosity and Porosity, Viscous Flow, Lattice-Boltzmann

Email addresses: kerstin.cramer@uni.lu (Kerstin Cramer), nikolaos.prasianakis@psi.ch (Nikolaos I. Prasianakis), stephan.leyer@uni.lu (Stephan Leyer)

1. Introduction

Membrane distillation (MD) is a desalination technique that uses a membrane to thermally separate potable water from sea or brackish water. It is considered a promising technology as it operates at lower temperatures ($< 100\,^{\circ}\mathrm{C}$) than conventional thermal desalination processes and can be driven by solar or waste heat [1]. Compared to reverse osmosis, the hydrostatic pressure difference across the membrane is reduced in MD and additionally, the process is more resistant to fouling. However, its energy efficiency and economical performance need to be enhanced for large scale application [2].

State-of-the-art membranes used in MD are made of polymers like polytetrafluoroethylene (PTFE) or polyvinylidene fluoride (PVDF) which were originally developed for microfiltration processes [3]. The mass transport processes in MD are commonly described by the Dusty Gas Model (DGM) which takes into account Knudsen diffusion, molecular diffusion, viscous flow and surface diffusion of which the last one is usually neglected [4]. The most general form of the DGM as it is used in MD is stated by Lawson and Lloyd [5]:

$$\frac{N_i^D}{D_{ie}^K} + \sum_{j=1\neq i}^{n} \frac{p_j N_i^D - p_i N_j^D}{D_{ije}^m} = -\frac{1}{RT}\nabla p_i \tag{1}$$

$$N_i^V = -\frac{p_i B_0}{RT\mu}\nabla P \tag{2}$$

$$N_i = N_i^V + N_i^D \tag{3}$$

$$D_{ije}^m = K_1 P D_{ij}, \qquad D_{ie}^K = K_0\sqrt{\frac{8RT}{\pi M_i}} \tag{4}$$

where N_i^D is the diffusive molar flux, N_i^V the viscous molar flux, N_i the total flux, P the total pressure, p_i the partial pressure of component i, T the temperature, μ the fluid viscosity and M_i the molar mass.

The three constants B_0, K_0, and K_1 depend on the membrane geometry and tare recommended to be measured experimentally. Assuming uniform cylindrical pores, they can be approximated using the membrane pore radius r, tortuosity τ and porosity ϵ [5]:

$$B_0 = \frac{\epsilon\, r^2}{8\,\tau}, \qquad K_0 = \frac{2\,\epsilon\, r}{3\,\tau}, \qquad K_1 = \frac{\epsilon}{\tau} \tag{5}$$

Many MD models apply this simplifications for uniform cylindrical pores [1, 3, 6].

The tortuosity is a measure for the deviation from cylindrical pores and relates the length of the actual path through the membrane to the membrane thickness. This parameter is usually set to 2 or is used as an adjusting parameter to fit theoretical models to experimentally measured data (or vice versa) [3, 6–9]. The values of the constants B_0 and K_0 can be measured by gas permeation experiments [5, 9–12].

A step towards more realistic membrane representation has been done by performing Monte Carlo simulations with a three-dimensional network of interconnected cylindrical pores as the porous membrane [9, 13, 14]. In these studies, the pore size distribution is set according to a statistical distribution function. The thermodynamic conditions inside the membrane and the vapor flux have been calculated taking into account viscous flow and Knudsen diffusion.

For other applications of porous media, permeability and diffusivity values were obtained combining three-dimensional (3D) structural mapping with Lattice-Boltzmann (LB) computation. In a study by Chen et al. [15] the porous structure of shales for shale gas extraction is reconstructed using the markov chain monte carlo method based on scanning electron microscopy images. Membrane properties are then computed via Lattice-Boltzmann simulation. Recently, X-ray tomographic microscopy has been used to analyze gas diffusion layers in polymer electrolyte fuel cells, both for the characterization of the transport properties of materials [16, 17], as well as for investigations relevant to water evaporation under operating conditions [18].

In this work, ptychographic X-ray computed tomography [19] is employed to map the 3D structure of three commercial state-of-the-art PTFE membranes in MD. The tortuosity and viscous flow coefficient of the samples are computed using the Lattice-Boltzmann model by Prasianakis et al. [17, 20] and the obtained membrane properties are compared to the viscous flow coefficient from the DGM.

2. Experiments

Sample Preparation

Three relevant state-of-the-art membranes are identified preceding the experiments (Tab. 1). From each of the membranes, cylindrical volumes are prepared that include the full thickness of the membrane as the height (samples 1-3). The diameter of the surface area is chosen to achieve a significant aspect ratio for the numerical simulation while reducing the overall measuring volume to decrease computational and experimental resources. Of the first membrane, a second sample (sample 4) was prepared whose height is only 20 µm. Instead, it covers a larger surface area.

Sample	**Membrane**	**Manufacturer**	**Pore size [µm]**	**Height [µm]**	**Diameter [µm]**
1	FGLP14250	Merck Millipore	0.2	65	35
2	Gore[a]	Gore	0.22	81	27
3	FHLP14250	Merck Millipore	0.45	65	35
4	FGLP14250	Merck Millipore	0.2	20	53.7

Table 1: Structural specifications of the imaged membrane samples: Pore size according to manufacturer; height and diameter describe the dimensions of the prepared cylindrical samples such that the height is measured from the PP grid in direction of the membrane thickness.
[a]Manufacturer specifications: pore size 0.22 µm, porosity 80 %, thickness 81 µm

The membranes consist of PTFE which is stretched and attached onto a coarser polypropylene (PP) grid. The PTFE itself is not rigid and for the manufacturing of cylindrical samples, embedding with epoxy resin is necessary. It is done in an iterative process using vacuum to assure the complete filling of all membrane pores. The preparation of the samples is done using focused-ion-beam cutting.

Ptychographic X-ray Computed Tomography

The 3D structures of the samples are obtained using ptychographic X-ray computed tomography. Experiments were conducted at the cSAXS beamline of the Swiss Light Source, PSI, Switzerland. Ptychographic X-ray computed tomography is a "scanning" coherent diffraction imaging technique that provides quantitative 3D density maps [19]. For the tomographic reconstructions, iterative phase retrieval algorithms were applied and tomograms of

phase and amplitude contrast are obtained by combining multiple projection angles [21, 22]. Advantages of this technique lie in the high spatial-resolution and the obtained quantitative tomograms [19].

For the experiments described in this paper, a photon energy of 6.2 keV is used. Ptychographic scans consisted at minimum of 415 diffraction pattern with an exposure time of 0.1 seconds per projection. Sampling positions were set using a Fermat spiral scanning grid with an average step size of 2.5 microns. The beam size at the sample plane was 4 microns in diameter.

The experimental set-up described by Holler et al. [23, 24] is extended by a liquid nitrogen cooled and depressurized specimen environment. Thereby, the samples remain in vacuum and at $-180\,^{\circ}\mathrm{C}$ during the entire measurement. Tomographic reconstruction was performed as described by Guizar-Sicairos et al. [25]. The resulting voxel size is 38.99 nm, the number of projections and the spatial-resolution of the individual tomograms as determined by Fourier shell correlation can be found in Table 2.

Larger sample diameters, due to the increased beam exposure, i.e. increased number of required projections to reach a set spatial-resolution, enhance the extent and likelihood of beam damage. This favors as such a loss in the achievable spatial-resolution which can be seen by comparing sample 1 and sample 4 in Tab. 2 for an example. As such it was favorable to keep the sample diameter as small as possible while increasing the sample height to image a sample representative volume.

Segmentation

The electron-density difference between PTFE and epoxy is sufficient to provide decent contrast in the electron density tomograms (Fig. 1). The PTFE structure is obtained from the tomograms by pixel intensity thresholding and a square cuboid is extracted for the computational domain (Fig. 2). Then, the porosity of the membrane samples can be calculated by relating the sum of all void pixels to the total number of pixels.

Sample	**#Projections**	**Resolution [nm]**	**Domain dimensions [µm³ (voxels)]**
1	740	81.73	$59.85 \cdot 22.42 \cdot 22.42$ $(1535 \cdot 575 \cdot 575)$
2	600	128.47	$57.70 \cdot 15.60 \cdot 15.60$ $(1480 \cdot 400 \cdot 400)$
3	740	96.24	$62.42 \cdot 21.44 \cdot 21.44$ $(1601 \cdot 550 \cdot 550)$
4	1000	98.74	$25.34 \cdot 37.04 \cdot 37.04$ $(650 \cdot 950 \cdot 950)$

Table 2: Imaging specifications of the membrane samples: Estimation of the resolution according to Fourier shell correlation [25, 26]; domain dimensions ($x \cdot y \cdot z$) for the subsequent numerical analysis first in µm and below in voxels, x normal to membrane plane

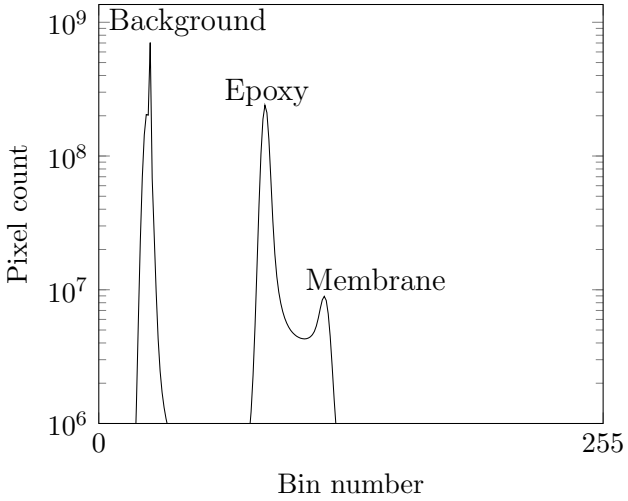

Figure 1: Histogram of sample 3, each bin contains 256 pixel intensity values

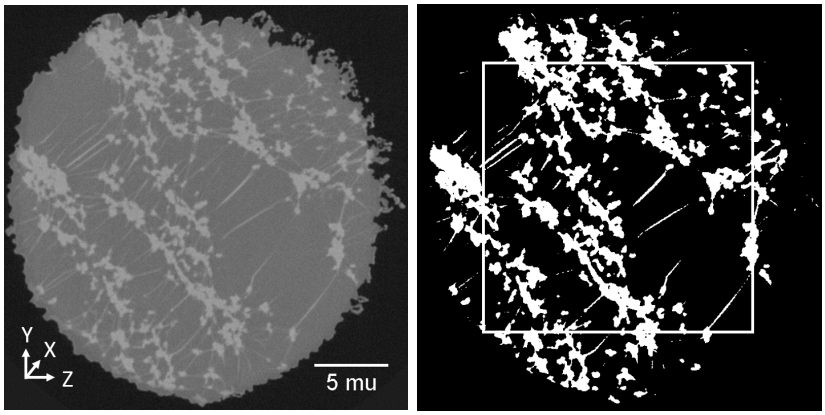

(a) (b)

Figure 2: (a) A *yz* orthoslice from sample 2; the membrane material is visible in light gray and the epoxy, i.e. pore space, in dark gray (b) The same slice after thresholding; as computational domain a rectangular area within the membrane material is selected throughout all slices

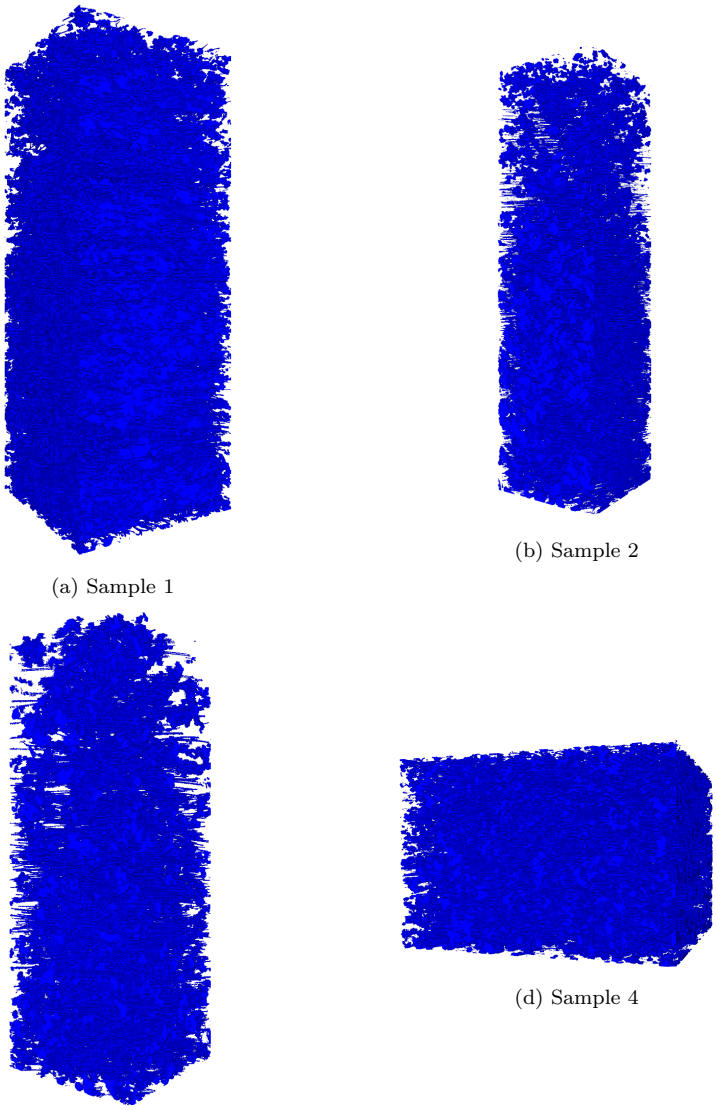

(a) Sample 1

(b) Sample 2

(c) Sample 3

(d) Sample 4

Figure 3: Representation of the segmented tomograms and domains for the computation of the membrane transport properties

3. Numerical Model

The lattice Boltzmann method is used to estimate the permeability of the structures. This method is a mesoscopic computational fluid dynam-

ics method stemming from the Boltzmann equation [27]. The velocity field in the membrane samples is computed using the LB-BGK guided equilibrium model, described in detail by Prasianakis et al. [17, 20]. LB solves the Boltzmann equation for groups of molecules on a Cartesian grid (lattice). A D3Q27 lattice is applied here, meaning a 3D lattice where in each lattice point 27 discrete velocities are defined that point to different neighboring points. Thereby, the computation consists of two steps: firstly, the populations move to the next lattice points with the respective velocity. Afterwards, their interaction with the neighboring populations is computed in the collision step. As the computation is only dependent on the next neighbors, its parallelization is straight-forward and it allows for efficient computing of large lattices.

The lattice is determined by the segmented tomograms in a way that each pixel displays a lattice point. Lattice points where membrane material is present are labeled as solid structure for the computation. At the solid-fluid interface, no-slip flow is assumed which is achieved by half-way bounce back boundary conditions given small Reynolds numbers ($Re << 1$) [28]. On the domain boundaries, periodic boundary conditions are applied.

For each velocity and lattice point, a velocity population is defined which can be viewed as the share of molecules which move in the direction of the specific velocity at this lattice point. These velocity populations f_i are calculated by the lattice BGK equation (Eq. 6) where c_i refers to the discrete velocities for $i = \{1, 2..., 27\}$.

$$f_i\left(\vec{x} + \vec{c}_i, t+1\right) - f_i\left(\vec{x}, t\right) = -\frac{1}{\tau}\left(f_i\left(\vec{x}, t\right) - f_i^{eq}\left(\vec{x}, t\right)\right) + F_i \tag{6}$$

For the calculation of the equilibrium populations f_i^{eq} the guided equilibrium model is used as it offers optimal accuracy for small Mach numbers ($Ma << 1$) [29]. The relaxation parameter τ is related to the dynamic viscosity by $\mu = \frac{1}{3}\rho\tau$. A constant forcing term F_i accelerates the initially stagnant fluid in X-direction like a pressure gradient.

The macroscopic density ρ and velocity $\vec{u}$ can then be calculated from the velocity populations as shown below:

$$\rho = \sum_{i=0}^{26} f_i \qquad \rho\vec{u} = \sum_{i=0}^{26} f_i \vec{c}_i \tag{7}$$

The calculation using fine resolution geometries, which are described by

~ 0.5 billion computational cells (see Tab. 2) require a considerable amount of computer memory. For sample 4, 270GB of RAM were needed and the computation was therefore, executed on dedicated big memory nodes on the ULHPC's high performance cluster.

Permeability Calculation

In the continuum regime, Darcy's law can be used to compute the permeability matrix for small Reynolds numbers ($Re << 1$) [16]:

$$\kappa_{ab} = \frac{\mu \cdot u_{b,mean}}{\partial p / \partial a} \tag{8}$$

where κ_{ab} is the intrinsic permeability for pressure gradient $\partial p/\partial a$ in direction a and mean velocity $u_{b,mean}$ in direction b. Eq. 8 is applied for the calculation of the membrane samples permeability in the present work using the results from the LB computation. For membrane applications, κ_{xx} is of interest, representing the permeability for acceleration and resulting velocity in x direction. κ_{xx} represents exactly the parameter B_0 in the viscous flow formulation of the DGM as seen in Eq. 2. In this work, the permeability values obtained for the membrane samples by Eq. 8 are compared to the formulation of B_0 for uniform cylinders with Eq. 4.

The permeability in the Darcy flow regime is called intrinsic permeability because it is independent of the fluid. For gas flows in porous media, however, a higher permeability is found due to slip-velocity effects on the boundary with the solid structure [30]. This apparent permeability depends on the flow regime. The standard lattice Boltzmann implementation with the use of the diffusive boundary condition[31], can succesfully describe microflow effects up to a certain Knudsen number Kn ~ 0.1 [32, 33]. For the present study, it is of interest to evaluate the permeability at Knudsen numbers up to Kn ~ 1, hence the intrinsic permeability is corrected using correlations from the literature. A correction factor depending on the Knudsen number is proposed by Beskok and Karniadakis [34] to correlate intrinsic and apparent permeability $\kappa_{a,ab}$.

$$\frac{\kappa_{a,ab}}{\kappa_{ab}} = (1 + \alpha\ Kn) \left(1 + \frac{4\ Kn}{1 - b\ Kn}\right) \tag{9}$$

where $b = -1$ and $Kn = \frac{\lambda}{L}$ is the Knudsen number relating the mean free path λ to the characteristic problem length L. The mean free path can

be calculated by $\lambda = \frac{k_B T}{\sqrt{2}\pi d^2 p}$ with k_B as the Boltzmann constant, T as the temperature and d as the collision diameter.

The parameter α varies from zero for low Knudsen numbers to an asymptotic value α_0 for large Knudsen numbers (Eq. 10):

$$\alpha = \alpha_0 \frac{2}{\pi} \tan^{-1}\left(\alpha_1 K n^{\beta}\right) \qquad \alpha_0 = \left[\frac{64}{3\pi\left(1 - 4/b\right)}\right] \tag{10}$$

with $\alpha_1 = 4.0$ and $\beta = 0.4$ [34].

Knudsen numbers for MD application lie usually between 0.3 and 0.8. For this range, the apparent permeability of the four membrane samples is computed from the intrinsic permeability according to Eq. 9.

Tortuosity Calculation

Gommes et al. [35] proposed to determine the tortuosity in porous media by identifying two parallel planes and comparing the length of the connecting path L_{eff} with the distance in between the planes L. The length of the connecting path can then be estimated by the length of the streamlines if the velocity field is known [17]. The tortuosity can then be calculated as $\tau = (L_{eff}/L)^2$. Tortuosity values for the four membrane samples are determined here following this methodology.

4. Results

The resulting membrane properties for the four membrane samples are presented in Tab. 3.

Sample	$\boldsymbol{\varepsilon}$ **[%]**	$\boldsymbol{\tau}$	$\boldsymbol{\kappa_{xx}}$ **[m²]**	$\boldsymbol{\kappa_{xy}}$ **[m²]**	$\boldsymbol{\kappa_{xz}}$ **[m²]**
1	76.86	2.34	$1.31 \cdot 10^{-14}$	$7.97 \cdot 10^{-17}$	$3.68 \cdot 10^{-17}$
2	79.00	2.28	$1.42 \cdot 10^{-14}$	$1.05 \cdot 10^{-16}$	$4.01 \cdot 10^{-17}$
3	85.04	2.19	$3.23 \cdot 10^{-14}$	$2.44 \cdot 10^{-16}$	$3.07 \cdot 10^{-16}$
4	84.23	2.16	$2.43 \cdot 10^{-14}$	$1.53 \cdot 10^{-16}$	$7.50 \cdot 10^{-17}$

Table 3: Resulting porosity, tortuosity and intrinsic permeability values; κ_{xy} relates the pressure gradient in x direction to the velocity in y direction

The tortuosity is slightly over-predicted compared to the reference value of 2 which is commonly assumed for MD studies [3]. In Fig. 4 the values obtained in this work are compared to common correlations used to calculate

the tortuosity from the porosity. For the analyzed membrane samples, the use of the reference value of 2 is enforced compared to the correlations which under-predict the tortuosity.

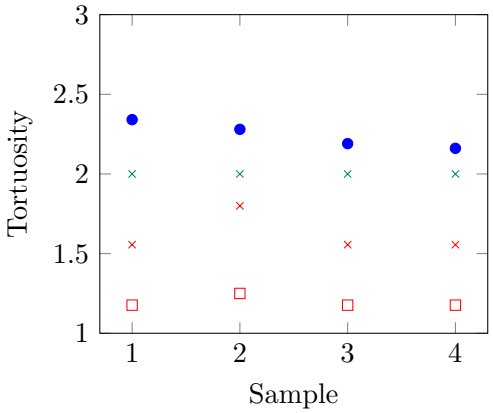

Figure 4: Comparison of tortuosity values obtained here and by different correlations: • τ obtained in this work, × $\tau = \frac{(2-\epsilon)^2}{\epsilon}$ [7], □ $\tau = \frac{1}{\epsilon}$ [7], × τ value commonly used in MD studies [3]; correlations computed with the porosity reported by the manufacturer

The porosity matches the value specified by the manufacturer for sample 2, 3 and 4 (manufacturer values are 85% for sample 1, 3 and 4 and 80% for sample 2). If one takes a closer look at the porosity distribution in axial direction (i.e. the number of void pixels in each yz slice) one finds a heterogeneous distribution (s. Fig. 5). For all samples, a high fluctuation is visible and the porosity close to the PP grid is increased compared to the free surface ($x = 0$). This behavior is more profound for samples 1 and 2 while sample 3 and 4 are more homogeneous. A possible explanation is that the investigated yz plane area does not span a representative area of the membrane. Section 4 provides a more detailed investigation of the representative elementary volume. The reason for the lower porosity at the free surface can also be found in the composition of the membrane. While the PTFE is stretched and attached on the PP grid, it can bend back on the free surface. This tendency to form a conic shape is especially increased since the membrane material is precut in order to fill it with epoxy.

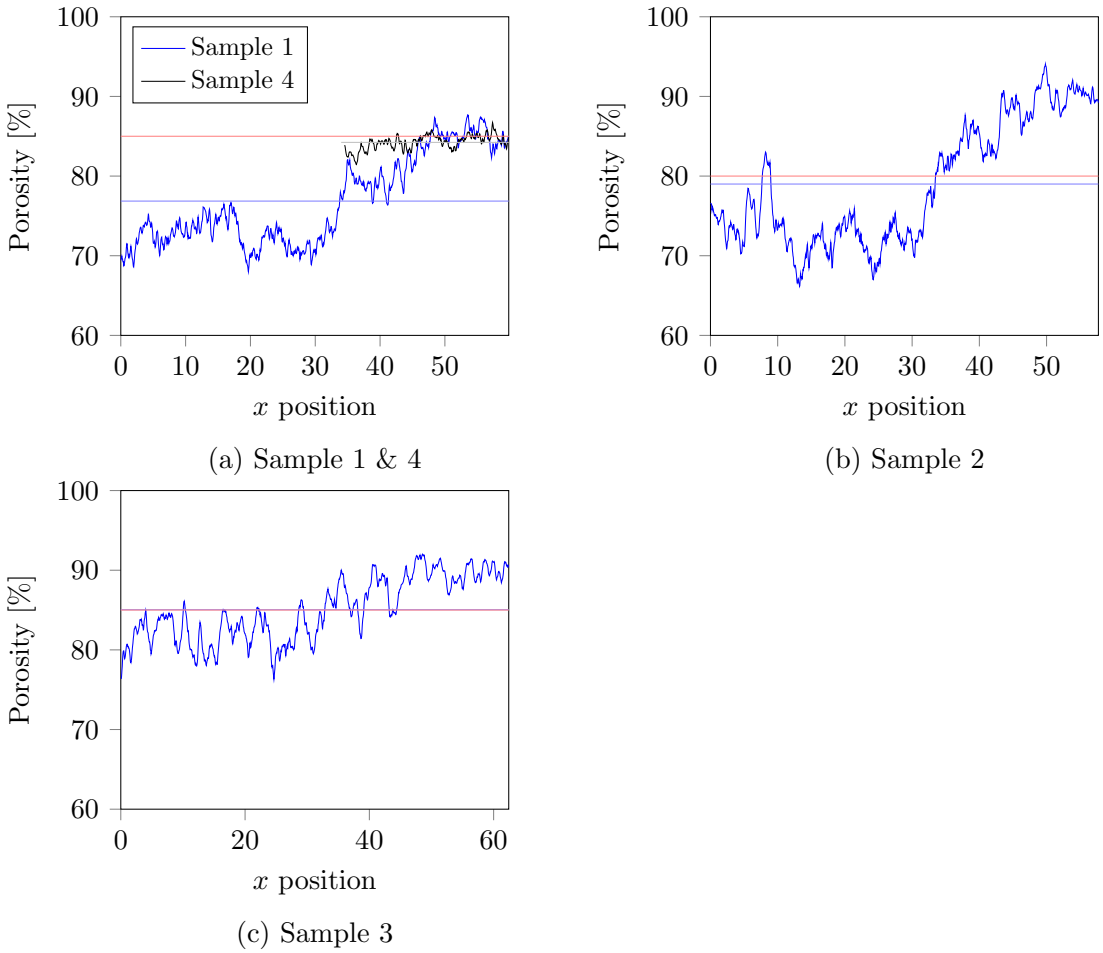

Figure 5: Porosity values calculated for each yz slice plotted against the axial position: Sample, Mean value, Manufacturer value; the x axis starts at the membrane top side and ends at the PP grid; for comparison the porosity specified by the manufacturer is included in red

The values for the intrinsic permeability κ_{xx} lie in the same range as the values reported by Lawson et al. [10] for other MD membranes. Also compared to the DGM, the here determined intrinsic permeability values are for sample 1, 2 and 4 in the same order of magnitude. For sample 3, the intrinsic permeability of the mapped volume is one order of magnitude smaller than predicted by the DGM. The pore size of sample 3 is larger compared to the other samples and therefore, the DGM predicts the permeability higher

because of the quadratical dependency on the pore size of the viscous flow contribution of the DGM. Also the computed intrinsic permeability of sample 3 is the largest of all samples, it is, however, reduced compared to the prediction by the DGM. The LB computation determines the permeability very accurately for the investigated geometry. The discrepancy between DGM and computed data for sample 3 needs therefore to be better understood and a physical explanation investigated. It can also be seen that the permeability of sample 4 is larger than of sample 1 which are both manufactured of the same membrane material but differ in the height and aspect ratio. It gives reason to believe that also the permeability is increased closer to the PP grid as is the porosity.

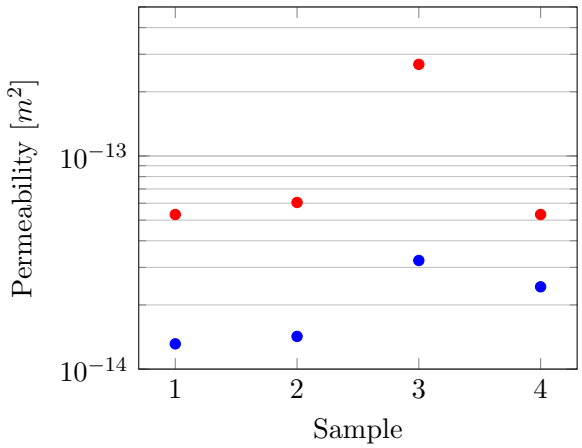

Figure 6: The intrinsic permeability κ_{xx} obtained here is compared to the permeability calculated by the DGM: • Intrinsic permeability κ_{xx}, • DGM

Correcting the intrinsic velocity for velocity slip effects at the solid boundaries, the apparent permeability as a function of Knudsen number is obtained (Eq. 9). The Knudsen number changes with pore size, temperature and pressure variations. In Fig. 7, the apparent permeability is presented for Knudsen numbers from 0.3 to 1 together with the permeability values from the DGM. A close fit for samples 1 and 2 can be seen between computed data and DGM while the permeability computed for sample 4 is increased. Also a better agreement for sample 3 can be found, especially for larger Knudsen numbers. This is surprising as the DGM computes an intrinsic permeability which does not take gas slippage into account.

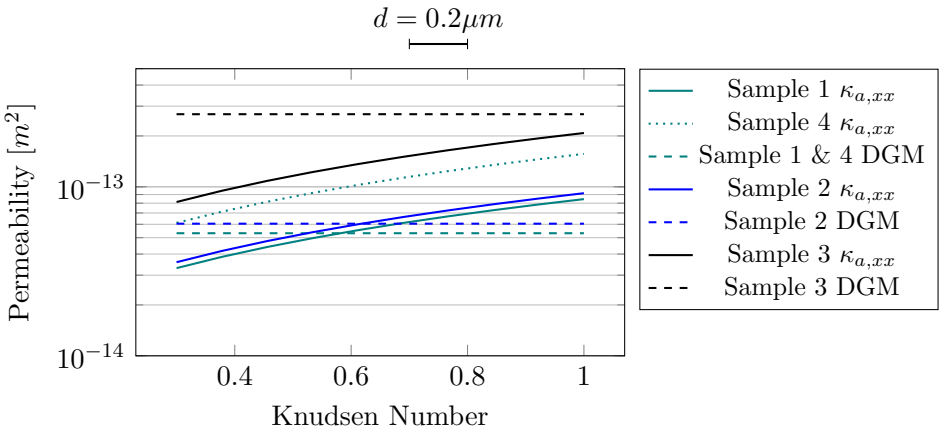

Figure 7: The apparent permeability $\kappa_{a,xx}$ as a function of Knudsen number compared to the DGM for Knudsen numbers from 0.3 to 1; for a porous medium with pore size $d = 0.2\mu m$ the Knudsen number varies between 0.7 – 0.8 for temperature changes between 40 – 80 °C at ambient pressure as indicated by the bar above the graph

Homogeneity of the Samples

To evaluate the representative elementary volume (REV) of the membranes, smaller volume sections are analyzed keeping the original aspect ratio and resolution. For each sample, three subsamples with half the original side lengths are calculated spanning an eighth of the total volume (see Fig. 8). Additionally, six subsamples with a quarter of the original side lengths are calculated representing an 64^{th} of the original volume. The location of these subsamples are chosen randomly within the complete sample volume. In Fig. 9 the resulting porosity and permeability of these subsamples are presented for each sample. The average values for both subsample seizes are indicated together with the results for the full sample. By comparing the green and red circular marks, it can be seen that the full volume is well approximated by the average of at least three subsamples of an eighth volume. The average of the smaller subsamples ($1/64^{\text{th}}$) is only representative for sample 3 and 4.

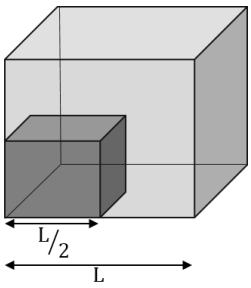

Figure 8: Graphical representation of a subsample with half the original side lengths; from the full volume, subsamples are extracted with constant aspect ratio and randomly chosen location within the full sample

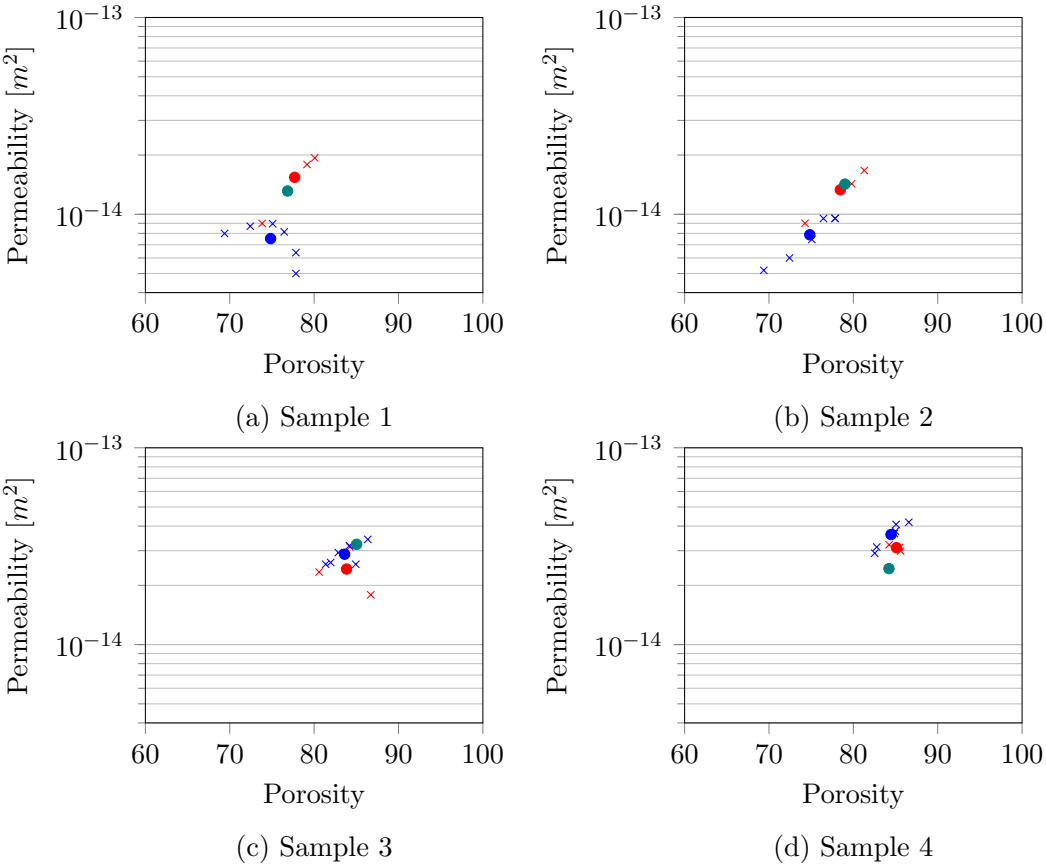

(a) Sample 1

(b) Sample 2

(c) Sample 3

(d) Sample 4

Figure 9: Intrinsic permeability and porosity for different volume sizes: ● Full volume, × 1/8 volume, × 1/64 volume, ● 1/8 volume average value, ● 1/64 volume average value

5. Conclusion

In this work, three state-of-the-art MD membranes are mapped using X-ray ptychography and their 3D structures are obtained. In total, four membrane samples are analyzed. Using these structures, the flow field is calculated driven by a pressure gradient using Lattice-Boltzmann computation. In this way, porosity, tortuosity and permeability values are determined. A comparison between the computed intrinsic permeability and the DGM is presented. Additionally, the apparent permeability as a function of Knudsen number is displayed which includes a correction for velocity slip effects at the solid boundaries.

The porosity agrees well with the porosity specified by the manufacturer for three of the samples. The porosity of one sample is below the specified manufacturer value. Considering the porosity across slices perpendicular to the main flow direction, variations are observed. Closer to the PP grid, the porosity is increased compared to the mean value while it is reduced on the free surface.

The tortuosity lies for all membrane samples slightly above 2 and justifies the use of the reference value of 2 which is commonly assumed for MD studies [3].

The intrinsic permeability is in the same order of magnitude as predicted by the DGM for three samples. For the membrane sample with the larger pore diameter, the DGM predicts the permeability to be one order of magnitude higher which is not reflected in the computations. Similar to the porosity, also the permeability is increased closer to the PP grid compared to the overall membrane height.

Interestingly, for all four samples the apparent permeability is closer to the permeability predicted by the DGM in the range of Knudsen numbers common in MD. This is surprising as the DGM calculates an intrinsic permeability. The discrepancy between DGM and computed permeability needs therefore to be better understood and a physical explanation investigated, especially for the membrane sample with larger pore diameter.

For optimal results, the membrane volumes to be mapped with ptychography should have a low aspect ratio and should not exceed the total volume measured in this work. To achieve significant results multiple samples of each membrane material should be mapped. As it is shown here, three volumes of an eighth volume can be averaged to obtain the same results as analyzing the full volume mapped in this work. This procedure also reduces computational requirements. Additionally, special care must be taken to extract the membrane samples from sufficiently large membrane cuts to reduce possible bending of PTFE on the free surface.

Ultra-high resolution fluid dynamics simulations, using the LB methodology, allows to incorporate phase change phenomena to predict evaporation rates at different flow conditions [18]. Upon the addition of geochemical reactions and deposition of solids, e.g. due to precipitation [36, 37], the list of necessary elements for predicting membrane degradation and fouling, is complete. We shall address these topics in our future research. Together with the three-dimensional air-gap MD model on macroscopic scale [38], the aim is the development of a numerical tool for MD module prototyping for

long term operation.

Acknowledgment

The authors wish to thank J. Reuteler from ScopeM at ETH Zürich, Switzerland for the preparation of the membrane samples and ULHPC for the computational resources.

References

[1] A. Alkhudhiri, N. Darwish, N. Hilal, Membrane distillation: A comprehensive review, Desalination 287 (2012) 2 – 18. Special Issue in honour of Professor Takeshi Matsuura on his 75th Birthday.

[2] R. B. Saffarini, E. K. Summers, H. A. Arafat, J. H. L. V, Economic evaluation of stand-alone solar powered membrane distillation systems, Desalination 299 (2012) 55 – 62.

[3] M. Khayet, Membranes and theoretical modeling of membrane distillation: A review, Advances in Colloid and Interface Science 164 (2011) 56 – 88. Membrane Separation and Colloid Science.

[4] E. Mason, A. Malinauskas, Gas transport in porous media: the dusty-gas model, number Bd. 17 in Chemical engineering monographs, Elsevier, 1983.

[5] K. W. Lawson, D. R. Lloyd, Membrane distillation, Journal of Membrane Science 124 (1997) 1 – 25.

[6] S. Srisurichan, R. Jiraratananon, A. G. Fane, Mass transfer mechanisms and transport resistances in direct contact membrane distillation process, Journal of Membrane Science 277 (2006) 186–194.

[7] S. B. Iversen, V. K. Bhatia, K. Dam-Johansen, G. Jonsson, Characterization of microporous membranes for use in membrane contactors, Journal of Membrane Science 130 (1997) 205–217.

[8] M. Khayet, C. Y. Feng, K. C. Khulbe, T. Matsuura, Preparation and characterization of polyvinylidene fluoride hollow fiber membranes for ultrafiltration, Polymer 43 (2002) 3879–3890.

[9] I. Hitsov, T. Maere, K. De Sitter, C. Dotremont, I. Nopens, Modelling approaches in membrane distillation: A critical review, Separation and Purification Technology 142 (2015) 48–64.

[10] K. W. Lawson, M. S. Hall, D. R. Lloyd, Compaction of microporous membranes used in membrane distillation. I. Effect on gas permeability, Journal of Membrane Science 101 (1995) 99–108.

[11] K. W. Lawson, D. R. Lloyd, Membrane distillation. I. Module design and performance evaluation using vacuum membrane distillation, Journal of Membrane Science 120 (1996) 111–121.

[12] M. Khayet, A. Velazquez, J. I. Mengual, Modelling mass transport through a porous partition: Effect of pore size distribution., Journal of Non-Equilibrium Thermodynamics 29 (2004) 279 – 299.

[13] A. O. Imdakm, T. Matsuura, A Monte Carlo simulation model for membrane distillation processes: direct contact (MD), Journal of Membrane Science 237 (2004) 51–59.

[14] M. Khayet, A. O. Imdakm, T. Matsuura, Monte Carlo simulation and experimental heat and mass transfer in direct contact membrane distillation, International Journal of Heat and Mass Transfer 53 (2010) 1249–1259.

[15] L. Chen, L. Zhang, Q. Kang, H. S. Viswanathan, J. Yao, W. Tao, Nanoscale simulation of shale transport properties using the lattice boltzmann method: permeability and diffusivity, Scientific Reports 5 (2015) 851– 866.

[16] T. Rosen, J. Eller, J. Kang, N. I. Prasianakis, J. Mantzaras, F. N. Büchi, Saturation Dependent Effective Transport Properties of PEFC Gas Diffusion Layers, Journal of the Electrochemical Society 159 (2012) F536–F544.

[17] N. I. Prasianakis, T. Rosen, J. Kang, J. Eller, J. Mantzaras, F. N. Büchi, Simulation of 3d porous media flows with application to polymer electrolyte fuel cells, Communications in Computational Physics 13 (2012) 851– 866.

[18] M. A. Safi, N. I. Prasianakis, J. Mantzaras, A. Lamibrac, F. N. Büchi, Experimental and pore-level numerical investigation of water evaporation in gas diffusion layers of polymer electrolyte fuel cells, International Journal of Heat and Mass Transfer 115 (2017) 238–249.

[19] M. Dierolf, A. Menzel, P. Thibault, P. Schneider, C. M. Kewish, R. Wepf, O. Bunk, F. Pfeiffer, Ptychographic x-ray computed tomography at the nanoscale, Nature 467 (2010) 436– 439.

[20] N. Prasianakis, I. Karlin, J. Mantzaras, K. Boulouchos, Lattice boltzmann method with restored galilean invariance, Physical Review E 79 (2009) 066702.

[21] M. Guizar-Sicairos, J. R. Fienup, Phase retrieval with transverse translation diversity: a nonlinear optimization approach, Optics Express 16 (2008) 7264–7278.

[22] P. Thibault, M. Dierolf, A. Menzel, O. Bunk, C. David, F. Pfeiffer, High-resolution scanning x-ray diffraction microscopy, Science (New York, N.Y.) 321 (2008) 379–382.

[23] M. Holler, A. Diaz, M. Guizar-Sicairos, P. Karvinen, E. Färm, E. Härkönen, M. Ritala, A. Menzel, J. Raabe, O. Bunk, X-ray ptychographic computed tomography at 16 nm isotropic 3d resolution, Scientific Reports 4 (2014) 3857.

[24] M. Holler, J. Raabe, Error motion compensating tracking interferometer for the position measurement of objects with rotational degree of freedom, Optical Engineering 54 (2015) 54 – 54 – 7.

[25] M. Guizar-Sicairos, A. Diaz, M. Holler, M. S. Lucas, A. Menzel, R. A. Wepf, O. Bunk, Phase tomography from x-ray coherent diffractive imaging projections, Optics Express 19 (2011) 21345–21357.

[26] M. Guizar-Sicairos, J. J. Boon, K. Mader, A. Diaz, A. Menzel, O. Bunk, Quantitative interior x-ray nanotomography by a hybrid imaging technique, Optica 2 (2015) 259–266.

[27] S. Succi, The lattice Boltzmann equation: for fluid dynamics and beyond, Oxford university press, 2001.

[28] X. He, Q. Zou, L.-S. Luo, M. Dembo, Analytic solutions of simple flows and analysis of nonslip boundary conditions for the lattice Boltzmann BGK model, Journal of Statistical Physics 87 (1997) 115–136.

[29] N. I. Prasianakis, I. V. Karlin, Lattice Boltzmann method for thermal flow simulation on standard lattices, Physical Review E 76 (2007).

[30] L. J. Klinkenberg, The Permeability Of Porous Media To Liquids And Gases, American Petroleum Institute, 1941.

[31] S. Ansumali, I. V. Karlin, Kinetic boundary conditions in the lattice boltzmann method, Physical Review E 66 (2002) 026311.

[32] S. Ansumali, I. Karlin, S. Arcidiacono, A. Abbas, N. Prasianakis, Hydrodynamics beyond navier-stokes: Exact solution to the lattice boltzmann hierarchy, Physical review letters 98 (2007) 124502.

[33] N. Prasianakis, S. Ansumali, Microflow simulations via the lattice boltzmann method, Communications in Computational Physics 9 (2011) 1128–1136.

[34] A. Beskok, G. E. Karniadakis, REPORT: A MODEL FOR FLOWS IN CHANNELS, PIPES, AND DUCTS AT MICRO AND NANO SCALES, Microscale Thermophysical Engineering 3 (1999) 43–77.

[35] C. J. Gommes, A.-J. Bons, S. Blacher, J. H. Dunsmuir, A. H. Tsou, Practical methods for measuring the tortuosity of porous materials from binary or gray-tone tomographic reconstructions, AIChE Journal 55 (2009) 2000–2012.

[36] N. Prasianakis, E. Curti, G. Kosakowski, J. Poonoosamy, S. Churakov, Deciphering pore-level precipitation mechanisms, Scientific reports 7 (2017) 13765.

[37] S. V. Churakov, N. I. Prasianakis, Review of the current status and challenges for a holistic process-based description of mass transport and mineral reactivity in porous media, American Journal of Science 318 (2018) 921–948.

[38] K. Cramer, B. Niceno, H.-M. Prasser, S. Leyer, A three-dimensional model for the heat and mass transfer in air-gap membrane distillation, Manuscript submitted for publication (2018).

Paper C

Module Orientation for Performance and Energy Efficiency in Air-gap Membrane Distillation

Kerstin Cramer[a], Pol Lamesch[a], Marie-Alix Dalle[a], Bojan Niceno[b], Stephan Leyer[a]

[a] *University of Luxembourg, 1359 Luxembourg, Luxembourg*
[b] *Paul-Scherrer-Institute (PSI), 5232 Villigen, Switzerland*

Abstract

Membrane distillation (MD) is a desalination technique which thermally separates potable water from sea or waste water. Various experiments have been performed where the modules are commonly oriented vertically with the hot salt water flowing upwards or with the hot salt water flowing horizontally above the membrane. However, the impact of the orientation on the MD process is not considered in these studies. In this work, two air-gap MD module configurations are numerically compared and their performance at different feed inlet temperatures, velocities and air-gap thicknesses evaluated. In the upside configuration the hot feed flows above the membrane, while in the downside configuration it flows below the air-gap and membrane. In the latter, the feed solution is not in contact with the membrane but separated by the air-gap which is expected to improve the fouling resistance of the membrane. The three-dimensional CFD computation allows the visualization of the velocity profile in the air-gap due to buoyancy in the downside configuration. As feed, both tap water and sea water are studied and compared. In order to do so, the model is extended to compute salt concentration boundary layers which form due to evaporation of vapor and an increase in salt concentration.

Keywords: Heat and mass transfer, CFD, Fouling and Scaling, Salt Modeling

1. Introduction

Membrane distillation (MD) is a desalination technique which uses a membrane to thermally separate potable water from sea or waste water. Compared to conventional thermal desalination technologies, MD has the advantage of operating at lower temperatures ($< 100°C$) and is considered a promising technology [1]. Furthermore, MD convinces with a higher fouling resistance and insensitivity to feed concentration than other comparable desalination techniques [2]. However, the MD modules economical performance and energy efficiency need to be improved for competitive large scale application [3].

Different configurations are realized with direct contact MD (DCMD) being the most studied configuration [1, 4] and air-gap MD (AGMD) the configuration mostly applied in pilot plants [3]. AGMD has the advantage of reduced conductive losses and a therefore increased thermal efficiency compared to DCMD.

Experiments have been performed mostly studying flat-sheet membrane modules on laboratory scale [1]. The modules are commonly oriented vertically with the hot salt water flowing upwards (Fig. 1a) [5–8]. Similarly often, the hot salt water is flowing horizontally above the membrane (Fig. 1b) [9–12]. This orientation is especially preferred for testing direct solar radiation as heat source. A horizontal orientation with the salt water streaming below the membrane has also been tested (Fig. 1c) [13]. The experiments test the influence of operational parameters on the AGMD process and evaluate the modules performance. However, the impact of the orientation on the MD process is not considered in these studies.

Email addresses: kerstin.cramer@uni.lu (Kerstin Cramer), marie-alix.dalle@uni.lu (Marie-Alix Dalle), stephan.leyer@uni.lu (Stephan Leyer)

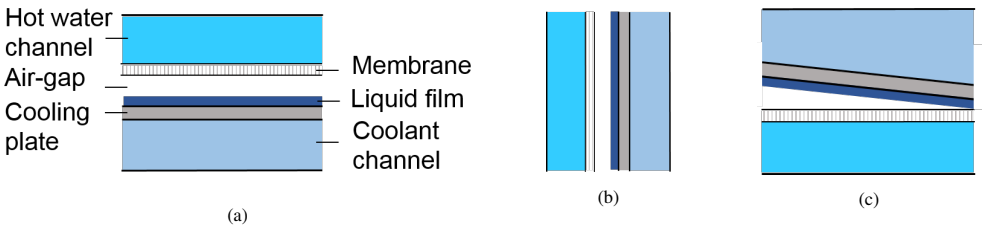

Figure 1: Illustration of the experimentally tested layouts; (a) Hot salt water flowing above the membrane (b) hot feed water flowing vertically (c) hot salt water flowing below the membrane

Recently, Warsinger et al. [14] assessed the impact of the inclination angle on the modules energy efficiency and permeate output. Experimentally and numerically, the module was tilted up to 90° from the vertical position in both directions normal to the membrane. They reported an increase in membrane flux in the experiments for both horizontal configurations which they explain with flooding of the air-gap in one case and permeate falling back from the condensation plate onto the membrane in the other. Numerically, the membrane mass flux is also predicted to increase from vertical to horizontal configuration. The change in orientation is considered in the calculation of the condensate film thickness which is increased when orienting the module horizontally in either direction. The computation is therefore invariant to the direction of the temperature gradient across the module and gravitational effects are not included.

Tan et al. [15] studied the influence of the orientation of DCMD on the permeate flux. They concluded that for desalination the hot water channel below the membrane performed best whereas for the treatment of oily feeds the exact opposite configuration is preferred. The findings are mainly based on their experiments as their simulations are performed isothermally.

Numerical models focusing on the heat and mass transfer in the module neglect gravitational effects whereas those, which solve the full Navier-Stokes equation tend to simplify the thermodynamic processes [16, 17]. Especially for AGMD, not many CFD models exists as the diffusion process of vapor through the air-gap and the condensation process need to be included [18]. However, in a vertically oriented AGMD module, gravitational effects like natural convection are present and can have an impact on the module performance [19].

In this work, the influence of module orientation on the energy efficiency and performance is investigated. Therefore, two horizontal AGMD module designs are analyzed in which the hot feed water flows above the membrane in the first and below the membrane in the other. Different operation conditions and air-gap thicknesses are compared numerically. For the numerical investigation, a model is used which computes buoyancy effects due to temperature depended density but also the heat and mass transfer in great detail [20]. The model is extended to compute salt concentration boundary layer to compare tap water and sea water as feed solutions for both module configurations.

2. Numerical Modeling

The modeled layouts are illustrated in Fig. 2. The upside configuration equals the standard AGMD layout with the hot feed water channel flowing above the membrane (Fig. 2a). As the temperature profile in the coolant channel has a minor impact on the MD process, the coolant channel and the steel plate separating the liquid film are excluded in this study [20]. Instead, a constant temperature is assumed on the boundary of liquid film and steel plate.

In the downside configuration, the hot water channel and the air-gap are located below the membrane and the liquid film above the membrane (Fig. 2b). In this setup, the inverted temperature gradient is opposing gravity creating buoyancy which is expected to influence the heat and mass transfer in the module. Another feature of this setup is the air-gap separating feed stream and membrane. This reduces the contact of the membrane with contaminants and salt in the feed water, possibly reducing scaling and fouling which is a principal challenge in long-term operation [21].

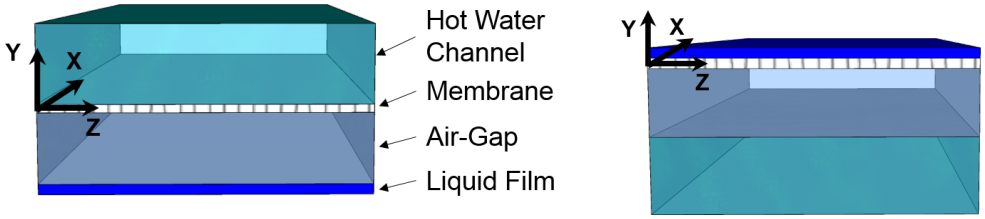

(a) Upside configuration

(b) Downside configuration

Figure 2: Illustration of the computed layouts and the coordinate systems; not to scale

Both layouts are computed with an AGMD model which has been described and validated previously, therefore, only the aspects important for this study and extensions are described in the following [20]. The model solves the temperature and velocity field in three dimensions (3D) in the hot water channel and the air-gap. Buoyancy effects are included by considering temperature depended density and gravity in the incompressible Navier-Stokes equation. The membrane modeling combines the energy conservation during evaporation with the diffusive vapor transport and thermal conduction in the membrane (Knudsen and molecular). Thereby, the temperature profile and mass flux through the membrane is obtained. Also at the liquid film, the condensation mass flux is obtained from energy conservation assuming saturated air. The liquid film is assumed to have a constant thickness and the discharge of the module is assumed to be equal to the condensation mass flux. By solving a conservation equation for the vapor in the air-gap, the effects of natural convection on the vapor mass transfer in the air-gap are also considered. In the downside configuration, no momentum exchange or shear is considered between feed water and air-gap.

Hot Water Channel

In the hot water channel, the Navier-Stokes and energy equation are solved in 3D to obtain the temperature and velocity field. Additionally, a conservation equation for the salt is included to account for the boiling point elevation due to the presence of salt. The salt modeling is described in detail in Section 2.1.

In this study, a parallel velocity inlet profile is assumed. The investigated inlet velocities are 0.025, 0.05 and 0.1 m/s leading to volume fluxes of 1.05, 2.1 and 4.2 l/min. Inlet temperatures of 60, 70 and 80 °C are investigated. The Reynolds numbers are below 2500 in all cases. The channel dimensions are $0.07 \cdot 0.07 \cdot 0.01$ m adapting to ongoing experiments.

Tap water is used as feed, however, a smaller set of operational conditions are additionally computed assuming sea water with 3.5 wt% salt.

Membrane

Merck Millipore FGLP14250 is assumed as the membrane for the computations. Therefore, literature values for Polytetrafluoroethylene are used. The membrane thickness is 65 µm, the porosity 85 %, pore diameter 0.2 µm and the tortuosity is 1.5.

Air-Gap

The velocity field, temperature and vapor concentration are computed in 3D by solving the Navier-Stokes, energy and species conservation equation in the air-gap.

The air-gap thicknesses investigated in this study are $0.5 \cdot 10^{-3}$, $2 \cdot 10^{-3}$ and $8 \cdot 10^{-3}$ m.

Liquid Film

The temperature profile inside the liquid film is determined by solving the energy conservation equation.

The liquid film is in upside configuration $0.5 \cdot 10^{-3}$ m thick, in downside $1 \cdot 10^{-3}$ m. The steel plate temperature is 15 °C.

2.1. Salt concentration modeling

The salt conservation equation tracks the mass content of salt in every computational cell in the hot feed channel. Changes occur by advection and diffusion. In the cell adjacent to the evaporation interface, water evaporates but the salt remains in the feed. In the model, the evaporation of water induces a velocity in y direction which is temporarily ignored for the solution of the concentration equation as no salt advection across the membrane takes place.

At this point, the interface acts as a wall for the salt and no increase in concentration due to evaporation is reflected. To allow for the computation of the concentration boundary layer, a source term is added to the computational cells at the interface boundary. The source term accounts for the difference in salt concentration before and after the evaporation in the respective time step.

$$a_1 = \frac{x_{salt}}{x_{tot}} \tag{1}$$

a_1 represents the salt content before the evaporation with x_{salt} being the mass of salt in the cell and x_{tot} being the total mass of water and salt in the cell. The total mass can be calculated from the density ρ and the volume of the computational cell dV: $x_{tot} = \rho \cdot dV$. x_{salt} can then be determined with the knowledge of a_1 and x_{tot}.

During the evaporation, the mass of salt in the computational cell remains constant while the total mass is reduced by the evaporating vapor.

$$a_2 = \frac{x_{salt}}{x_{tot} - \dot{m}_{evap} \cdot \Delta t} \tag{2}$$

a_2 is the salt content after evaporation, $\dot{m}_{evap}$ the evaporating mass flux, Δt the computational time step.

Finally, the source term q_a for the computational cells at the interface can be expressed as:

$$q_a = \frac{\rho}{\Delta t} (a_2 - a_1) \tag{3}$$

The salt concentration profile leads to variations in density and possibly buoyancy. To account for these effects, the density in the feed channel is calculated as a function of salt concentration and temperature. The equation of state of seawater by Millero and Huang [22] is applied using the coefficients in Table 3 for 0 – 90 °C.

The salt concentration also influences the saturation vapor pressure which is needed to calculate the heat and mass transfer through the membrane. The saturation vapor pressure is temperature dependent and can be calculated by the Antoine equation (Eq. 4). The correction for the presence of salt in the upside configuration can then be done by Raoult's law (Eq. 5).

$$\log_{10} p^0_{sat} = \left(A - \frac{B}{T - C} \right) \tag{4}$$

$$p_{sat} = p^0_{sat} (1 - c_s) \tag{5}$$

p^0_{sat} represents the saturation vapor pressure, p_{sat} the saturation pressure corrected for the presence of salt, T the temperature and c_s the mole fraction of salt.

In the downside configuration, the hot salt water is in direct contact with the air-gap and the evaporating vapor mass flux is calculated from the energy conservation over the interface. Therefore, the interface temperature is to be calculated assuming the air in contact with the interface is saturated. As the vapor concentration is known from solving the vapor concentration in the air-gap, the temperature at the interface can be calculated by inverting the Antoine equation and Raoult's law:

$$p^0_{sat} = p_{sat} / (1 - c_s) \tag{6}$$

$$T = C + \frac{B}{A - \log_{10} p^0_{sat}} \tag{7}$$

Eq. 4, 5 and 7 have been included in a previous version of the model already [20]. The model and the scripts to compute all results in this study are openly accessible[1].

[1] `https://github.com/kjcramer/pyns/tree/configuration_study`

2.2. Performance Indicators

The Recovery Ratio (RR) relates the permeate mass flow $\dot{m}_{permeate}$ which is condensing into the liquid film, to the feed mass flow $\dot{m}_{in}$. The RR is calculated as

$$RR = \frac{\dot{m}_{permeate}}{\dot{m}_{in}} = \frac{\dot{m}_{permeate}}{\rho\, u_{in}\, A_{in}} \tag{8}$$

where u_{in} is the feed inlet velocity and A_{in} the feed inlet area.

The Gained Output Ratio (GOR) is a measure for the energy economization of the module indicating the heat used for evaporation of vapor as a fraction of the total heat inputed into the module $\dot{Q}_{in}$.

$$GOR = \frac{\dot{m}_{permeate} \cdot h_d}{\dot{Q}_{in}} = \frac{\dot{m}_{permeate} \cdot h_d}{\rho\, u_{in}\, A_{in}\, c_p\, (T_{in} - T_{out})} \tag{9}$$

where h_d is the specific heat of evaporation, c_p the heat capacity and $(T_{in} - T_{out})$ the temperature difference in the feed channel between inlet and outflow averaged over the outflow area.

3. Results

Figure 3 shows the permeate flux plotted against the inlet velocity for different air-gap thicknesses and both configurations - upside and downside. The data proofs the strong dependence of the inlet temperature on the permeate flux as well as the weak dependence of the inlet flow velocity. This behavior has been previously experimentally observed [5, 7]. However, it can also be seen that the air-gap thickness has a similarly strong effect as the inlet temperature: a module operated at 80 °C and 2 mm air-gap will produce the same permeate flux as a module operated at only 60 °C and 0.5 mm air-gap.

Only small differences in permeate mass flux are found between upside and downside configuration. For the smallest air gap (0.5 mm), the upside configuration produces a slightly higher permeate flux, while for the medium air-gap (2 mm) the permeate flux of the downside configuration is slightly increased. For the larger air gap of 8 mm, no significant differences can be found. High inlet temperatures and feed velocities favor the upside configuration whereas the downside configuration is less susceptible to feed velocity changes and performs better at the lowest inlet velocity.

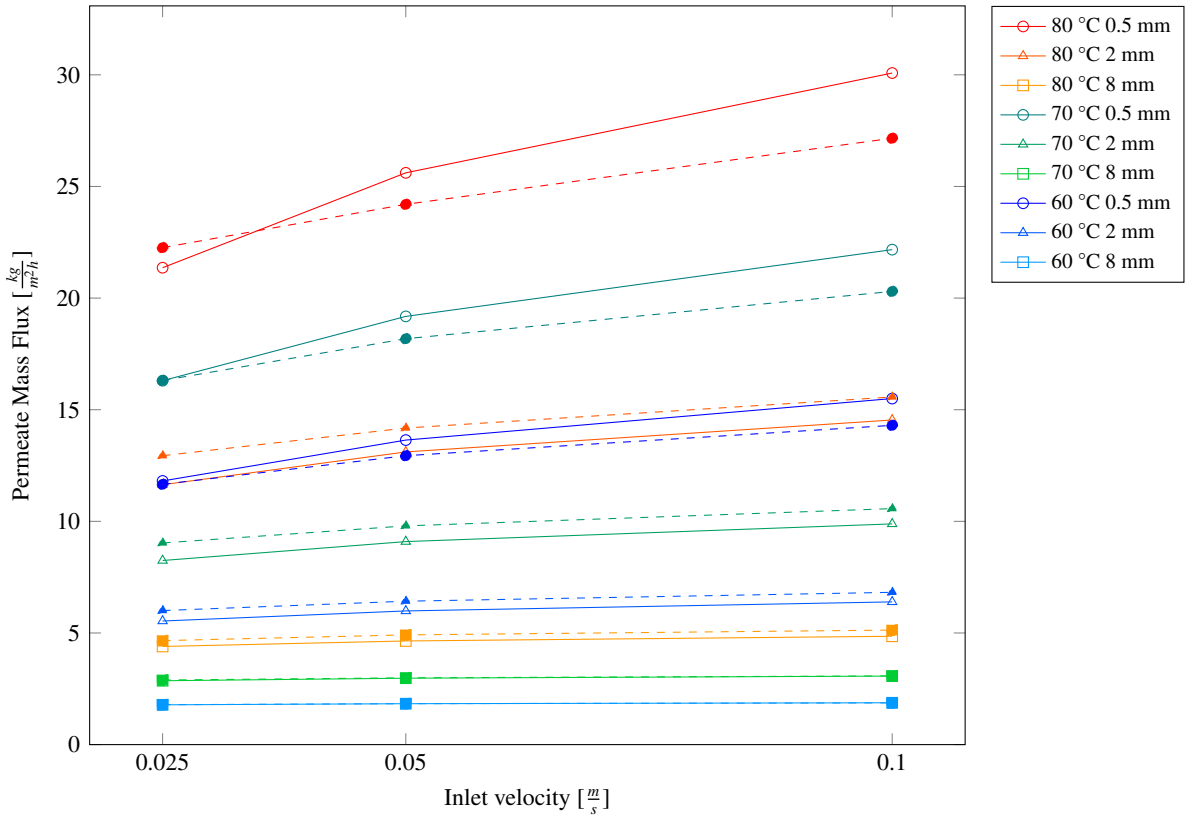

Figure 3: Fresh water output for different hot channel inlet temperatures, velocities and air-gap thicknesses: —○— Upside configuration; - -●- - Downside configuration

The same trends can be seen for the recovery ratio in Fig. 4, as the feed flow rate is independent of configuration, air-gap thickness and feed inlet temperature. Only, the effect of the feed inlet velocity is inverted and the RR is decreasing with increasing feed flow rate.

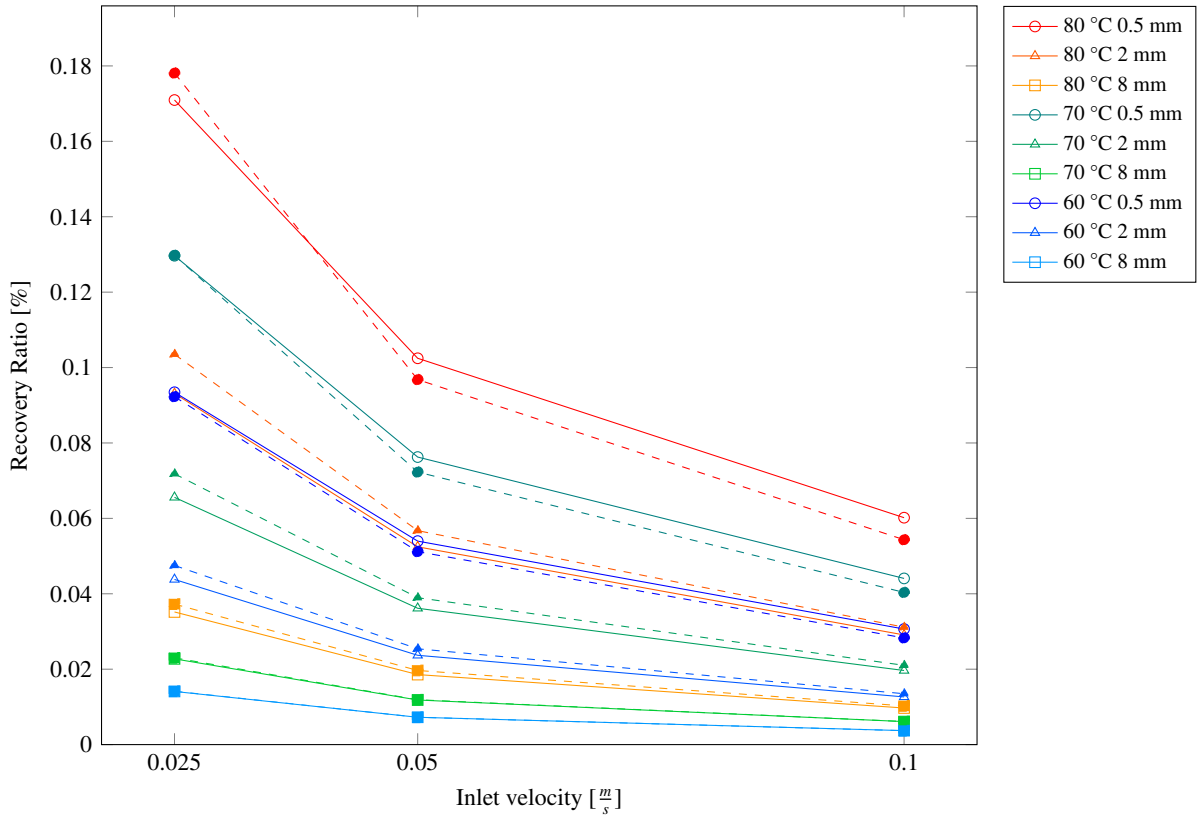

Figure 4: Recovery ratio for different hot channel inlet temperatures, velocities and air-gap thicknesses: —○— Upside configuration; - -●- - Downside configuration

In Fig. 5 the GOR values are presented. For both configurations, GOR is increasing with increasing feed temperature and decreasing feed velocity which agrees with the literature [3]. A higher temperature leads to a higher partial vapor pressure and therefore a higher driving force for the MD process. On the other hand a higher feed flow rate increases the sensible heat transfer through the membrane which outweighs the gain in permeate flux at higher feed velocities and leads to a decreased GOR.

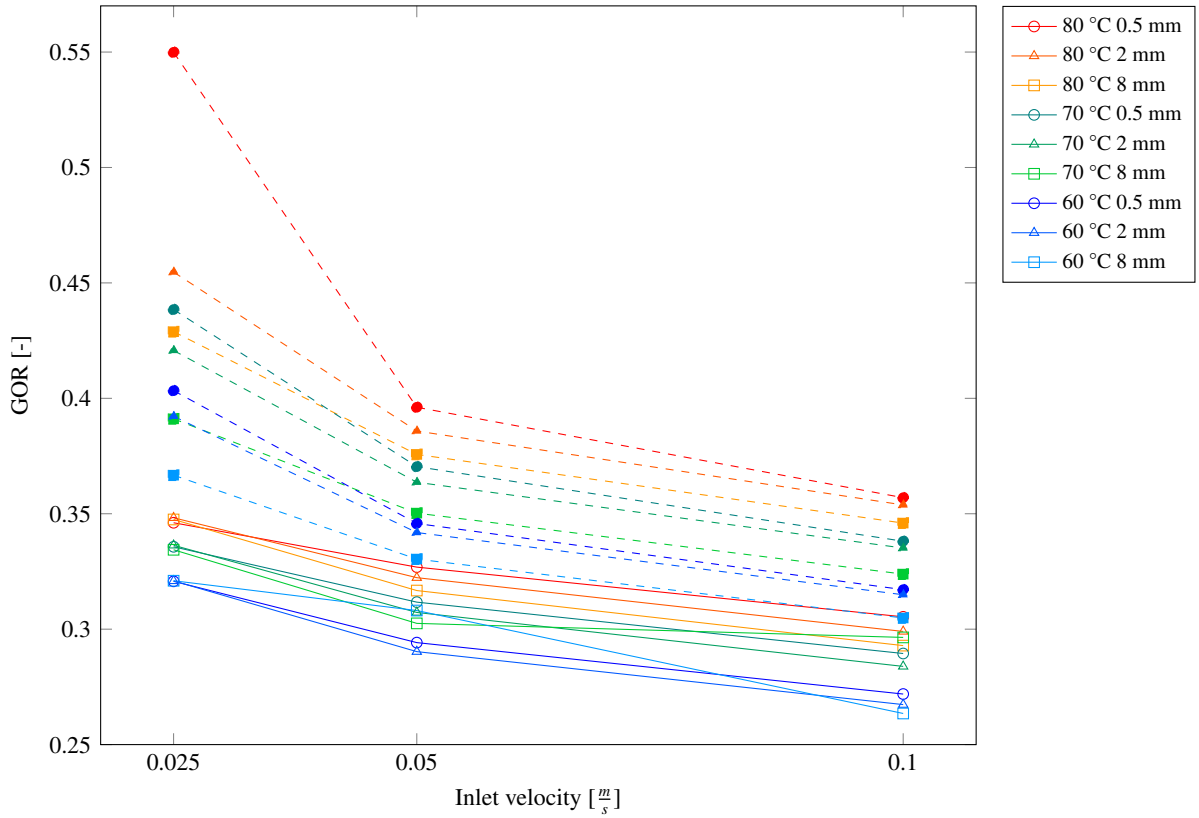

Figure 5: GOR for different hot channel inlet temperatures, velocities and air-gap thicknesses: —○— Upside configuration; - -●- - Downside configuration

For the upside configuration, the influence of the air-gap thickness is less distinct and not consistent. A thicker air-gap reduces the sensible heat losses but also impairs the diffusive vapor transport which results in a smaller permeate flux as already shown in Fig. 3. The predominance is changing in between the two effects for the largest air-gap (hence the crossing lines) but favors a thinner air-gap for the smaller air-gaps.

In the downside configuration, GOR is larger for smaller air-gaps indicating that the mass resistance increases stronger than the insulating benefits when enlarging the air-gap.

The GOR is consistently higher for the downside configuration indicating that less energy is needed to distill the same permeate flux compared to the upside configuration.

Flow field in the air-gap

Fig. 6 – 12 show the velocity fields in the air-gap of the downside configuration for different operational parameters. As the temperature gradient is opposing gravity, buoyancy effects can be seen. For T_{in} = 80 °C and 8 mm air-gap (Fig. 6) vortexes are forming that are rotating alternately clockwise and counter-clockwise, generating thereby an upward or downward movement in between the swirls. The vortexes are uniform in z direction and form along the x axis, the direction of feed flow, for all analyzed inlet velocities.

Even though no stationary vortexes are forming in the smaller air-gaps (Fig. 7 & 8), nonetheless a velocity field is observed with a vertical velocity component. Recalling the evaluation of the GOR in Fig. 5, the smaller air-gaps of the downside configuration performed best at minimizing sensible heat losses while still allowing for vapor mass transfer.

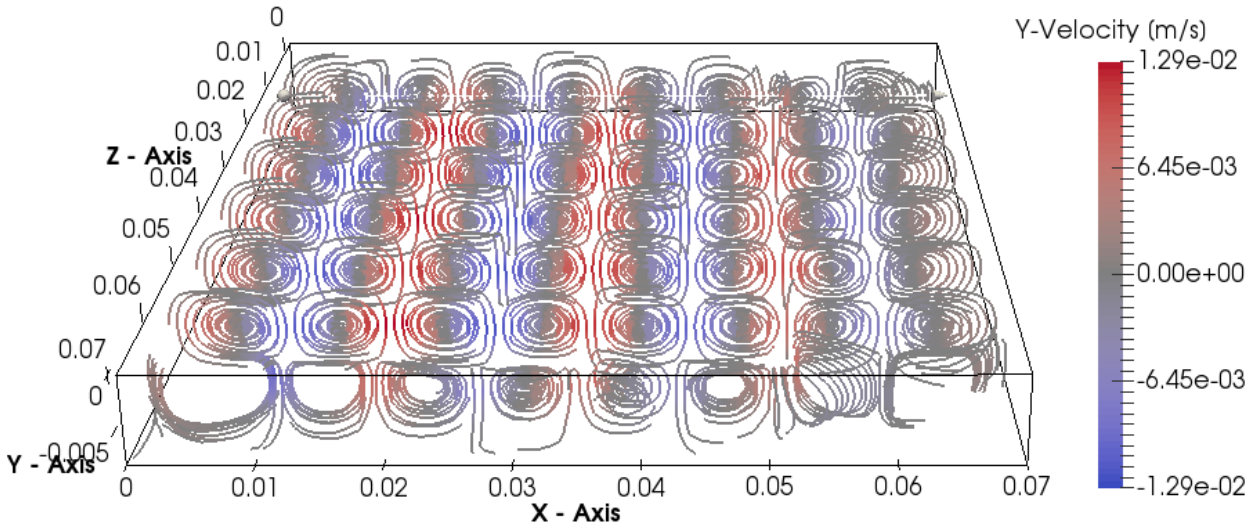

Figure 6: Streamlines in air-gap for downside configuration, $T_{in} = 80\,°C$, $u_{in} = 0.05\,\frac{m}{s}$ and 8 mm air-gap

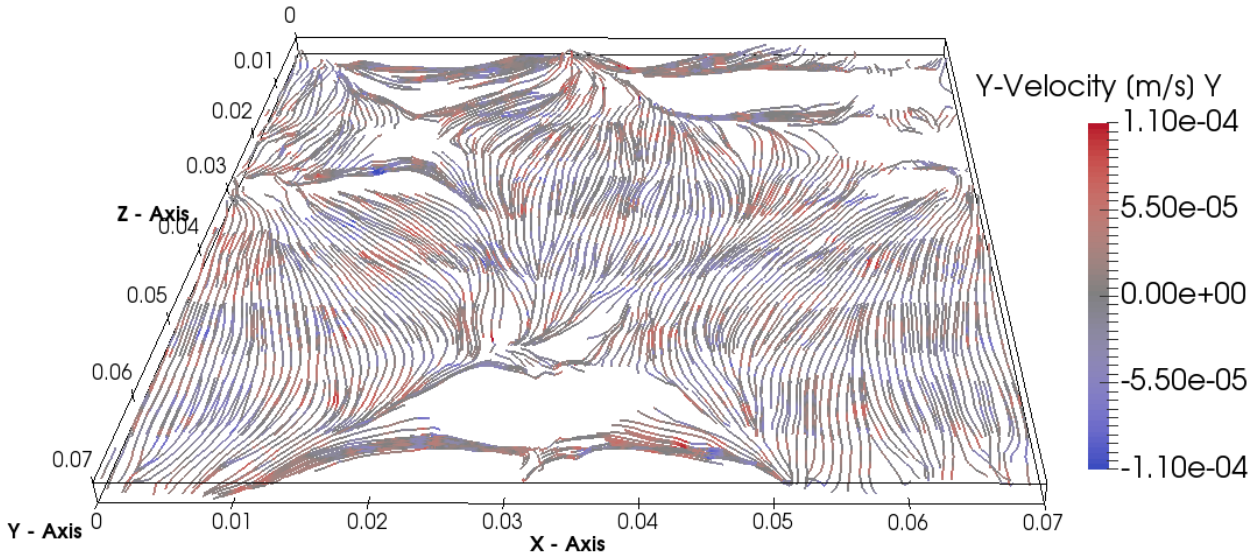

Figure 7: Streamlines in air-gap for downside configuration, $T_{in} = 80\,°C$, $u_{in} = 0.05\,\frac{m}{s}$ and 2 mm air-gap

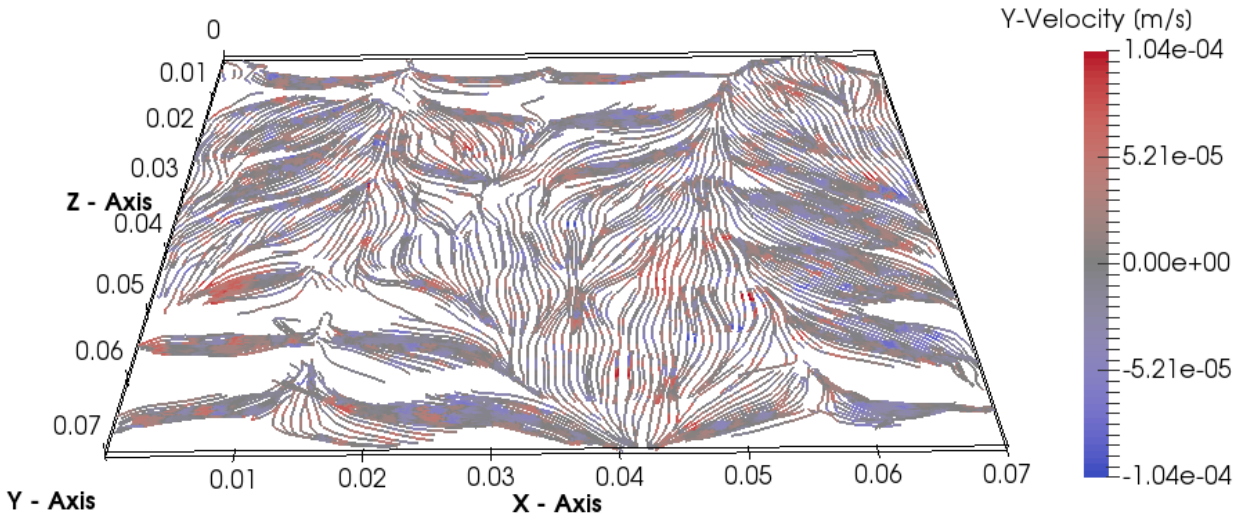

Figure 8: Streamlines in air-gap for downside configuration, T_{in} = 80 °C, u_{in} = 0.05 $\frac{m}{s}$ and 0.5 mm air-gap

Fig. 9 – 11 show the velocity fields for different feed flow rates at T_{in} = 70 °C and 8 mm air-gap. While at u_{in} = 0.025 $\frac{m}{s}$ (Fig. 9) three fully established vortexes are visible, two are less established when increasing the feed velocity to 0.05 $\frac{m}{s}$ (Fig. 10) and barely visible anymore for u_{in} = 0.1 $\frac{m}{s}$ (Fig. 11). The favored formation of vortexes at lower feed velocities explains why the downside configuration is less susceptible to feed velocity changes. The vortexes encourage the mass transfer in the air-gap also at lower feed velocities.

For T_{in} = 60 °C, no stationary swirls are observed, however, a distinctive vertical velocity component is still visible (Fig. 12).

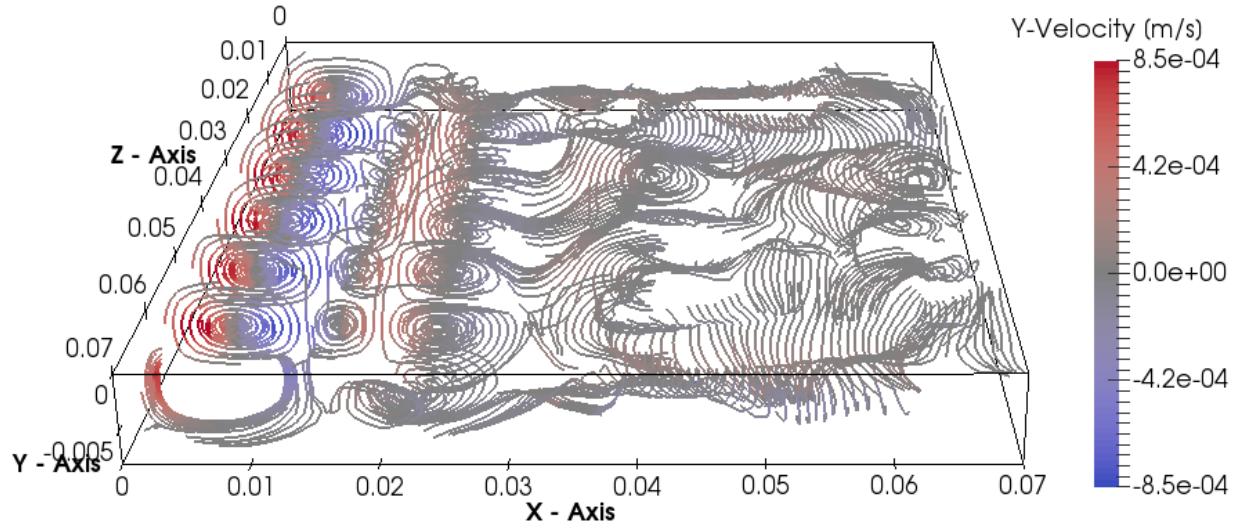

Figure 9: Streamlines in air-gap for downside configuration, T_{in} = 70 °C, u_{in} = 0.025 $\frac{m}{s}$ and 8 mm air-gap

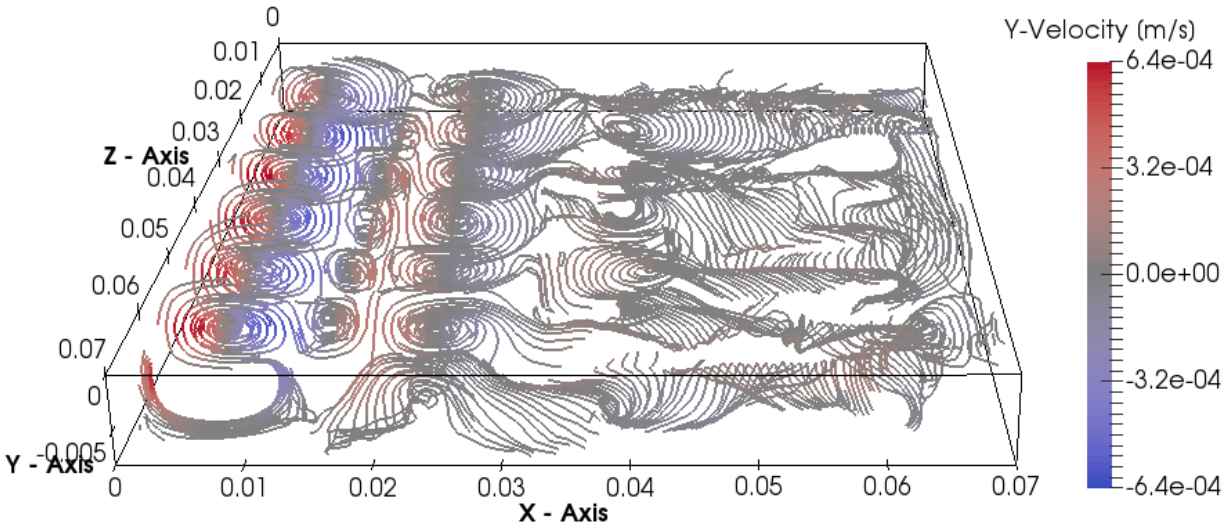

Figure 10: Streamlines in air-gap for downside configuration, $T_{in} = 70\,^{\circ}\text{C}$, $u_{in} = 0.05\ \frac{m}{s}$ and 8 mm air-gap

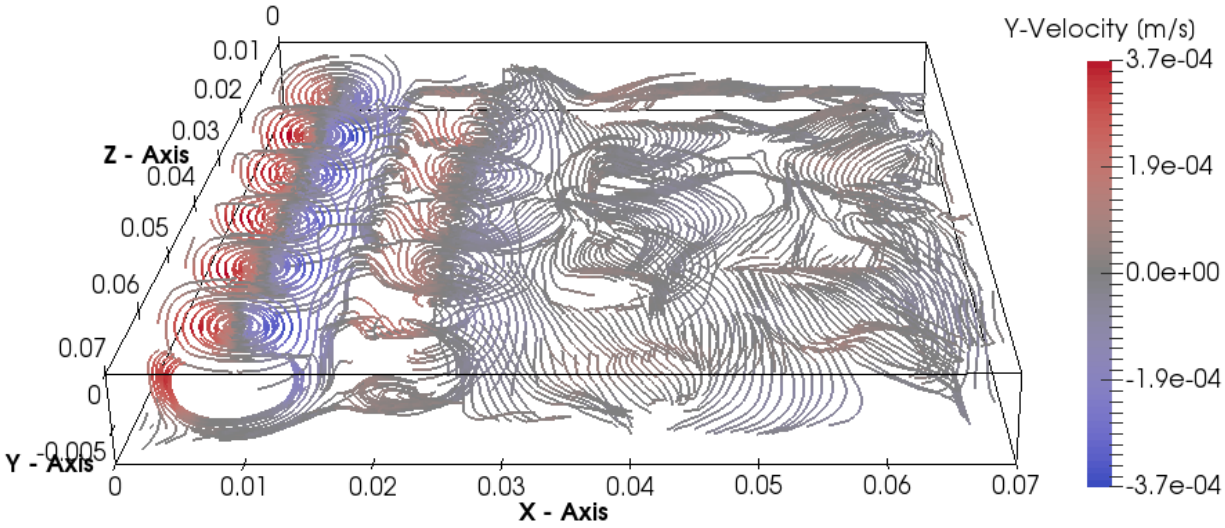

Figure 11: Streamlines in air-gap for downside configuration, $T_{in} = 70\,^{\circ}\text{C}$, $u_{in} = 0.1\ \frac{m}{s}$ and 8 mm air-gap

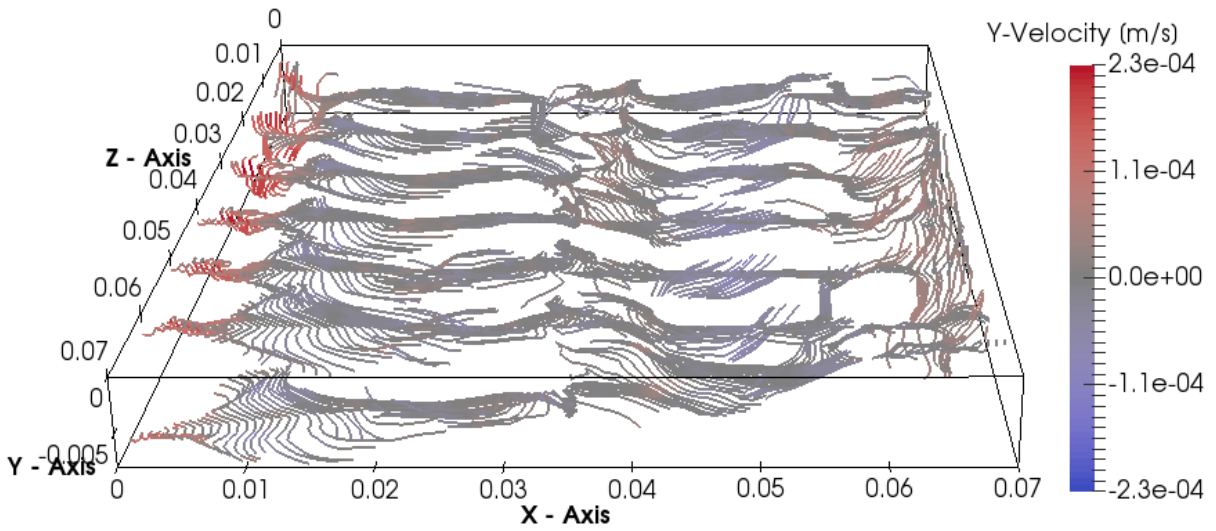

Figure 12: Streamlines in air-gap for downside configuration, $T_{in} = 60\,°C$, $u_{in} = 0.05\,\frac{m}{s}$ and 8 mm air-gap

Comparison of tap water and sea water

Applying sea water as feed, a slight reduction in permeate flux, RR and GOR is observable for all operational conditions and both configurations (Fig. 13 – 14). The reduction is in general increased for the downside configuration. Exceptions are the largest air-gap (8 mm) and the GOR value for the slowest feed velocity which is even higher in presence of the salt.

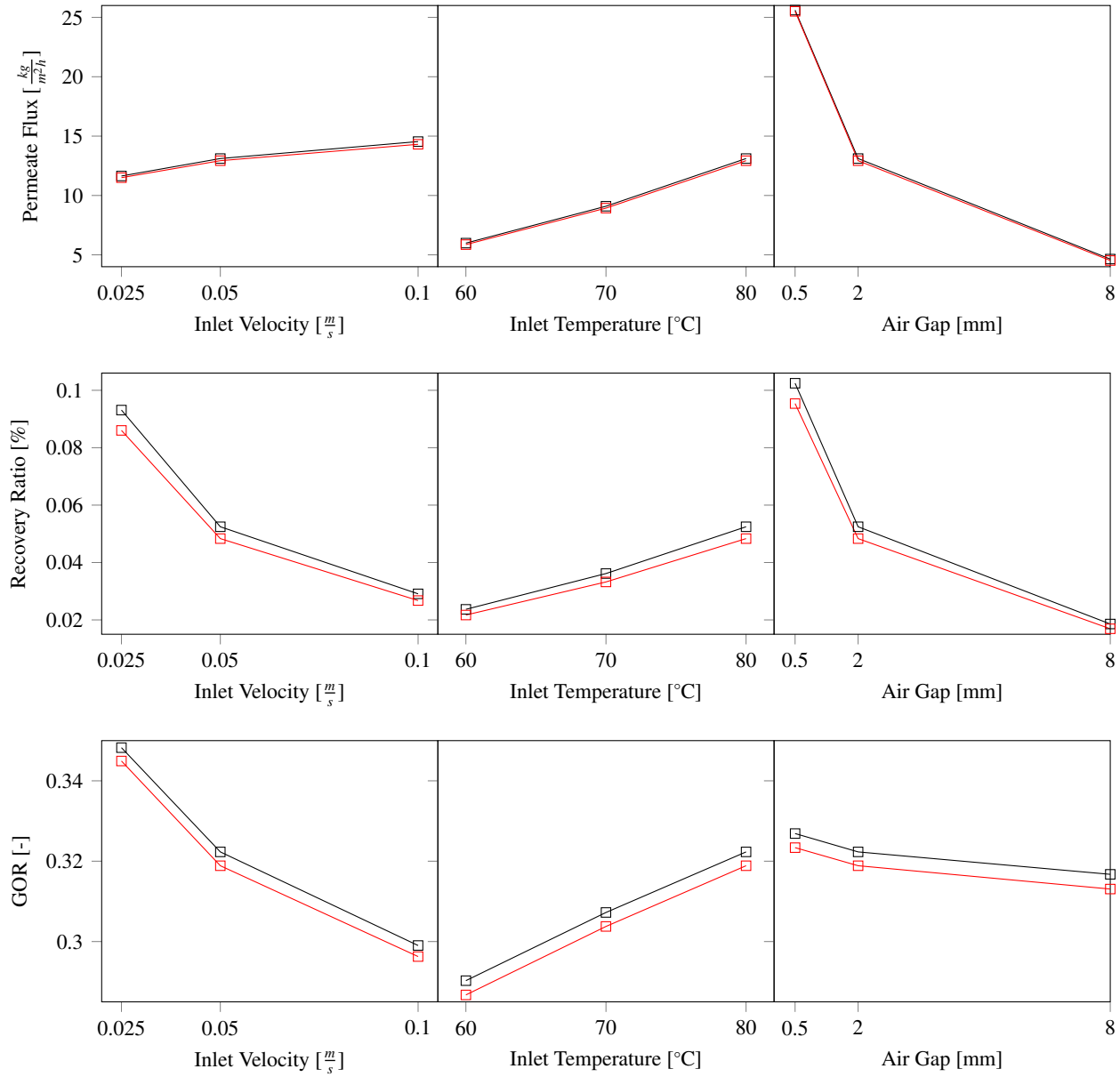

Figure 13: Fresh water output, recovery ratio and GOR for upside configuration: —□— Tap water; —□— Sea water (3.5 wt% salt); default parameter for computation: T_{in} = 80 °C, u_{in} = 0.05 $\frac{m}{s}$ and 2 mm air-gap

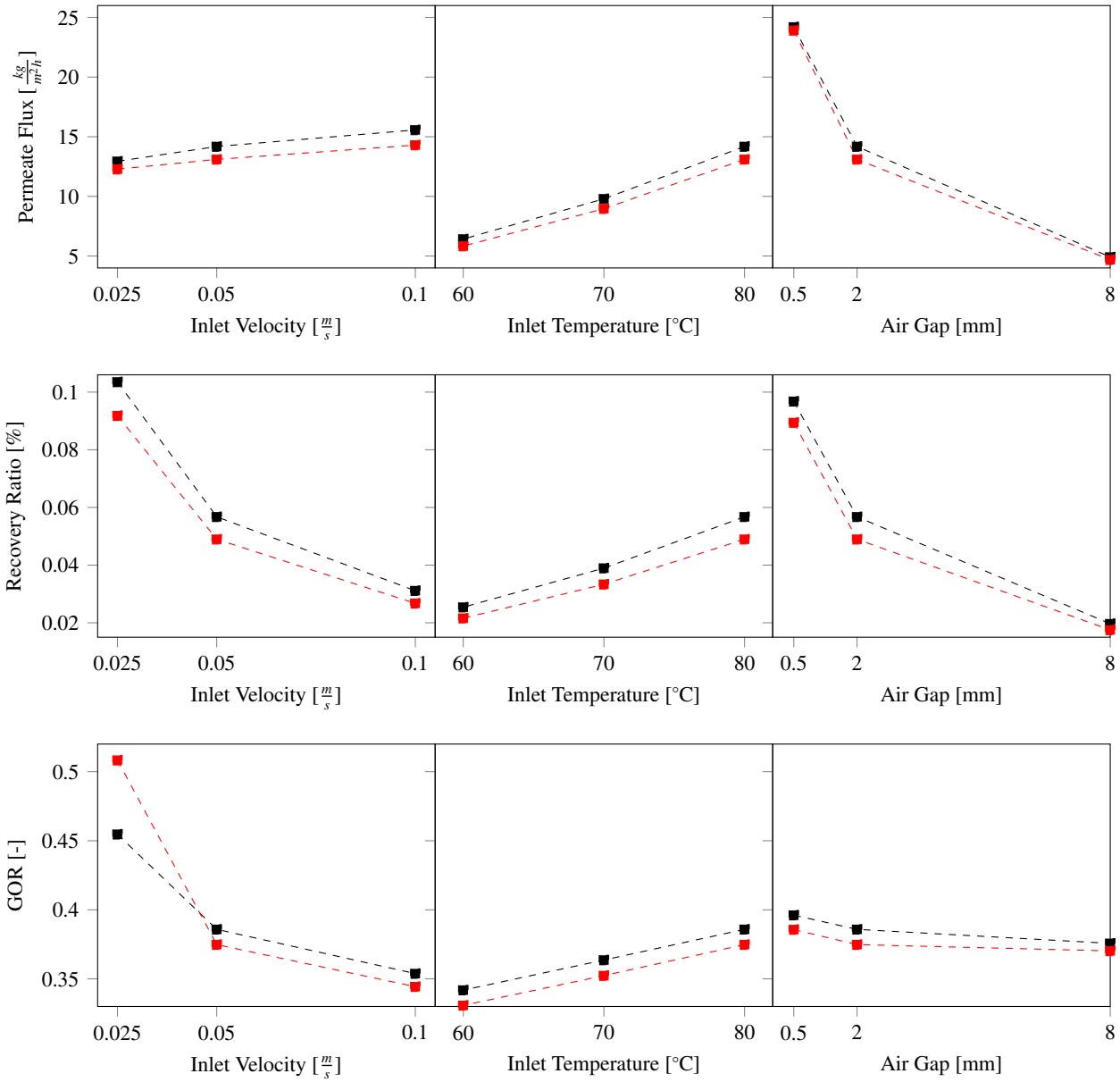

Figure 14: Fresh water output, recovery ratio and GOR for downside configuration: —□— Tap water; —□— Sea water (3.5 wt% salt); default parameter for computation: T_{in} = 80 °C, u_{in} = 0.05 $\frac{m}{s}$ and 2 mm air-gap

The salt concentration has two major influences on the MD process: Firstly, it decreases the saturation vapor pressure at a given temperature and secondly it alters and increases the density profile in the feed channel.

Fig. 15 shows the change in vapor pressure at the evaporation interface in the upward configuration. Sea water is consistently reducing the vapor pressure and therefore the driving force of the MD process for both configurations. The salinity of sea water is, however, lower than of e.g. brine from reverse osmosis for which this effect becomes more profound when treated with MD.

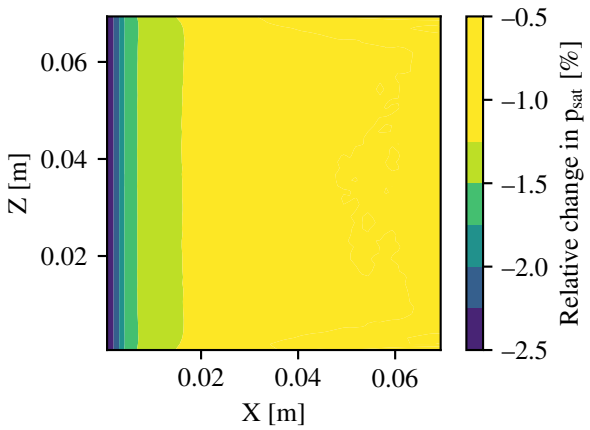

Figure 15: Relative change of vapor pressure between tap water and sea water at the interface between feed and membrane in upside configuration, $T_{in} = 80\,°C$, $u_{in} = 0.05\frac{m}{s}$, 2 mm air-gap

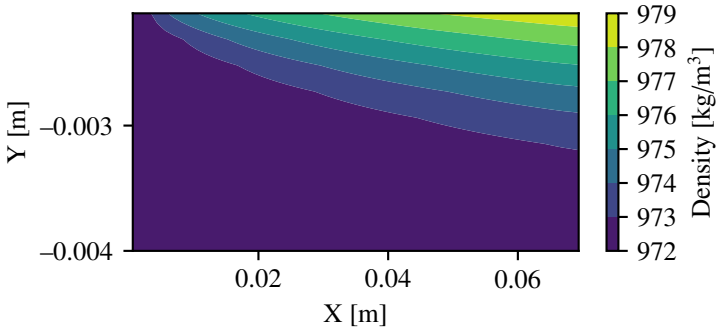

Figure 16: Density profile in boundary layer of the feed water channel (tap water) in mid-Z-plane, $T_{in} = 80\,°C$, $u_{in} = 0.05\frac{m}{s}$, 2 mm air-gap

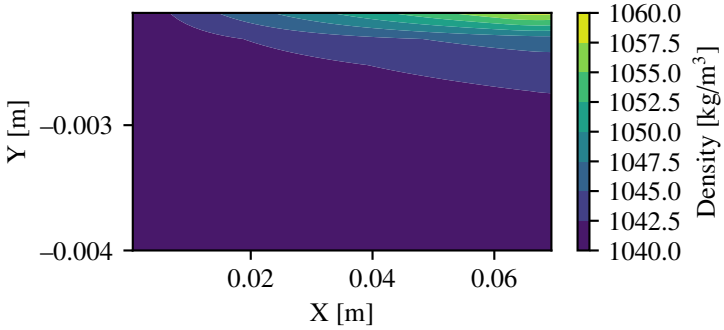

Figure 17: Density profile in boundary layer of the feed water channel (sea water) in mid-Z-plane, $T_{in} = 80\,°C$, $u_{in} = 0.05\frac{m}{s}$, 2 mm air-gap

The density profile in the feed channel is displayed in Fig. 16 for tap water and in Fig. 17 for sea water. Comparing both figures, the density is generally increased in the case of sea water but the boundary layer is narrower. When

using tap water, the density is solely a function of temperature and the profiles of temperature and density resemble one another as can be seen in Fig. 16 and Fig. 18. In the case of sea water, the density becomes also a function of salt content. The salt content profile is shown in Fig. 19 where a very narrow boundary layer is visible.

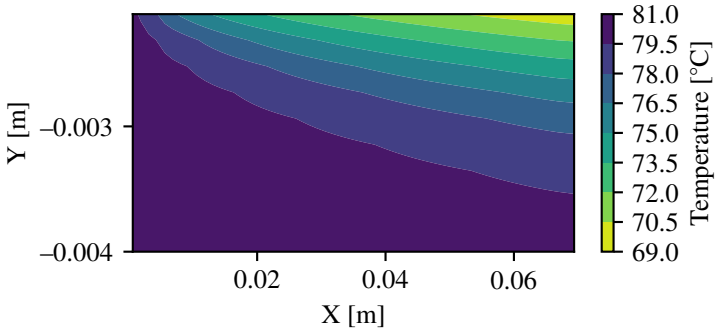

Figure 18: Temperature profile in boundary layer of feed water channel (sea water) in mid-Z-plane, $T_{in} = 80\,°\text{C}$, $u_{in} = 0.05\frac{m}{s}$, 2 mm air-gap

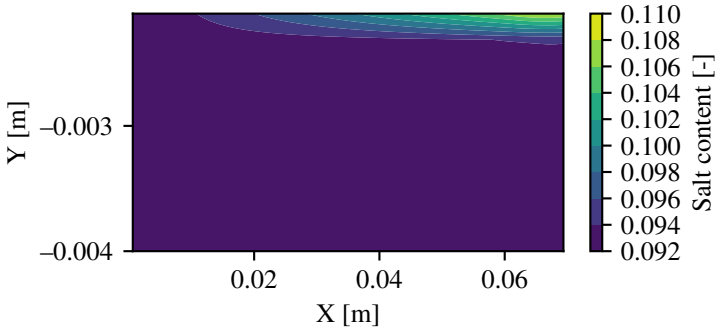

Figure 19: Salt content profile in boundary layer of feed water channel (sea water) in mid-Z-plane, $T_{in} = 80\,°\text{C}$, $u_{in} = 0.05\frac{m}{s}$, 2 mm air-gap

In general, narrower boundary layers favor the MD process and in particular the upside configuration because of the stable stratification in the module. In the downside configuration, the density difference causes buoyancy effects in the feed channel which benefit the heat and mass transfer. The downside configuration is therefore additionally penalized by the decreased density boundary layer in the presence of salt. It remains to be investigated how the boundary layers develop when treating highly saline brines.

4. Conclusion

In this work, two AGMD module configurations are numerically compared and their performance at different feed inlet temperatures, velocities and air-gap thicknesses evaluated. In the upside configuration the hot feed flows above the membrane, while in the downside configuration it flows below the air-gap and membrane. In the latter, the feed solution is not in contact with the membrane but separated by the air-gap which is expected to improve the fouling resistance of the membrane.

For the downside configuration, the velocity profile in the air-gap due to buoyancy is visualized. As feed, both tap water and sea water are studied and compared. In order to do so, the model is extended to compute salt concentration boundary layers which form due to evaporation of vapor and an increase in salt concentration.

The upside configuration produces a slightly higher permeate flux when combining a high feed inlet temperature (80 °C), feed inlet velocity ($0.1\frac{m}{s}$) and narrow air-gap (0.5 mm). At all other operational conditions, the permeate flux is comparable.

The downside configuration is less susceptible to feed inlet velocity than the upside configuration which shows in a slightly higher RR and evidently higher GOR at the lowest feed velocity studied. The vortex formation in the air-gap is favored by low feed velocities which results for smaller air-gaps in an increased energy utilization.

In general, the GOR is consistently and significantly higher for the downside configuration indicating that less energy is needed to distill the same permeate flux compared to the upside configuration. As the main advantage of AGMD is the reduction of heat losses, the downside configuration could bring further improvement in this direction.

Experiments are ongoing at the University of Luxembourg and the experimental validation of these findings is expected to be published soon.

For low salinities like sea water, the salt boundary layer is thinner than the temperature boundary layer and its impact is visible but not yet predominant. The modification implemented in this study orients the model in the direction of studying the treatment of highly saline brines. Evaporation and scaling phenomena can be studied with ultra-high resolution fluid dynamic simulations [23, 24]. For this purpose, 3D structures have been obtained from membranes for MD by X-ray ptychography [25]. Insights from these studies shall benefit the development of the model towards prototyping MD modules for the treatment of highly saline brines for long-term operation.

Acknowledgment

The authors wish to acknowledge ULHPC, Luxembourg for the computational resources.

References

[1] A. Alkhudhiri, N. Darwish, N. Hilal, Membrane distillation: A comprehensive review, Desalination 287 (2012) 2 – 18. Special Issue in honour of Professor Takeshi Matsuura on his 75th Birthday.
[2] A. Alklaibi, N. Lior, Membrane-distillation desalination: Status and potential, Desalination 171 (2005) 111 – 131.
[3] R. B. Saffarini, E. K. Summers, H. A. Arafat, J. H. Lienhard V, Technical evaluation of stand-alone solar powered membrane distillation systems, Desalination 286 (2012) 332 – 341.
[4] M. Khayet, Membranes and theoretical modeling of membrane distillation: A review, Advances in Colloid and Interface Science 164 (2011) 56 – 88. Membrane Separation and Colloid Science.
[5] F. A. Banat, J. Simandl, Desalination by Membrane Distillation: A Parametric Study, Separation Science and Technology 33 (1998) 201–226.
[6] U. Dehesa-Carrasco, C. Pérez-Rábago, C. Arancibia-Bulnes, Experimental evaluation and modeling of internal temperatures in an air gap membrane distillation unit, Desalination 326 (2013) 47–54.
[7] G. L. Liu, C. Zhu, C. S. Cheung, C. W. Leung, Theoretical and experimental studies on air gap membrane distillation, Heat and Mass Transfer 34 (1998) 329–335.
[8] I. Hitsov, K. De Sitter, C. Dotremont, P. Cauwenberg, I. Nopens, Full-scale validated Air Gap Membrane Distillation (AGMD) model without calibration parameters, Journal of Membrane Science 533 (2017) 309–320.
[9] J. Xu, Y. B. Singh, G. L. Amy, N. Ghaffour, Effect of operating parameters and membrane characteristics on air gap membrane distillation performance for the treatment of highly saline water, Journal of Membrane Science 512 (2016) 73–82.
[10] S. Adnan, M. Hoang, H. Wang, Z. Xie, Commercial PTFE membranes for membrane distillation application: Effect of microstructure and support material, Desalination 284 (2012) 297–308.
[11] H. Chang, C.-L. Chang, C.-D. Ho, C.-C. Li, P.-H. Wang, Experimental and simulation study of an air gap membrane distillation module with solar absorption function for desalination, Desalination and Water Treatment 25 (2011) 251–258.
[12] T.-C. Chen, C.-D. Ho, Immediate assisted solar direct contact membrane distillation in saline water desalination, Journal of Membrane Science 358 (2010) 122–130.
[13] E. Guillén-Burrieza, G. Zaragoza, S. Miralles-Cuevas, J. Blanco, Experimental evaluation of two pilot-scale membrane distillation modules used for solar desalination, Journal of Membrane Science 409-410 (2012) 264–275.
[14] D. M. Warsinger, J. Swaminathan, L. L. Morales, J. H. Lienhard V, Comprehensive condensation flow regimes in air gap membrane distillation: Visualization and energy efficiency, Journal of Membrane Science 555 (2018) 517–528.
[15] Y. Z. Tan, L. Han, W. H. Chow, A. G. Fane, J. W. Chew, Influence of module orientation and geometry in the membrane distillation of oily seawater, Desalination 423 (2017) 111–123.
[16] A. Alklaibi, N. Lior, Transport analysis of air-gap membrane distillation, Journal of Membrane Science 255 (2005) 239 – 253.
[17] I. Hitsov, T. Maere, K. De Sitter, C. Dotremont, I. Nopens, Modelling approaches in membrane distillation: A critical review, Separation and Purification Technology 142 (2015) 48–64.
[18] M. M. A. Shirazi, A. Kargari, A. F. Ismail, T. Matsuura, Computational Fluid Dynamic (CFD) opportunities applied to the membrane distillation process: State-of-the-art and perspectives, Desalination 377 (2016) 73–90.
[19] R. Chouikh, S. Bouguecha, M. Dhahbi, Modelling of a modified air gap distillation membrane for the desalination of seawater, Desalination 181 (2005) 257 – 265.

[20] K. Cramer, B. Niceno, H.-M. Prasser, S. Leyer, A three-dimensional model for the heat and mass transfer in air-gap membrane distillation, Manuscript submitted for publication (2018).
[21] D. M. Warsinger, J. Swaminathan, E. Guillen-Burrieza, H. A. Arafat, J. H. Lienhard V, Scaling and fouling in membrane distillation for desalination applications: A review, Desalination 356 (2015) 294–313.
[22] F. J. Millero, F. Huang, The density of seawater as a function of salinity (5 to 70 g kg^{-1}) and temperature (273.15 to 363.15 K), Ocean Science 5 (2009) 91–100.
[23] N. Prasianakis, E. Curti, G. Kosakowski, J. Poonoosamy, S. Churakov, Deciphering pore-level precipitation mechanisms, Scientific reports 7 (2017) 13765.
[24] S. V. Churakov, N. I. Prasianakis, Review of the current status and challenges for a holistic process-based description of mass transport and mineral reactivity in porous media, American Journal of Science 318 (2018) 921–948.
[25] K. Cramer, N. I. Prasianakis, B. Niceno, J. Ihli, M. Holler, S. Leyer, Three-dimensional membrane imaging with x-ray ptychography: determination of membrane transport properties for membrane distillation, Manuscript to be submitted (2019).

Paper D

Speed-up Using GPU Accelerators: How to Port a Numerical Solver for CFD with PyCUDA

Project for the PDC Summer School 2017

Kerstin Cramer & Luca Manzari

February 2018

Contents

1 Introduction

In Computational Fluid Dynamics (CFD) non-linear conservation equations are solved for physical problems which are therefore discretized in space and time to allow local linearization of the equations. For each point of the grid and solving variable, a linear equation is obtained which needs to be solved for every time step. This results in a large system of linear equations growing with the refinement of the grid and the size of the physical problem. These characteristics qualify CFD codes for parallelization: they are commonly executed on Central Processing Units (CPUs) of high performance computers.

Numerous linear equations are solved significantly faster with numerical, iterative methods. Using these methods, the problem is reduced to multiple matrix multiplications with big matrices. This single-instruction-multiple-data paradigm well fits the architecture of Graphical Processing Units (GPUs).

In this report, the process of porting a solver for non-symmetric linear systems of equations to run on GPUs is documented. The chosen solver is the bi-conjugate gradient stabilized (bicgstab) method which ranks as one of the fastest state-of-the-art numerical solvers for linear equations after multigrid methods. It is embedded into a laminar Navier-Stokes CFD code called pyns which is implemented in Python. Therefore, the PyCUDA module is used to translate Python code into NVIDIA CUDA kernels to achieve a speed-up of the overall execution time of the pyns code.

2 pyns.bicgstab

The Finite-Volume code solves the incompressible Navier-Stokes equation in three dimensions. Following the SIMPLE algorithm, the momentum conservation equation is solved to obtain a preliminary velocity field. To ensure the conservation of mass, the pressure gradient is calculated from the pressure correction equation and is used to correct the velocity field.

Both momentum conservation and pressure correction equations are discretized forming a system of linear equations. For each equation, seven system matrices are formed (one central and six for the neighboring directions). For their solution, an analytical solver, Krylov subspace methods and a multigrid solver are implemented. The implementation of the bicgstab method and the two subroutines it uses are discussed in this report.

`bicgstab` takes as input the seven system matrices, the matrix of the respective solving variable and the right-hand-side matrix of the linear equation to solve. Additionally, the desired tolerance and the maximum number of iterations can be set. In accordance with

the bicgstab algorithm, new values for the solving variable are computed for the next time step in an iterative way using scalar operations and subroutines for matrix multiplication.

`vec_vec` calculates the vector-dot product of two matrices by performing an element-wise multiplication followed by a sum reduction.

`mat_vec_bnd` takes as input the seven system matrices and the matrix of the solving variable with its boundary values. The returned matrix represents the product of the left-hand side of the system of linear equations (the coefficient matrix multiplied with the solving variable). It does so by multiplying the central system matrix with the variable matrix and subtracting from it the results from the multiplication of the six neighbouring matrices with the solving variable matrix concatenated with the respective boundary values.

These three functions are ported and run on the GPU.

3 PyCUDA

The PyCUDA module enables the execution of Python code on NVIDIA GPUs. Firstly, the `pycuda.driver` library has to be imported as it contains the CUDA functions. Secondly, the import of `pycuda.autoinit` is useful as it initializes automatically a context for evoking CUDA kernels. It probes for installed devices and decides on the number of blocks-per-grid and threads-per-block. Therefore, these parameters do not need to be modified or specified anymore. The context can also be set manually.

The `pycuda.gpuarray` library offers convenient built-ins for handling numpy-compatible data types. Slicing of gpuarrays on the GPU is thereby supported and mathematical operations for gpuarrays are either built-in routines (like the matrix dot product) or offered in the `pycuda.cumath` library (like the sine function). Broadcasting and comparison operations are not clearly defined in PyCUDA. Multiplying a vector and a scalar both living on the GPU will multiply only the first element of the vector with the scalar. To correctly multiply a scalar and a vector that are on the GPU, the scalar needs to be fetched on the host: the multiplication is then carried out correctly on the GPU. The method `gpuarray.to_gpu()` allocates memory and copies data from a numpy array to the GPU. To copy data into an existing gpuarray instance, the method `gpuarray.set()` can be used. Fetching data is performed calling the `gpuarray.get()` method.

Other options that PyCUDA offers require some C code to be written. `ElementwiseKernel` from `pycuda.elementwise` takes an array as input, and runs the kernel on each element of the array. `ReductionKernel` from `pycuda.reduction` lets the user specify an elementwise operation (as in `ElementwiseKernel`) and a reduction operation to be executed afterwards. `SourceModule` from `pycuda.compiler` is a Python wrapper for native CUDA code.

4 Benchmarks

The computations are run on the ULHPC Cluster Gaia on Intel Xeon E5-2680v3 CPUs and NVIDIA Tesla K80 GPUs when referred to Gaia. When referred to Tegner, the computations are carried out on KTH PDC Cluster Tegner on Intel E5-2690v3 Haswell CPUs and NVIDIA Tesla K80 GPUs. The code for the benchmarks can be found on github[1].

4.1 Matrix Multiplication on CPU vs. `gpuarray`

In this benchmark study, the elapsed time is compared when executing on the CPU versus on the GPU using `pycuda.gpuarray`. The matrix multiplication of two random, three dimensional matrices was performed 32, 64 and 128 times. The order of the matrices was varied between 64 and 256 in 16-increments. Two different cases for copying the matrices to the GPU are thereby tested: whereas using `gpuarray.to_gpu()`, memory for both matrices is allocated in each iteration anew followed by the copying of the values, using `gpuarray.set()`, it is only needed to copy the matrices' values each iteration into memory space which was preallocated in advance.

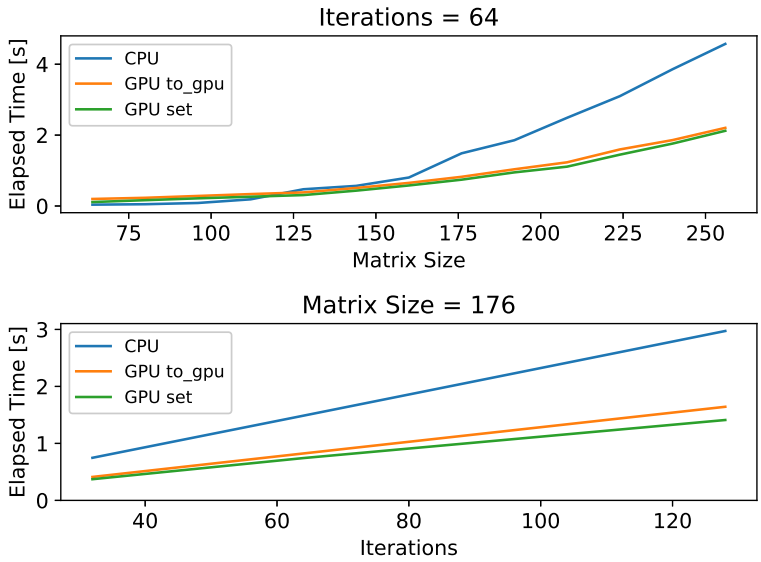

Figure 1: Comparison of the run time of CPU and `gpuarray` methods: Elapsed time for matrix multiplication of three-dimensional matrices of order *Matrix Size* after 64 iterations and influence of number of iterations on the elapsed time

[1] `https://github.com/kjcramer/pyns/tree/HPC_SummerSchool/pycuda/benchmarks`

The results shown in Figure 1 are run on Tegner. The break-even-point between CPU and GPU execution time lies between the matrix order of 112 and 128. Also, `gpuarray.set()` is consistently faster than `gpuarray.to_gpu()`, if an array needs to be written more than once, since the cost of the initialization and allocation is spared. The allocation time is independent of the amount of data that needs to be written.

4.2 Sine Function on CPU vs. `gpuarray` vs. C Kernel vs. `Elementwise` Kernel

This benchmark is taken from the PyCUDA example gallery[2] and modified to include memory copying to the GPU in the time counting. It compares the execution time of the CPU and four methods to run on the GPU. The sine is computed of a one-dimensional vector with lengths between 16 to 256 with 16-increments for 100, 1000 and 10000 times. Using the `gpuarray` method, in every iteration the vector is send to the GPU where the sine is calculated using the `cumath` library (looping on the CPU). Two `Elementwise` kernels are compared: one of them loops on the GPU (*EW w. loop*) whereas the other kernel is called in a loop on the CPU (*EW*). Moreover, a C kernel is executed.

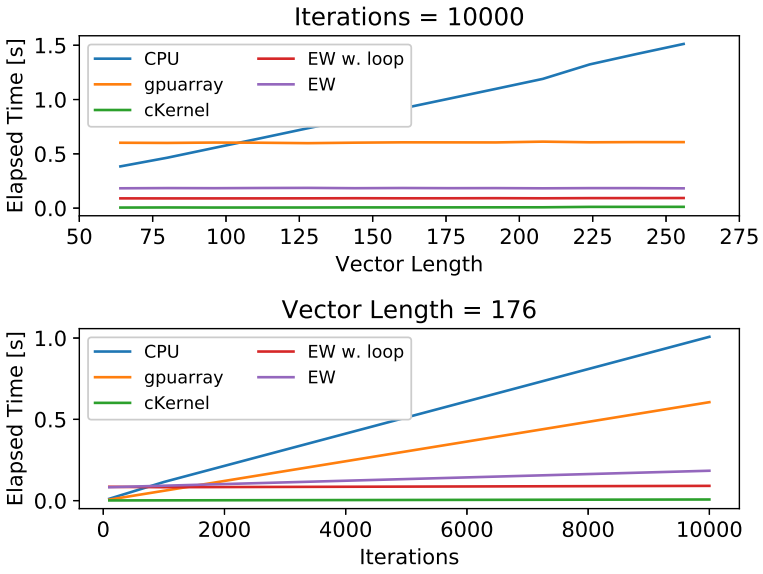

Figure 2: Comparison of the run time of CPU, `gpuarray` method, `Elementwise` kernel (with internal & external loop) and C kernel: Elapsed time of sine computation after 10.000 iterations and influence of number of iterations on the elapsed time

[2] `https://wiki.tiker.net/PyCuda/Examples/SimpleSpeedTest`

The graphs shown in Figure 2 are obtained on Gaia. The C kernel is for all vector lengths and number of iterations the fastest. For a small number of iterations (less than around 1500) the `gpuarray` method performs better than the `Elementwise` kernels.

Looping on the GPU speeds up the computation. However, it is only feasible if each iteration operates on the same data, like computing 100 times the sine of the same matrix. If data changes and need to be updated, a copying operation prevents the usage of an internal loop on the GPU as used in the `Elementwise` kernel with internal loop and the C kernel.

4.3 Matrix Multiplication on CPU vs. `gpuarray` vs. `Reduction` Kernel

In this benchmark, single matrix multiplication of random, three dimensional matrices of order 64 to 512 in 16-increments is compared running on the CPU and on the GPU using `gpuarray` and a `Reduction` kernel. A comparison that included also a C kernel was attempted but returned incorrect values and was therefore discontinued.

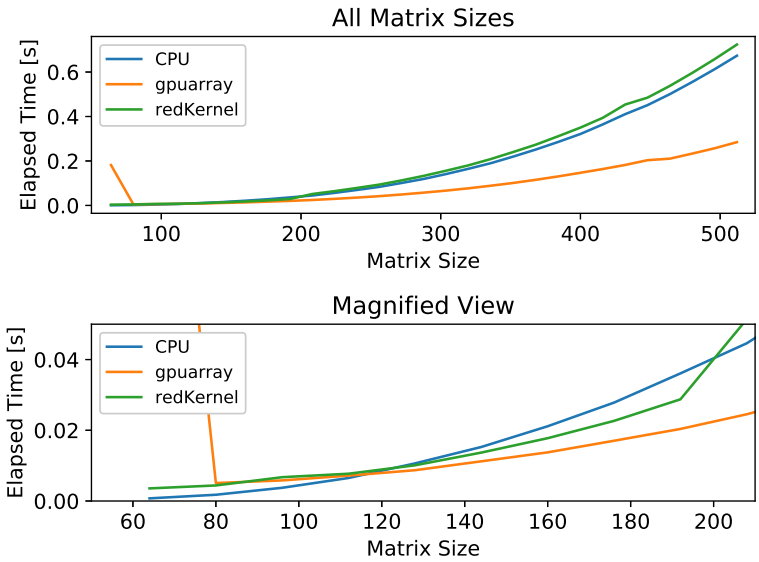

Figure 3: Comparison of the run time of CPU, `gpuarray` method and `Reduction` kernel: Elapsed timeforf matrix multiplication of three-dimensional matrices of order *Matrix Size*

The results shown in Figure 3 are computed on Gaia. When called for the first time, the `gpuarray.dot()` method compiles a kernel, hence it takes longer time to execute in the first computation. For matrix orders bigger than 200, the `gpuarray.dot()` method performs the fastest. The `Reduction` kernel runs faster than the CPU for matrix orders between 120 and

200. This behavior can be observed on Tegner NVIDIA Tesla K420 as well, so is not only exclusive to Gaia nor to the NVIDIA Tesla K80.

Finally, the `gpuarray` class offers the highest flexibility as much as decent speed-up when working with different matrix operations.

5 Final Implementation

The numpy arrays and scalars passed to the `bicgstab` function are converted to `gpuarray` and pushed to the GPU. A gpu version of the class `Unknown` is thereby used. The mathematical operations are carried out and saved on the GPU. The final array is fetched from the GPU and returned from the `bigcstab` function. Comparison operations in `bicgstab` are carried out on CPU since no comparison operator is defined in PyCUDA: they might be carried out on the GPU using `gpuarray.is_positive()`, but this has not been tested yet.

The `mat_vec_bnd` subroutine operates on the GPU in the same way as on the CPU. The slicing is done on the GPU. In `vec_vec`, the PyCUDA built-in `gpuarray.dot()` routine is used.

A boolean *gpu* is set in the `bicgstab` function to enable the computation on the GPU. It is additionally passed as an input parameter to the subroutines which is per default false.

As test case, the flow around four rectangular-shaped obstacles arranged in a labyrinth setting is computed for 200 time steps. The `bicgstab` function is called four times per times step: three times for solving each velocity component and a fourth time for the pressure.

The maximal Courant-Friedrich-Lewy (CFL) number is compared to examine the accuracy of the computation on the GPU. It is important to note that 64 byte precision is needed to achieve sufficient results. The mid-plane velocity and pressure fields after 200 time steps are compared to ensure that differences lie in the order of numerical diffusion. Plots are shown in Appendix B.

The test case is run with different mesh sizes, displayed in Table 1. The aspect ratio is specified in the table as the obstacles are scaled with the grid dimension. Equal aspect ratio ensures an equal physical problem.

Just like the benchmarks, the computations are run on the ULHPC Cluster Gaia on Intel Xeon E5-2680v3 CPUs and NVIDIA Tesla K80 GPUs when referred to Gaia. When referred to Tegner, the computations are carried out on KTH PDC Cluster Tegner on Intel E5-2690v3 Haswell CPUs and NVIDIA Tesla K80 GPUs. The code and simulation data can

Mesh	Size	Aspect Ratio
1	$64 \cdot 16 \cdot 16$	4:1
2	$128 \cdot 16 \cdot 16$	8:1
3	$128 \cdot 32 \cdot 32$	4:1
4	$256 \cdot 32 \cdot 32$	8:1
5	$256 \cdot 64 \cdot 64$	4:1
6	$512 \cdot 64 \cdot 64$	8:1
7	$512 \cdot 128 \cdot 128$	4:1

Table 1: Mesh sizes used for computation and aspect ratio between main flow axis and the two orthogonal axes

be found on github[3]. The final simulation results are grouped in the corresponding folder (e.g. "gaia_gpu/").

The computation times are averaged between 24 runs per mesh size on CPU Tegner and three runs per mesh size on CPU Gaia and the GPUs (both Tegner and Gaia). On CPU Tegner, one run per physical core of the node is performed simultaneously, whereas on CPU Gaia one simulation on one core per node is run.

In Figure 4 the total execution time of the full simulation is shown. Computation on the GPU is faster for mesh sizes larger than mesh 4 or 5. As the aspect ratio of the mesh is changing, the number of iterations in `bicgstab` might change and by that also the overall execution time.

In Figure 5 the average time per inner iteration in `bicgstab` for all calls of `bicgstab` is shown. Even though the slopes are slightly different, the critical mesh size stays the same. For larger mesh sizes, the time advantage of computing on the GPU increases significantly. On Gaia, while mesh 5 takes the same time to run on CPU and GPU, the GPU is already twice as fast for mesh 6. The speed-up of mesh 7 even increases to 5.6 meaning that a simulation takes a day instead of a working week.

On Tegner, when running a simulation on each core of the CPU node, already mesh 3 is 1.5 times faster on the GPU. For mesh 4 the speed-up is 4.4, for mesh 5 it is 6.9, for mesh 6 it is 6.6. Mesh 7 is nearly 12 times faster on the GPU.

[3] `https://github.com/kjcramer/pyns/tree/HPC_SummerSchool/pycuda`

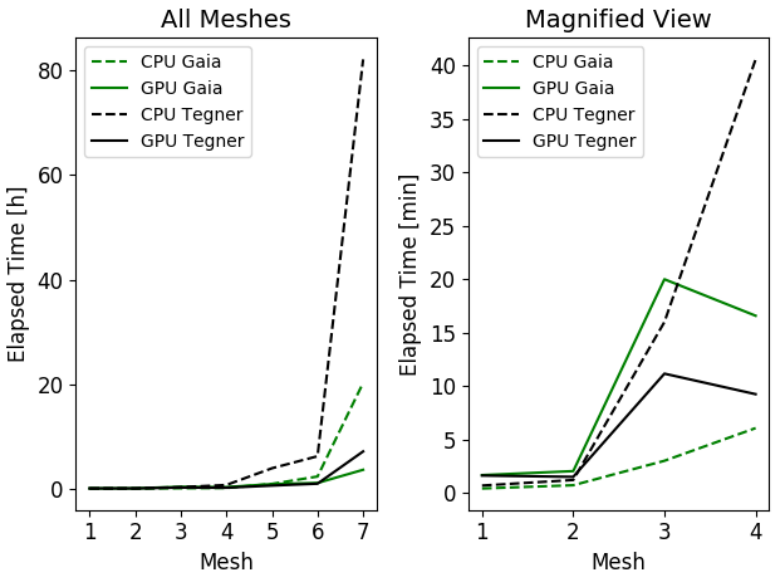

Figure 4: Comparison of the total execution time of 200 time steps for different mesh sizes computed on CPU and GPU

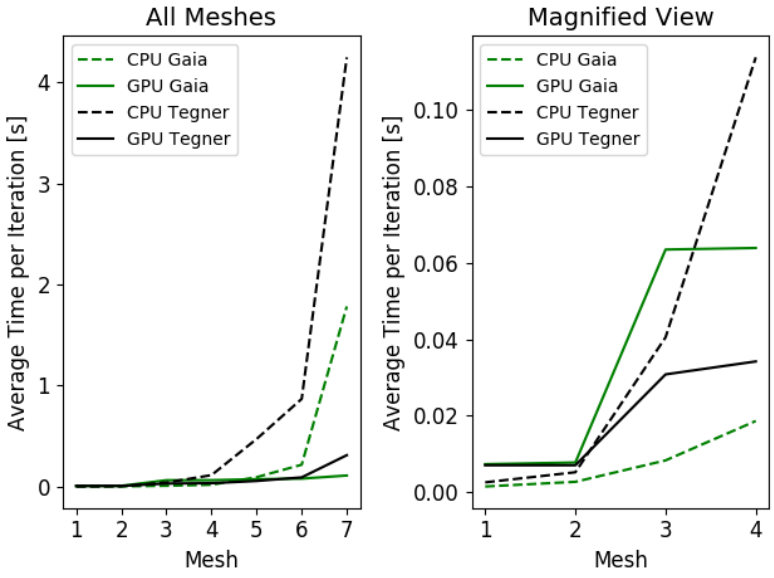

Figure 5: Comparison of the average time spent per iteration in `bicgstab` for different mesh sizes computed on CPU and GPU for 200 time steps

6 Conclusion

Looking at the results, the port of the numerical solver `bicgstab` can be considered successful: a simulation that would take a working week can now be performed in less than a working day.

PyCUDA is relatively easy to use, once its limits are understood and circumvented (e.g. multiplying a scalar with a matrix): with the `pycuda.gpuarray` library you don't need to be a programmer – even mechanical engineers get somewhere without worrying about pointers. The documentation, scary at first, might be more understandable to trained computer scientists.

When working with CFD and numerical methods, 64 byte precision on the GPU is an absolute requirement. This might be a constraint for GPUs that lack hardware support for double precision numbers. Moreover, in case of a machine that has multiple users and only one GPU, there is no easy way to tell whether a process is already using the GPU or not. In an environment like a supercomputer, having to reserve a 24-cores node and using only its GPU is a potential waste of resources.

Acknowledgement

We want to thank the people behind both PDC and ULHPC for being super-supportive and quick in replying to every question we encountered as engineers who dared to approach the field of computer science.

Appendices

A Setting up HPCs

Running on PDC KTH Tegner

1. `kinit --forwardable -l 7d manzari@NADA.KTH.SE`
2. `ssh USER@tegner.pdc.kth.se`
3. `salloc -t hh:mm:ss -N 1 -A summer-extra-2017 --gres=gpu:K420:1 [or K80:2]`
4. ssh directly to GPU node
5. `module load cuda anaconda`

Running on ULHPC Gaia

1. `ssh gaia`
2. `oarsub -t gpu -l nodes=1/core=2,walltime=hh:mm:ss ./myscript.sh`
   - for specific node `-p "network_address='gaia-182'"`
   - for specific GPU `-p "gputype='K80'"`
   - for batch job do header `#!/bin/bash -l`

B CFD Simulation Figures

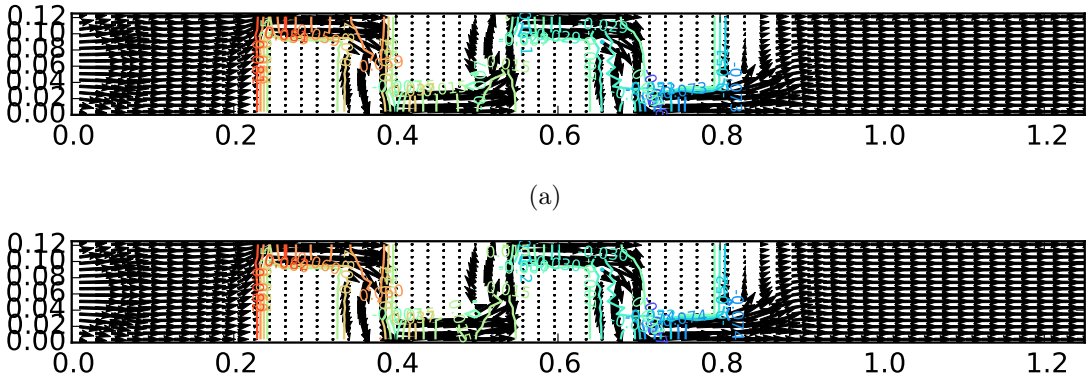

(a)

(b)

Figure 6: Velocity (arrows) and pressure field of mesh 1 in the mid-z-plane after 200 time steps (a) run on CPU (b) run on GPU